Aerodynamics of a Rotating and Flapping Insect Wing

by

Shantanu S. Bhat

A thesis submitted for the degree of Doctor of Philosophy
at Monash University in 2018

Department of Mechanical and Aerospace Engineering

Copyright notice

According to the classical theory of aerodynamics, it is impossible for a bumblebee to fly, but the bumblebee doesn't know anything about the laws of aerodynamics, so it goes ahead and flies anyway.

Author unknown

I have no doubt that in reality the future will be vastly more surprising than anything I can imagine. Now my own suspicion is that the Universe is not only queerer than we suppose, but queerer than we can suppose.

J. B. S. Haldane (1927)

Abstract

Further advances in the design of micro air vehicles (MAVs) may require detailed understanding of the aerodynamics of the flapping wings of insects, which outperform the lifting mechanisms used in standard MAVs. Researchers in the past have proposed different mechanisms in order to explain the higher lift observed for insect wings flapping at very high angles of attack. Studies investigating the effects of various geometrical and kinematic parameters on the flow structure and forces over a wing have greatly improved our understanding of the flapping wing aerodynamics. However, studies on some of the key parameters, such as the wing aspect ratio and Rossby number, have resulted in seemingly contradictory results. Moreover, the effects of wing shape and wing kinematics are also not well understood. This thesis presents results of four studies related to the aerodynamics of a rotating and flapping insect wing. This comprehensive work involves both experimental and numerical methods.

The first study investigates the effects of the central body size on the rotating wing aerodynamics. It is revealed that beyond a certain central body size, the flow structure over a wing changes dramatically. The presence of a central body is also observed to have a detrimental effect on the forces over the wing, beyond a certain size (i.e. the radius normalised by the wing span, $\hat{b}_0 > 0.5$). The second study investigates the coupled effects of the wing aspect ratio, Reynolds number and Rossby number. Interestingly, a span-based scaling proposed for the Reynolds number and Rossby number helps reconcile the past studies. The third study presents an evolutionary shape optimisation approach to optimise the wing shape. Although, this approach has been used in the past for load bearing structures, its use in the design of wing shapes is novel, to the knowledge of the author. The optimised wings have more area outboard, as compared to the generic shapes used in past studies. This study provides some possible reasons behind the wing shapes observed in some insects and Samara seeds. The fourth study investigates the effects of a range of flapping motion waveforms on the wing aerodynamics. The results show that the rapid flip motion towards the end of a half-stroke is advantageous for achieving a high lift and high power economy. However, the sweep motion profile has different effects on the lift and power economy. Interestingly, most insects have a near-sinusoidal sweep motion profile, which is shown to result in a high lift.

Overall, the various aspects of the insect wing aerodynamics investigated in the four

studies can provide useful insights into some unanswered questions regarding insect flight. The results also highlight some optimised parameters, such as the wing aspect-ratio, wing shape, and the flapping profile parameters, that may be useful in the design of MAVs for better performance.

Declaration

This thesis contains no material which has been accepted for the award of any other degree or diploma at any university or equivalent institution and that, to the best of my knowledge and belief, this thesis contains no material previously published or written by another person, except where due reference is made in the text of the thesis.

Signature: [redacted]

Name: Shantanu Bhat

Date: May 28, 2018

Publications Relating to Thesis

BHAT, S. S., ZHAO, J., SHERIDAN, J., THOMPSON, M. C. & HOURIGAN, K. 2015 Investigation of the flow structure over a rotating insect wing using PIV measurements. *In proceedings of the 7th Australian Conference on Laser Diagnostics in Fluid Mechanics and Combustion*, Melbourne, Australia, December 2015.

BHAT, S. S., ZHAO, J., JACONO, D. L., SHERIDAN, J., HOURIGAN, K. & THOMPSON, M. C. 2016 Effect of central body size on the leading-edge vortex of a rotating insect wing. *In proceedings of the 20th Australasian Fluid Mechanics Conference*, Perth, Australia, December 2016.

BHAT, S. S., ZHAO, J., SHERIDAN, J., HOURIGAN, K. & THOMPSON, M. C. 2018 The leading-edge vortex on a rotating wing changes markedly beyond a certain central body size. *Royal Society Open Science* **5** (7), 172197.

BHAT, S. S., ZHAO, J., SHERIDAN, J., HOURIGAN, K. & THOMPSON, M. C. 2018 Uncoupling the effects of aspect ratio, Reynolds number and Rossby number on a rotating insect-wing planform. *Under consideration for publication in the Journal of Fluid Mechanics.*

BHAT, S. S., ZHAO, J., SHERIDAN, J., HOURIGAN, K. & THOMPSON, M. C. 2018 Evolutionary shape optimisation of a rotating wing. *Under consideration for publication in the Journal of Fluid Mechanics.*

Acknowledgements

First and foremost, I would like to express my gratitude to my supervisors, Prof. Mark C. Thompson, Prof. Kerry Hourigan and Prof. John Sheridan, for their guidance, encouragement and support. Working with them was an excellent learning experience. I would also like to thank Dr. Jisheng Zhao for his supervision, willingness to share his expertise and also for his timely advice.

I would like to extend my thanks to Dr. David Lo Jacono, Dr. James Venning, Dr. Tim Crouch, and Daniel Tudball Smith for their ideas and suggestions that helped me in this work. I take this opportunity to thank Hugh Venables, Mark Symonds, Bruce Dudley, Santhosh Babu, Narendra Babu, and Chris Pierson, from the mechanical and electronics workshops, for their help in the fabrication of my experimental setup. I owe a special thanks to Nat De Ros for his ideas and skills in machining crucial parts in the setup assembly. I also thank Jane Moodie for her timely inputs on my technical writing and presentation skills.

It has been a pleasure to work with Anchal Sareen, Lawrence Wong, Atul Soti, Thomas McQueen, and Takao Oku in the *FLAIR* water channel lab. I also want to thank Methma Rajamuni, Dhiraj K. Singh, Rajiv Kumar, and Sarang Kulkarni. Our group-lunch sessions used to be the most refreshing part of the day. Special thanks to Jagmohan Singh for his help throughout my PhD. I would like to thank Siavash Maleki and Shibo Wang for their help in my computational setup.

I am indebted to Sheetal and Saee Ranade for providing me and my wife all the moral support that we needed in our initial days in Melbourne. Further, it is a pleasure to mention Bhagyashri Patil, Rahul Patil, Ankit Jain, Ankita Jain, Anuradha Kulkarni, and Naren Kulkarni. My sincere thanks to Sameehan Joshi for his encouragement and help.

I would like to acknowledge the resources provided by the Department of Mechanical and Aerospace Engineering. I also acknowledge the financial support of Monash Gradual Scholarship (MGS) and Monash International Postgraduate Scholarship (MIPRS).

Finally, my warm thanks to my parents, Mrs. Sandhya Bhat and Mr. Shrinath Bhat, for their unconditional love, encouragement and understanding. My sincere thanks to my brother, Akshay, and sister in law, Apurva, for being supportive, when I was away from home. I also thank Rahul Dada, Purnima Vahini, my mother in law, late Mrs. Jayashree Kulkarni, and father in law, Mr. Suresh Kulkarni, for their support. I wholeheartedly thank my lovely wife, Meghana, for her inseparable support and for helping me get through tough situations. To her, I dedicate this thesis.

Contents

Nomenclature

Mathematical symbols

$\frac{\mathrm{d}}{\mathrm{d}t}$ Time derivative

$\int$ Integral

∇ Vector gradient operator

Greek symbols

α Angle of attack (°)

μ Dynamic viscosity (Ns/m^2)

ν Kinematic viscosity (m^2/s)

Ω Angular velocity (rad/s)

Ω_c Constant angular velocity (rad/s)

$\dot{\Omega}$ Angular acceleration (rad/s^2)

ω_z Spanwise vorticity (s^{-1})

ϕ Sweep angle or stroke angle (°)

ψ Pitch angle (°)

ρ Density (kg/m^3)

τ Torque (Nm)

θ Deflection angle (°)

English symbols

$\overline{r}_1$ Radius of the first moment of inertia (m)

$\overline{r}_2$ Radius of the second moment of inertia (m)

b Wing span (m)

b_0	Wing root offset (m)
c	Wing chord (m)
c_m	Mean wing chord (m)
F	Force (N)
f	Wing beat frequency (Hz)
p	Pressure (N/m^2)
Q	Second invariant of velocity gradient tensor (s^{-2})
R	Wing tip radius or total span (m)
r	Radial location along the wing span (m)
R_g	Radius of gyration of a wing (m)
S	Wing area (m^2)
T	Time period of flapping or time for one rotation (s)
t	Time (s)
u	Velocity (m/s)
U_g	Wing velocity at the radius of gyration (m/s)
U_t	Wing tip velocity (m/s)
u_z	Spanwise velocity (m/s)
u_{abs}	Velocity in absolute frame of reference (m/s)
CFD	Computational fluid dynamics
ESO	Evolutionary structural optimisation
HSV	Horseshoe-shaped vortex
LEV	Leading-edge vortex
MAV	Micro air vehicle
PIV	Particle image velocimetry
TEV	Trailing-edge vortex
TV	Tip vortex

Non-dimensional variables

$\mathcal{R}$ Wing aspect ratio

$\overline{C}_D$ Mean coefficient of drag

$\overline{C}_L$ Mean coefficient of lift

$\overline{C}_P$ Mean coefficient of power

$\hat{b}_0$ Wing root offset normalised by wing span

γ_1 Vortex centre identification scalar field

γ_2 Vortex core identification scalar field

Γ_z^* Normalised spanwise circulation around a LEV

ω_z^* Normalised spanwise vorticity

p_p^* Normalised pressure on wing pressure side

p_s^* Normalised pressure on wing suction side

C_D Coefficient of drag

C_L Coefficient of lift

C_P Coefficient of power

C_ψ Pitch motion profile parameter

ER Evolutionary rate in ESO method

K Sweep motion profile parameter

P Wing petiolation or wing root offset normalised by chord

PE Power economy

Q^* Normalised second invariant of velocity gradient tensor

Re Reynolds number

Re_b Reynolds number with wing span as the length scale

Re_{span} Reynolds number based on wing tip velocity and wing span

Ro Rossby number

Ro_b Span-based Rossby number

RR Rejection ratio in ESO method

Miscellaneous symbols

§ Thesis section

List of Figures

List of Tables

Chapter 1

Introduction

Flying is a way of life for the majority of animals. From around 1 million species of animals, 75% are winged insects, birds, and bats. Flight performance is crucial for these animals as their survival and evolution depends on it. Aerodynamics of flying animals has been a topic of interest to physicists as well as biologists around the world. Motivated by the research in aircrafts, the aerodynamics of large flying animals has been studied in detail over the past many years. But the aerodynamics of small flyers is not understood well. Recent developments in micro air vehicles (MAVs) have created a demand for designs of smaller flying vehicles. Inspired by insects, some flapping wing MAVs have also been developed, such as *DelFly II* by TU Delft University and *Robobee* by Harvard University, which are shown in figure 1.1. However, the natural flyers still outperform the most sophisticated MAV designs. Hence, the study of insect wing aerodynamics can provide useful insights into designing efficient and accurately controlled MAVs that can find a wide range of applications, such as in fire-fighting, hazard exploration, and rescue operations.

Flight of small birds and insects seems improbable with the standard theory of aerodynamics. The popularly known *bumble-bee paradox* suggested that a bumble-bee should not generate enough lift to fly, according to the conventional theory. With advances in flow visualisation and force measurement techniques, it was revealed that the unsteady phenomena associated with the flapping wings of an insect are responsible for the generation of sufficient lift to support its weight. The insect wings maintain a very high angle of attack during their flapping motion, at which a stationary wing would stall, failing to generate a high lift. However, a flapping wing slices through the air, creating a large swirling vortex past its leading edge, known as the leading-edge vortex (LEV). This provides the extra lift necessary for the insect to fly.

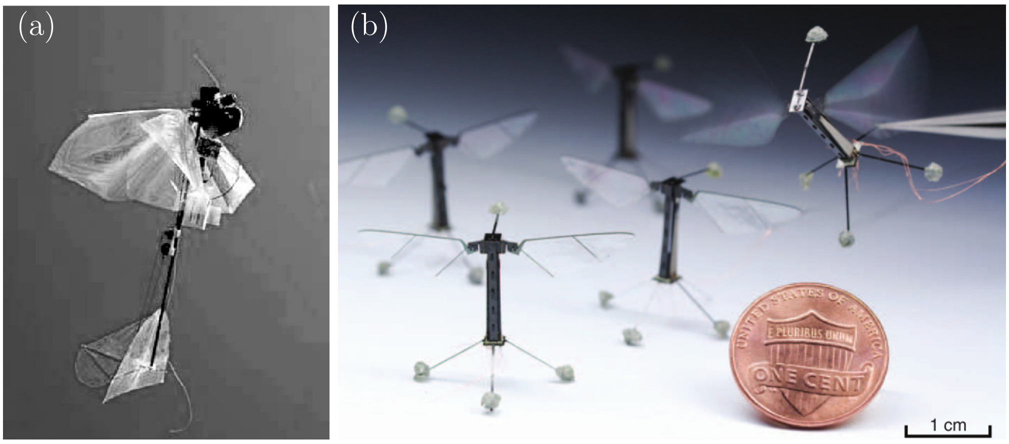

FIGURE 1.1: Insect inspired MAVs, namely, (a) Delfly II, with a single wing span of 14 cm, by De Clercq *et al.* (2009)[1] and (b) Robobee, with a single wing span of 3 cm, by Ma *et al.* (2013)[2].

Researchers have investigated different aspects of flapping motion, both experimentally and numerically. Moreover, the flow over an insect body was also found to interact with the LEV (Liu & Zheng, 2006). However, the influence of body size on the LEV structure has not been explored. Several other geometrical and kinematic parameters are known to influence the insect wing aerodynamics. The effects of wing aspect ratio, Reynolds number, and Rossby number have been studied by a number of researchers. The influence of these parameters, particularly the aspect ratio, on the LEV structure and the aerodynamic loads has been debatable. Recently, it was found from two independent studies that the effects of any two of these parameters are coupled (Harbig *et al.*, 2013; Lee *et al.*, 2016), which may have resulted in the discrepancies in the literature. A systematic variation of each of these three parameters will be useful to explain their combined effects. By decoupling the effects of these parameters, it might be possible for researchers in future to focus on each parameter independently.

Furthermore, there are some studies in the literature that have optimised wing shapes and flapping kinematics for MAVs. Most of such studies focus on optimising the aerodynamic loads predicted using the quasi-steady models. A different approach, such as the evolutionary structural optimisation (ESO) method, can be explored to optimise wing shapes. Use of the quasi-steady models has limited advantages, in that

[1]Republished with permission of SAGE Publications

[2]Republished with permission of American Association for the Advancement of Science from Ma *et al.* (2013); permission conveyed through Copyright Clearance Center, Inc.

the predicted aerodynamic loads cannot be correlated to the flow structures. Therefore, an experimental study of the flapping wing kinematics will be helpful in having a comprehensive understanding of the flow structures and the resulting aerodynamic loads. The outcomes from these studies can help researchers design more efficient MAVs.

This thesis aims at an investigation of the effects of the geometrical and kinematic parameters on the flow over a rotating and flapping wing. The review of past studies on this topic is presented in chapter 2. In the present investigation, a combination of experimental and computational methods has been used. Chapter 3 describes the experimental and computational methods. The thesis outlines four broad studies, namely, the study of the effect of the central body size, the study of the coupled effects of the aspect ratio, Reynolds number, and Rossby number, optimisation of the wing shape, and optimisation of the flapping motion profile. The results from the four studies are presented in chapters 4, 5, 6, and 7, respectively. The research outcomes are summarised and recommendations for future studies are given in chapter 8.

Chapter 2

Insect Wing Aerodynamics

Flapping motion of insect wings has fascinated researchers from around the world for more than past 50 years. Very high flapping frequency and low inertia make it difficult to accurately describe the unsteady forces and the flow field around the flapping wings of insects. Initial research on the insect wings was focused on quantifying the aerodynamic characteristics of insect wings. Researchers such as Jensen (1956) treated insect flight as a sequence of stationary flow situations. Further investigation, for example by Bennett (1966), showed that unsteady effects have significant influence on the insect flight. Study of flapping motion of insect wings is complex in a sense that their small size and very high wing beat frequency pose a challenge in their study. A common fruit fly has a wing size of approximately 2-3 mm where as its flapping frequency is about 200 Hz. Some larger insects have a larger wing area and relatively lower flapping frequency. The wing shape can be characterised broadly by its aspect ratio ($\mathcal{R}$) and the wing kinematics can be characterised by its Reynolds number (Re), which are defined later in § 2.1. Table 2.1 shows a comparison of mass, frequency, Reynolds number, and aspect ratio of flapping wings of three different insects and the hummingbird.

It is challenging to conduct experiments on such free flying insects, such as those by Liu *et al.* (2018), as this would require a setup and measuring instruments that continuously track an insect's position. Hence, most such studies have been performed

Parameters	**Fruit fly**	**Bumblebee**	**Hawkmoth**	**Hummingbird**
Total mass (mg)	2	175	1579	8400
Flapping frequency (Hz)	200	150	25	23
Re	130-210	1200-3000	4200-5300	11000
$\mathcal{R}$	2.91	3.33	2.65	4.5

TABLE 2.1: Comparison of size and frequency of small flyers (Shyy *et al.*, 2008).

on tethered insects (Vogel, 1966; Wootton, 1979; Zanker & Götz, 1990; Bomphrey *et al.*, 2005; Caballero *et al.*, 2015). However, tethering causes a disruption to the insect's sensory feedback that results in a strong distortion of the flapping pattern (Fry *et al.*, 2005). Some attempts have also been made to perform experiments on freely hovering insects (Fry *et al.*, 2008). To keep an insect hovering in place, it is also important to maintain the required lighting conditions and create a virtual reality environment during the experiments. Considering the small size and very high flapping frequency of insect wings, it is also difficult to measure the tiny forces and flow fields around them. Interestingly, some flapping wing MAVs, such as those shown in figure 1.1, have also been developed, ranging in size from a few centimetres to about a few millimetres.

Dynamically scaled mechanical models or numerical models can be used to simulate the flapping motion and then measure or predict the forces and the flow field around the wings. The parameters studied in the case of flapping wing motion can be broadly classified as geometrical and kinematic parameters. The parameters such as wing shape, aspect ratio, camber and flexibility are some of the important geometrical parameters and the parameters such as Reynolds number, wing motion profile, Rossby number and flapping frequency are some of the important kinematic parameters that influence the flapping wing aerodynamics. Prior to moving on to the details of the study conducted on each of them in literature, it is worthwhile becoming familiarised with the terminology used in the literature.

2.1 Terminology

The terminology followed in most of the literature is shown in figure 2.1. The wing span (b) refers to the distance of the tip of the wing from the root of the wing. The chord is measured in the direction perpendicular to the span, from the leading edge to the trailing edge. The wing tip radius or the total span (R) is measured from the axis of rotation to the wing tip. This distance is the sum of the wing-root offset (b_0) and the wing span. The wing aspect ratio ($\mathcal{R}$) is defined as the ratio of the wing span and the mean chord (c).

The flapping stroke of an insect comprises two half-strokes, namely, upstroke and downstroke. During upstroke, the wings move from the front to the dorsal side of the insect body. The wings separate from each other and attain a constant angle of attack. After an initial acceleration, the wings move with constant angular velocity

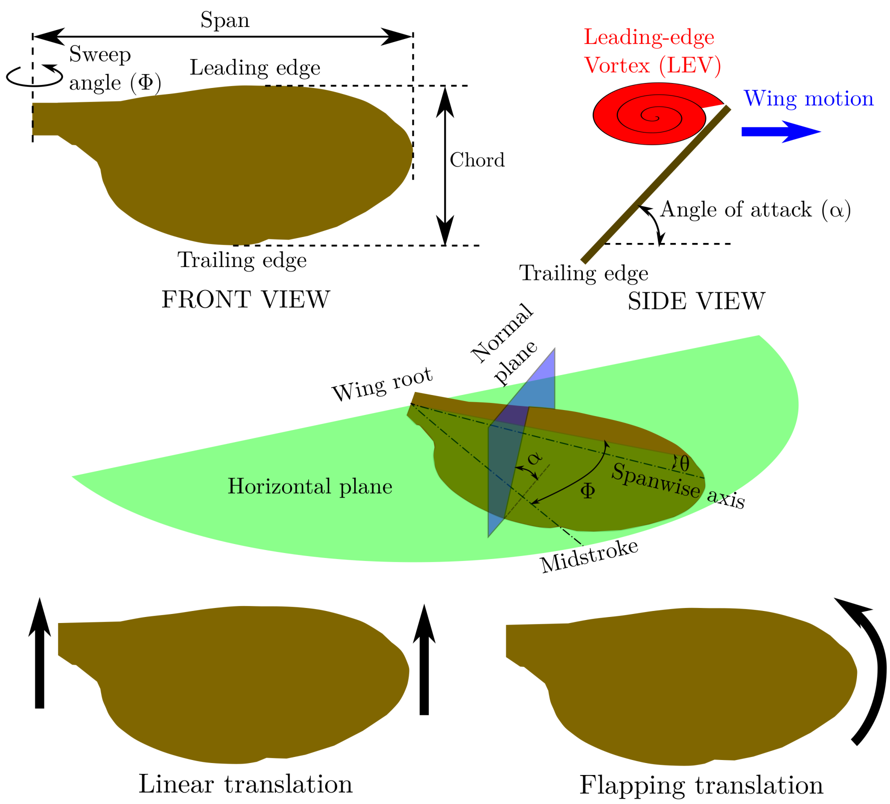

FIGURE 2.1: Terminology followed in the literature.

and then decelerate towards the end of upstroke. During the deceleration, the wings start increasing their angle of attack to flip into the opposite orientation. The constant velocity rotational motion of the wing is referred to as flapping translation or sweep. This translation is different from the linear translation, where the wing moves along a linear axis with a given velocity, as shown in figure 2.1.

In general, an insect wing can flap about three different axes during a stroke, causing it to sweep, pitch and deflect. The rotation angle associated with the sweep is called the sweep angle or stroke angle (ϕ). The angle made by the wing plane with the stroke plane is called the angle of attack (α). During the flapping motion, the wing may move up or down, deflecting it from the stroke plane. The rotation angle associated with this third axis is called the deflection angle (θ). The deflection angle is relatively small in an insect flight. In the case of '*normal hovering*', the deflection is negligible and the wings move approximately in a horizontal plane, as has been described by Weis-Fogh (1973).

The Reynolds number of the flapping wing has been described in different ways by researchers. A generalised expression for the Reynolds number can be written as

$$Re = \frac{U_{ref} l_{ref}}{\nu}, \tag{2.1}$$

where U_{ref} is the reference velocity, l_{ref} is the reference length scale and ν is the kinematic viscosity of the surrounding medium. Some researchers, such as Birch *et al.* (2004), Aono *et al.* (2008b), and Kang & Shyy (2014), use the velocity at the wing tip (U_t) as U_{ref}, whereas other researchers, such as Luo & Sun (2005), Lee *et al.* (2016), and Tudball Smith *et al.* (2017), use the velocity at the radius of gyration (U_g) of the wing as U_{ref}. Inspired by the research on two-dimensional wings and airfoils in the past, almost all the studies on insect wings have used the mean wing chord as l_{ref}. However, Harbig *et al.* (2013) have shown that the wing span is a better choice for l_{ref} as the leading-edge vortex structure on the wing scales uniformly with the Reynolds number based on the wing span. In the present work, U_g is used as the reference velocity. The chord-based and the span-based Reynolds numbers are defined as

$$Re_c = \frac{U_g c}{\nu} \qquad \text{and} \qquad Re_b = \frac{U_g b}{\nu}, \tag{2.2}$$

respectively.

The mechanical and numerical models are constructed such that their Reynolds number and reduced frequency parameter are matched with those of an actual insect. This condition is called 'dynamic scaling', which has facilitated the performance of force and flow field measurements while the underlying aerodynamic phenomena are conserved. Flow measurements and visualisation from these models have helped researchers to understand several unsteady mechanisms associated with the flapping wing (e.g. Sane, 2003; Liu *et al.*, 2017).

2.2 Unsteady flow over a flapping wing

As previously described, the low inertia and high flapping frequency makes the flow over a flapping wing highly unsteady. Different mechanisms associated with the unsteady effects are explained below.

2.2.1 Wagner effect

When an inclined plate starts impulsively from rest, it develops a circulation around it. Due to viscous effects, it takes some time to reach the steady state value of the circulation (Walker, 1931). When the starting vortex has moved sufficiently downstream, the

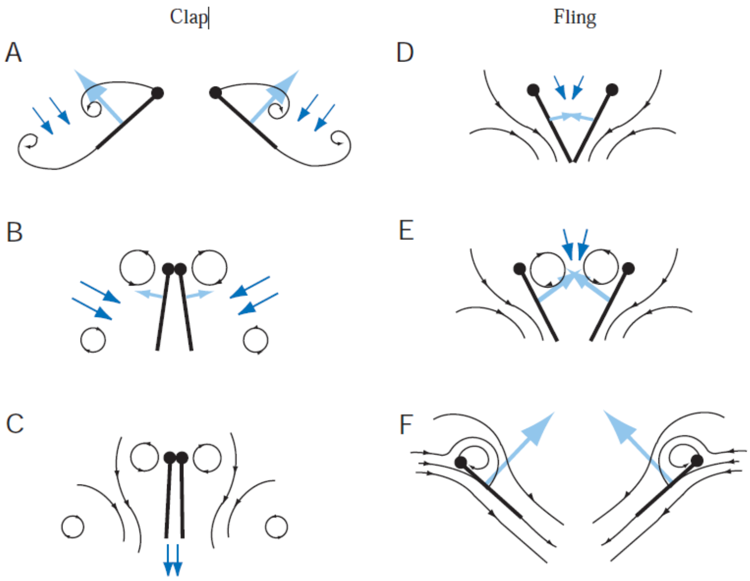

FIGURE 2.2: Clap-and-fling mechanism proposed by Weis-Fogh (1973), illustrations by Sane (2003) (figure reproduced with permission).

wing attains maximum steady state circulation as proposed by Wagner (1925). Thus, the Wagner effect relates to the growth of vorticity at the start of the flapping motion.

2.2.2 Clap and fling

The clap-and-fling mechanism, also known as the Weis-Fogh mechanism, was first proposed by Weis-Fogh (1973). It explains the reason behind the high lift generation during flapping motion of wings of some insects like the small Chalcid wasp *Encarsia formosa*. As shown in figure 2.2 (A-C), at the end of the half stroke, the two wings approach each other. The leading edges touch initially and the wings rotate about the leading edges such that the trailing edges come closer, pushing the fluid between the two downward. This part of the motion is called 'clap'. This is followed by 'fling' (D-F) where wings rotate about the trailing edges separating the leading edges and thus create suction in the gap. This creates an initial boost in circulation around the wings.

2.2.3 Delayed stall and LEV

The clap-and-fling mechanism does not completely explain the high lift production as many insects do not perform a clap (Marden, 1987). Maxworthy (1979) noted for the first time that the presence of a 'Leading-Edge Vortex' (LEV) on insect wings is responsible for producing higher lift. In the case of a linearly translating wing at high

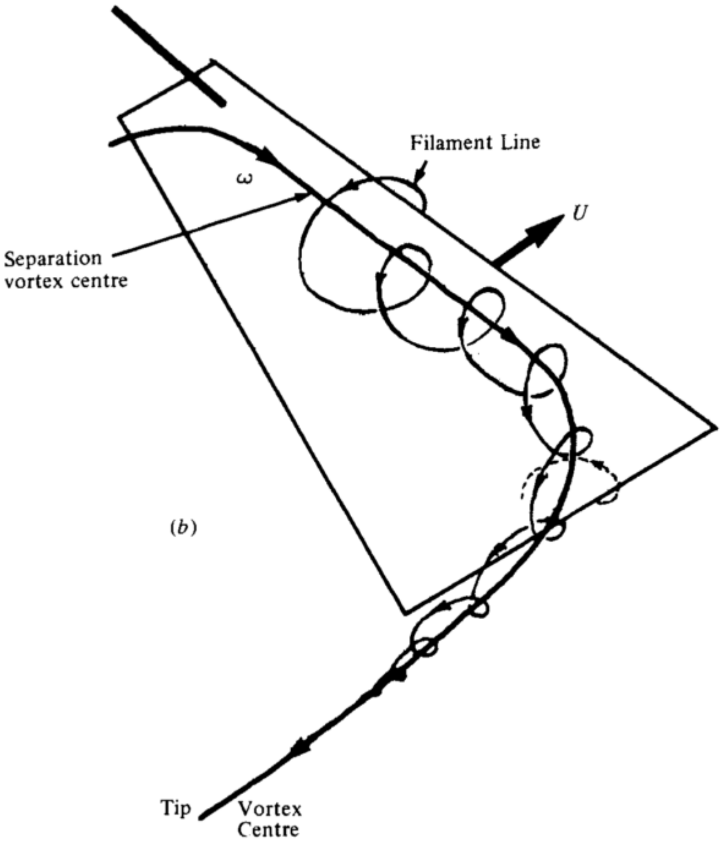

FIGURE 2.3: Sketch of the leading edge vortex (LEV) merging with tip vortex for flinging wing, by Maxworthy (1979) (reproduced with permission).

angles of attack, alternate shedding of leading and trailing edge vortices is observed. However, in the case of flapping translation, the LEV remains stable and thus delays the stall. The axial flow in the vortex feeds vorticity into the tip vortex as shown in figure 2.3. This axial/span-wise momentum transfer helps in reducing the chord-wise momentum and thus the LEV remains smaller. The smaller size allows the flow to reattach and maintain the LEV stable for a longer time. This LEV is shed at the end of a stroke when the wing flips and a new LEV is formed after the wing starts translating back.

Birch *et al.* (2004) measured forces on a rotating model wing of *Drosophila melanogaster* at different Reynolds numbers and observed that the forces remain stable throughout the stroke after initial transients. Thus, the stable lift generation shows that the LEV is stable throughout the stroke. Interestingly, they also observed an intense narrow region of span-wise flow within the LEV core at $Re = 1400$, but not at $Re = 120$.

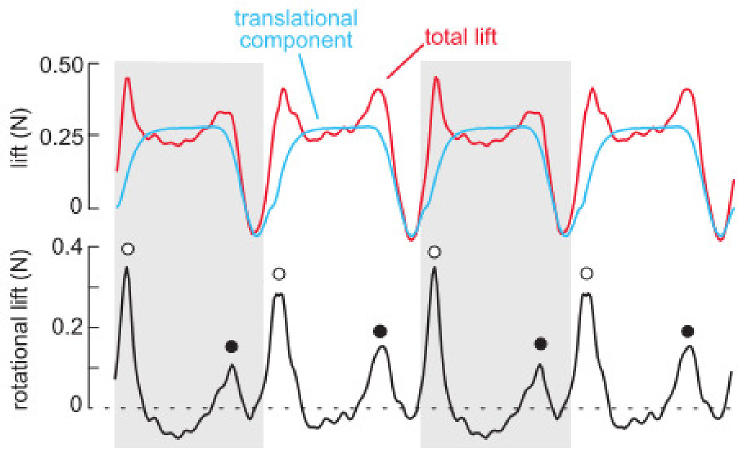

FIGURE 2.4: Two distinct peaks appear in the lift force, due to high lift generated during rotation and wake capture, shown by Dickinson *et al.* (1999)[1].

2.2.4 Magnus effect

Force measurements by Dickinson *et al.* (1999) showed two distinct peaks during flapping motion, separated by a finite time (figure 2.4). This increase in lift in one of the peaks, beyond the steady lift generated by a stable LEV, was explained by the presence of rotational circulation while flipping. As the wing flips near the end of a stroke, it rotates about its span-wise axis while it is in translation. Thus, the early rotation prior to the end of a stroke is similar to backspin, which is responsible for higher lift as explained by the Magnus effect. Thus, the phase of pronation and supination with respect to downstroke and upstroke is important in this case. The speed of the flip also determines the increase in the lift.

2.2.5 Wake capture

Rotational circulation cannot explain the second peak observed at the start of a stroke. The explanation was given by Dickinson *et al.* (1999) with the help of the mechanism of wake capture in which the wing benefits from the vorticity shed in the previous stroke. It was demonstrated that the flow generated in the previous stroke increases the effective velocity at the start of the next stroke, thereby increasing the force production.

[1]Republished with permission of American Association for the Advancement of Science, from Dickinson *et al.* (1999); permission conveyed through Copyright Clearance Center, Inc.

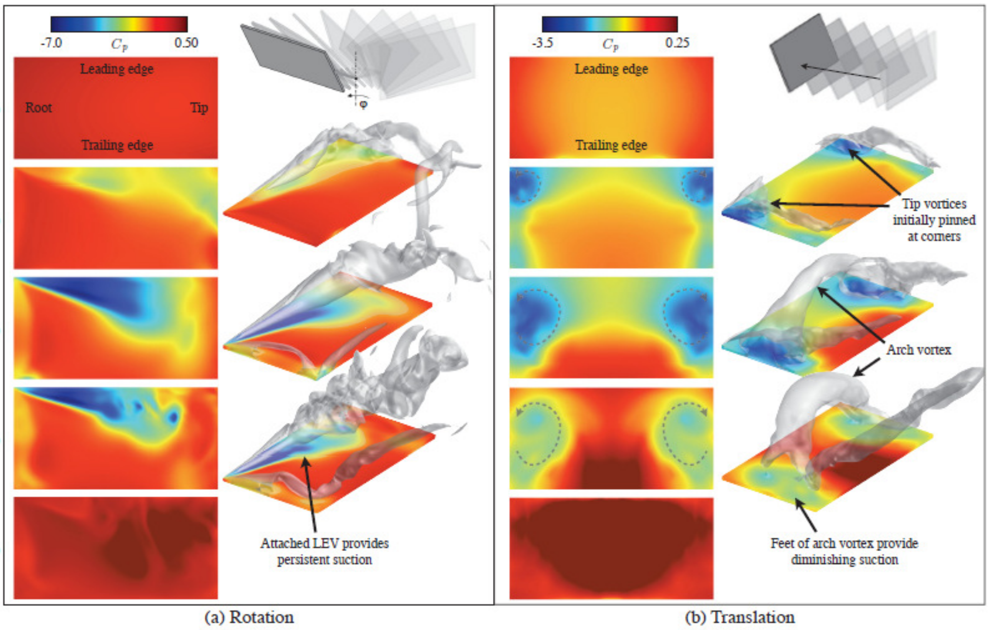

FIGURE 2.5: Rotational translation (a) shows an attached LEV whereas linear translation (b) shows an unsteady arch vortex. There is a clear difference between the pressure developed on the wing surface in the two cases (Garmann & Visbal, 2013)[2].

2.2.6 Linear flapping and rotational flapping

The aerodynamics of 2-D sections of flapping wings is addressed widely in the literature, including the classical work by Garrick (1936), Lighthill (1970) and Wu (1971). Since the present work addresses rotational flapping of a finite wing, it is important to distinguish between linear flapping and rotational flapping. A finite wing has the wing tip at a finite span that is responsible for the spanwise component of the velocity. In the case of 2-D sections flapping linearly, the wing is assumed to be infinite in the spanwise dimension and thus the flow velocity has components only in the plane of the section. This assumption may be useful in the study of flight with wings of high aspect ratios. However in small flyers, especially in insects, the aspect ratios are small and thus the flow has a 3-D structure.

2-D wing sections at a high angle of attack are observed to shed vortices alternately from the leading and the trailing edge forming a von Kármán vortex street. On the other hand, a rotationally flapping wing has a stable LEV during its translation, as described in an earlier section. Garmann & Visbal (2013) systematically studied the

[2]The figure is in public domain as a declared work of the U. S. government.

difference between linear and rotational flapping (figure 2.5) and found that a linearly translating wing generates 32% less cycle-averaged lift than does the rotational translation. Moreover, Kim & Gharib (2010) have observed a difference in the location of the spanwise flow over the wing between a translating and a rotating wing. Inspired by flapping wings of insects, the present work focuses on the rotational flapping.

2.3 Leading-edge vortex structure

The LEV is a peculiar flow feature of the wing in rotational translation. When observed along the spanwise direction, the LEV grows in size from the wing root towards the wing tip. The LEV is spiral in nature, transporting the vorticity along the spanwise direction, which merges with the tip vortex and tilts into the wake. Due to the small aspect ratios of the insect wings, a horseshoe-shaped vortex (HSV) is formed that comprises the LEV, a tip vortex (TV) and a trailing-edge vortex (TEV), as can be seen in figure 2.6. The HSV is stronger at low Reynolds number ($Re \sim 10^3$) than at higher Reynolds numbers. Liu *et al.* (2018) have performed *Schlieren* photography to record the HSV structure over a free-flying Hawkmoth wings, flapping typically at $Re \sim 5000$. For such higher Reynolds numbers and with a high α, the LEV bursts into small incoherent structures (Lentink & Dickinson, 2009b; Jones *et al.*, 2016) at a certain location along the span. This vortex burst can be characterised by the stagnation in the axial flow and the entrainment of the opposite-sign vorticity.

In rotational translation, the LEV initially starts growing in size during the initial acceleration. If the wing is rotated with a constant angular velocity, the LEV reaches a certain size until the rotation angle $\phi = 90°$ and then maintains a stable size. This initial growth and the stability of the LEV is evident from the sectional spanwise circulation (Γ_z^*) of the LEV tracked at various rotation angles. Elimelech *et al.* (2013) and Achache *et al.* (2017) have shown that Γ_z^* initially increases until $\phi = 90°$, followed by a stable value. The reason behind the stability of the LEV has been a topic of debate among the researchers. Ellington *et al.* (1996) associated it with the spanwise flow through the LEV core. This was challenged by Birch & Dickinson (2001), who artificially limited the spanwise flow over a wing with baffles and observed that the LEV still remained attached. They hypothesised that the LEV growth was limited by the downwash induced by the tip vortex. Later, Lentink & Dickinson (2009a) and Jardin (2017) showed that the Coriolis effects were responsible for the LEV stability, whereas

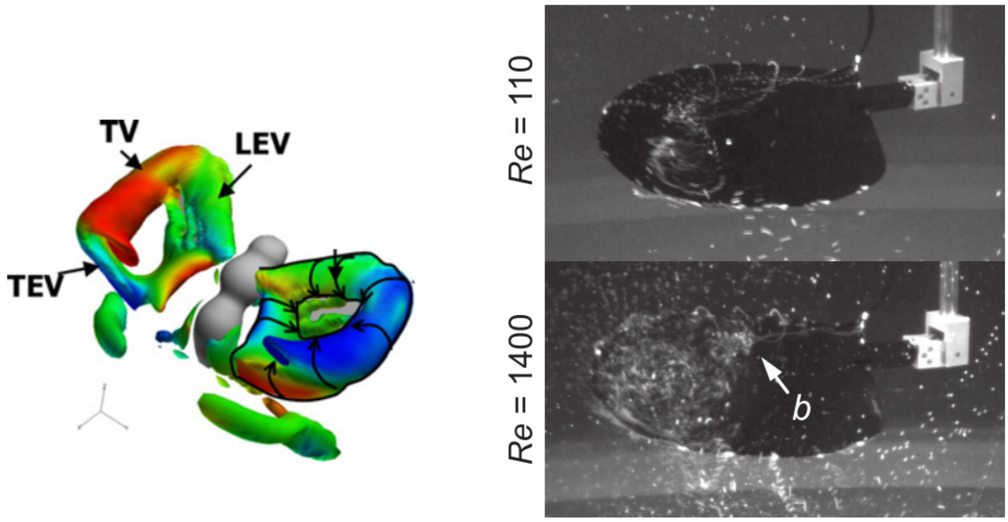

Horseshoe vortex (HSV) Bursting of the LEV

FIGURE 2.6: The horseshoe vortex structure (HSV) shown by Liu & Aono (2009) and the LEV bursting at $Re = 1400$ shown by Lentink & Dickinson (2009b) (both figures reproduced with permission).

Garmann & Visbal (2014) observed the centrifugal and pressure gradient forces to be responsible for the spanwise flow that stabilised the LEV.

The simultaneous flow separation over the wings and thorax of an insect can result in different LEV topologies, depending on the Reynolds number and wing morphology (Bomphrey, 2006). Srygley & Thomas (2002) observed the LEV to be extending from one wing tip to the other wing tip across the thorax of a butterfly, with a cylindrical shaped core. Ellington *et al.* (1996) observed two independent LEVs with spanwise flows occurring through the LEV cores on two wings of a hawkmoth. Bomphrey *et al.* (2005) observed that the LEV structure changes for these wings during the downstroke, by virtue of a shift of the spanwise flow towards midchord location.

2.3.1 Existence of dual-LEVs

While studying the LEV on a free flying butterfly, Srygley & Thomas (2002) first observed '*two subparallel leading-edge vortices*'. These vortices originate from single LEV, which splits into two vortices at a certain spanwise location. This structure is called the dual-LEVs. This existence of the dual-LEVs for a wide range of $A\!\!R$ and Re was confirmed experimentally by Lu *et al.* (2006). The dual structure is observed for $\alpha > 30°$ and $Re > 600$.

Lu *et al.* (2006) discussed several reasons behind the existence of the two vortices.

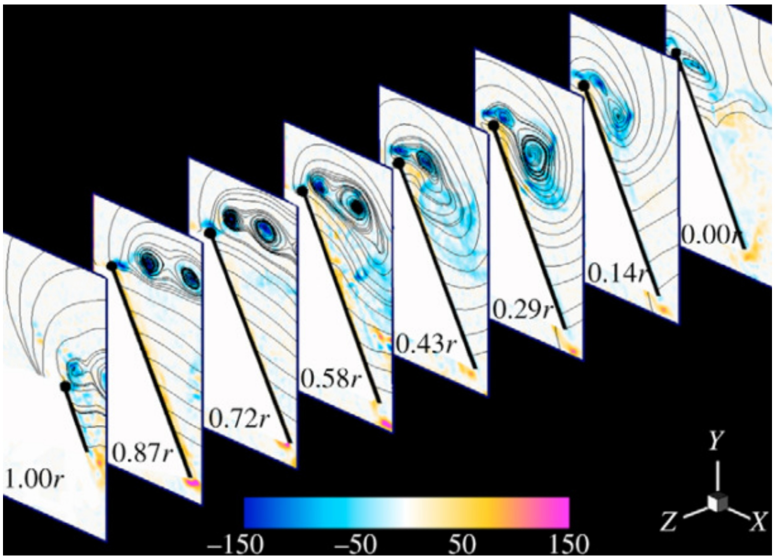

FIGURE 2.7: 2-D PIV images taken at different span-wise locations by Lu *et al.* (2006) show single LEV formed at the root (right hand side), which separates into two vortices towards the tip (left hand side) (figure reproduced with permission).

First, they observed the secondary separation of the opposite sign vorticity to that of the LEV to induce the outboard separated flow to form a minor vortex. Second, the shear layer, outboard from the minor vortex, of the negative sign vorticity also plays a role transporting the vorticity to the minor vortex. Figure 2.7 shows the dual LEVs where the primary vortex remains attached and the secondary vortex is shed as the wing rotates. Later, Hu & Wang (2011) also observed the dual-LEVs over a butterfly wing in forward sweep, even at low angles of attack ($\alpha = 8° - 12°$).

Lu *et al.* (2006) did not find the LEV structure to be sensitive to Æ but later Harbig *et al.* (2013) showed that it is insensitive to Æ only when Re is calculated based on the wing span. The effect of Æ is a subject of debate even in current studies, which will be discussed in subsequent sections.

2.4 Effect of kinematic and geometrical parameters

To understand the effects of different parameters on the acceleration of fluid around a flapping wing, the Navier-Stokes equations are revisited, following the similar method as of Lentink & Dickinson (2009a). The flow over a flapping or a rotating wing can be analysed by the Navier-Stokes equations cast in a non-inertial rotating frame of reference, which can be written as

$$\rho\frac{\mathrm{D}\boldsymbol{u}}{\mathrm{D}t}+\rho\dot{\boldsymbol{\Omega}}\times\boldsymbol{r}+\rho\boldsymbol{\Omega}\times(\boldsymbol{\Omega}\times\boldsymbol{r})+\rho2\boldsymbol{\Omega}\times\boldsymbol{u}=-\boldsymbol{\nabla}p+\mu\boldsymbol{\nabla}^2\boldsymbol{u} \tag{2.3}$$

and

$$\boldsymbol{\nabla}\cdot\boldsymbol{u}=0, \tag{2.4}$$

where ρ is the density of the fluid, $\boldsymbol{u}$ is the velocity in the rotating frame, $\boldsymbol{\Omega}$ is the angular velocity, $\dot{\boldsymbol{\Omega}}$ is the angular acceleration, $\boldsymbol{r}$ is the radial location, p is the pressure, and μ is the fluid dynamic viscosity. The first term in equation 2.3 involves the material derivative of the velocity vector, whereas the next three terms are the angular, centripetal and Coriolis acceleration terms, respectively. $\boldsymbol{\nabla}p$ is the pressure gradient term and the last term is the diffusion term. Lentink & Dickinson (2009a) have scaled the terms using

$$\boldsymbol{u}^*=\frac{\boldsymbol{u}}{U},t^*=\frac{Ut}{c},\boldsymbol{\nabla}^*=c\boldsymbol{\nabla},\boldsymbol{\Omega}^*=\frac{\boldsymbol{\Omega}}{\Omega},\dot{\boldsymbol{\Omega}}^*=\frac{\dot{\boldsymbol{\Omega}}}{\dot{\Omega}},\boldsymbol{r}^*=\frac{\boldsymbol{r}}{R},p^*=\frac{p}{p_0}, \tag{2.5}$$

where U is the wing tip velocity, c is the mean wing-chord, Ω is the time averaged angular velocity, $\dot{\Omega}$ is the time averaged angular acceleration, R is the wing tip radius (or the total span), and p_0 is the ambient pressure. Using this scaling and omitting the symbol '*' for simplicity, equation 2.3 can be written in a dimensionless form as

$$\frac{\mathrm{D}\boldsymbol{u}}{\mathrm{D}t}+\frac{\dot{\Omega}Rc}{U^2}\dot{\boldsymbol{\Omega}}\times\boldsymbol{r}+\frac{\Omega^2Rc}{U^2}\boldsymbol{\Omega}\times(\boldsymbol{\Omega}\times\boldsymbol{r})+\frac{\Omega^2Rc}{U^2}2\boldsymbol{\Omega}\times\boldsymbol{u}=-\frac{p_0}{\rho U^2}\boldsymbol{\nabla}p+\frac{\mu}{\rho Uc}\boldsymbol{\nabla}^2\boldsymbol{u}. \tag{2.6}$$

Harbig *et al.* (2012), Lee *et al.* (2016), and Tudball Smith *et al.* (2017) have used the velocity at the radius of gyration (U_g) as the reference velocity. The radius of gyration (R_g) is the radius of the second moment of the wing area, which is a measure of wing shape (Ellington, 1984b). It is defined as

$$R_g=\frac{1}{S}\int_0^R c(\boldsymbol{r})\boldsymbol{r}^2d\boldsymbol{r}, \tag{2.7}$$

where S is the wing area.

Using U_g as the reference velocity, equation 2.6 can be re-written as

$$\frac{\mathrm{D}\boldsymbol{u}}{\mathrm{D}t}+\frac{\dot{\Omega}Rc}{U_g^2}\dot{\boldsymbol{\Omega}}\times\boldsymbol{r}+\frac{\Omega^2Rc}{U_g^2}\boldsymbol{\Omega}\times(\boldsymbol{\Omega}\times\boldsymbol{r})+\frac{\Omega c}{U_g}2\boldsymbol{\Omega}\times\boldsymbol{u}=-\frac{p_0}{\rho U_g^2}\boldsymbol{\nabla}p+\frac{\mu}{\rho U_g c}\boldsymbol{\nabla}^2\boldsymbol{u}. \tag{2.8}$$

It can be estimated from this equation that the angular acceleration term can be influenced by the flapping motion profile of the wing. The centripetal acceleration term has a coefficient (Ω^2Rc/U_g^2), which can be simplified as

$$\frac{\Omega^2Rc}{U_g^2}=\frac{Rc}{R_g^2}=\frac{\mathcal{R}}{Ro^2}, \tag{2.9}$$

where $\mathcal{A}\!\!R$ is the aspect ratio ($\mathcal{A}\!\!R = R/c$) and Ro is the Rossby number ($Ro = R_g/c$). The Coriolis acceleration term is influenced by the term ($\Omega c/U_g$) which can be simplified as

$$\frac{\Omega c}{U_g} = \frac{c}{R_g} = \frac{1}{Ro}. \tag{2.10}$$

The diffusion term scales with Reynolds number (defined as $Re = \rho U_g c/\mu$).

Thus, from several kinematic and geometrical parameters that influence the flapping wing aerodynamics, the important parameters are the wing aspect ratio ($\mathcal{A}\!\!R$), Reynolds number (Re), motion profile, and Rossby number (Ro). Moreover, the wing shape can also be deformed by the flow, depending on the flexibility of the wing, which may cause a change in the flow structure itself. The effects of these parameters studied by researchers in the past are discussed in detail in the following subsections.

2.4.1 Reynolds number (Re)

It is evident from Table 2.1 that different insects fly at different Reynolds numbers. It has been unanimously agreed that the aerodynamic force coefficients increase with an increase in Re (Birch *et al.*, 2004; Harbig *et al.*, 2013; Carr *et al.*, 2015). The Reynolds number directly influences the formation of the LEV structure and hence the performance of the flapping wing. As discussed in an earlier section, dual-LEVs are observed for $Re > 600$. This was confirmed by the numerical study conducted by Harbig *et al.* (2013). They observed a clear difference in the LEV structure at four different Reynolds numbers, as shown in figure 2.8. The LEV is observed to be stable throughout the stroke at low Re whereas it breaks up at higher Re. Birch *et al.* (2004) observed an intense narrow region of span-wise flow at higher Re but not at lower Re. Their study at low Re led to the conclusion that LEV stability does not necessarily depend on the span-wise flow.

Vortex bursting occurs when a vortex breaks to form smaller, noncoherent structures. In the case of rotating and flapping wings, the burst occurs when the spanwise velocity approaches stagnation. The LEV burst has also been observed as a function of Re (Shyy & Liu, 2007). The location of the LEV bursting point is observed to be radially more inward at higher Re. Thus, a fruit fly wing, having a weaker LEV at a lower Re, maintains the LEV structure intact compared to that of a hawkmoth wing at a higher Re.

Studies using computational models for a fruit fly wing and a Hawkmoth wing

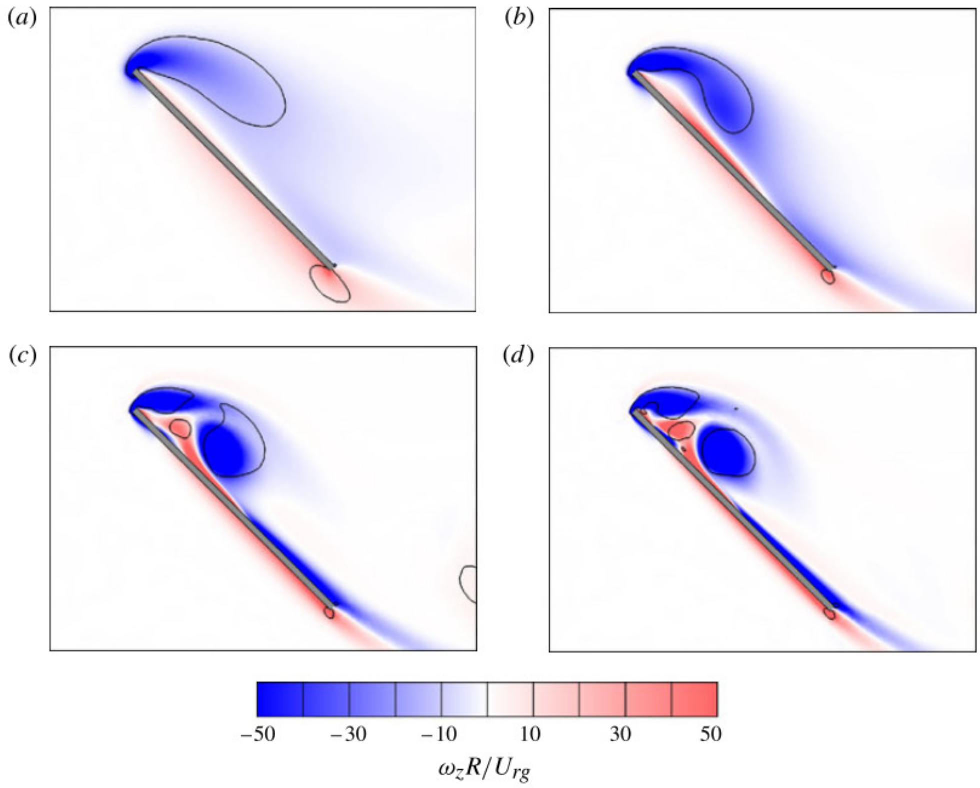

FIGURE 2.8: Vorticity plot at 50% span of a rotating wing by Harbig *et al.* (2013) shows the difference between LEV structure at Reynolds number of (a) 120, (b) 300, (c) 750 and (d) 1500 (reproduced with permission).

flapping at their respective Reynolds numbers confirmed that the influence of the span-wise flow is more evident at high Re (e.g. Liu *et al.*, 1998; Aono *et al.*, 2008a; Liu, 2009; Liu & Aono, 2009). A detailed analysis by Wojcik & Buchholz (2014) demonstrated that the span-wise convection of vorticity is insufficient to balance the vorticity flux through the leading-edge shear layer. They found the vorticity annihilation due to interaction between the LEV and the opposite-sign layer on the wing surface to be an important mechanism for LEV circulation.

Liu & Aono (2009) observed that the fruit fly wing, having a low Re, has the peak spanwise pressure gradient always close to the leading edge, driving the LEV towards the wing tip. However, a hawkmoth wing, having a high Re, has the peak pressure gradient shifting towards the trailing edge near the midspan region, causing the LEV to tilt at a more inboard location than that at a lower Re. Han *et al.* (2014) observed that, in the case of flapping wings, the centre of pressure (C.P.) on the wing surface moved towards the trailing-edge root as the wings flipped. However, the movement of

C.P. at a high Re is only gradual compared to that at a low Re. Therefore, it was concluded that the response to the rotational lift during the flip motion was immediate in the low-Re case.

2.4.2 Motion profile

The wing flapping motion is characterised by wing beat frequency (f), stroke amplitude (ϕ_{max}), phase of rotation and velocity profile. Dudley & Ellington (1990) observed the flapping kinematics of bumblebees by filming them in their actual flight in a wind tunnel. Their flapping stroke amplitude was not affected significantly with the wind speed. However, the bee's body was observed to tilt in the response, so as to adjust the thrust and the lift to have a stable flight. Ellington (1984b) obtained the timetraces of the stroke angles for various insects. The stroke amplitudes (peak-to-peak) were mostly less than 180°, eliminating the possibility of *clap-and-fling*. For a fixed amplitude, as the frequency increases, the mean lift and drag forces increase with a scaling roughly proportional to f^2 (Ansari *et al.*, 2008a). Increase in stroke amplitude linearly increases the mean lift and drag. Berman & Wang (2007) built an analytical model for determining the optimal wing kinematics for a fruit fly, bumble bee and hawkmoth. They found that the frequency, that minimised the power consumption, while producing just enough lift to balance the weight in hovering, was close to that observed in nature.

The effect of flip timing and flip duration was first studied by Sane & Dickinson (2001). The Magnus effect, as described in the earlier section, depends upon the phase of flipping with respect to translation and flip duration. The lift force was observed to be maximised by short-duration flips occurring slightly in advance of stroke reversal (Dickinson *et al.*, 1999; Gogulapati *et al.*, 2014). The mean lift generated by rotation after stroke reversal was found to be very low. Further investigation by Bross & Rockwell (2014) showed that in pure rotation, the coherence of the tip vortex is substantially degraded whereas the flipping motion helps in maintaining the coherence of the tip-LEV system.

Bos *et al.* (2008) numerically analysed four different kinematic models for the wing motion profile. This involved harmonic motion, robofly experimental kinematics, actual fruit fly kinematics and simplified fruit fly kinematics. The mean aerodynamic drag at equal lift was found to be significantly lower for a real fruit fly than other models. Another realistic feature is the wing deviation from the stroke plane, which is found to have only a marginal effect on the mean lift and drag.

Various optimisation techniques have also been used to obtain the optimised flight of MAVs (Rakotomamonjy *et al.*, 2007; Ghommem *et al.*, 2013; Wang *et al.*, 2013). These studies have found the optimum parameters, such as the amplitudes in rotational translation and pitch, frequency and timing of reversal for MAV wings. Taha *et al.* (2013) found that the harmonic waveform required 20% more aerodynamic power than the robofly (triangular) waveform. However, since the force prediction models on the flapping wings are not robust, the applicability of the optimisation models, which include the force predictions, is limited.

2.4.3 Aspect Ratio ($\mathcal{R}$)

As described in §2.1, the aspect ratio ($\mathcal{R} = b/c$) is an important geometrical feature in flapping wing aerodynamics. It is one of the most studied and yet debatable parameters in the literature. Usherwood & Ellington (2002) reported a decrease in the horizontal force and a negligible effect on the vertical force with an increase in $\mathcal{R}$. Luo & Sun (2005) investigated ten different insect wing shapes in the range of $\mathcal{R}$ values from 2.8 to 5.5 rotating at a constant angular velocity. They observed that $\mathcal{R}$ has a minimal effect on the force coefficients if the velocity at the radius of the second moment of wing area is used as a reference velocity. Garmann & Visbal (2014) also observed very little variation in the lift coefficient (C_L) by simulating rotating rectangular wings of $\mathcal{R}$ 1,2, and 4. However, they observed the evolution of the LEV structure to be affected significantly with $\mathcal{R}$. As can be seen in figure 2.9, for higher $\mathcal{R}$, the LEV interacts with the wing surface post its breakdown, which creates undulations of the LEV core. Moreover, the LEV for higher $\mathcal{R}$ extends in the chordwise direction to reach the trailing edge, which hinders its growth in the spanwise direction.

Some researchers, on the other hand, observed a variation in the forces acting on the wing with a change in $\mathcal{R}$. Ansari *et al.* (2008b) simulated the flapping motion of wing planforms obtained by various combinations of wing shapes and aspect ratios. By maintaining a constant wing-area for all the wing planforms, they observed that the lift force increased with $\mathcal{R}$ for all the wing shapes, except the triangular wing for which the lift was nearly unaffected. Harbig *et al.* (2012) observed a maximum C_L for $\mathcal{R} = 5.1$ and a decrease in C_L with a change in $\mathcal{R}$ on both the lower and the higher sides, whereas Han *et al.* (2015) obtained a maximum C_L for the wing of $\mathcal{R} = 3$. Among the

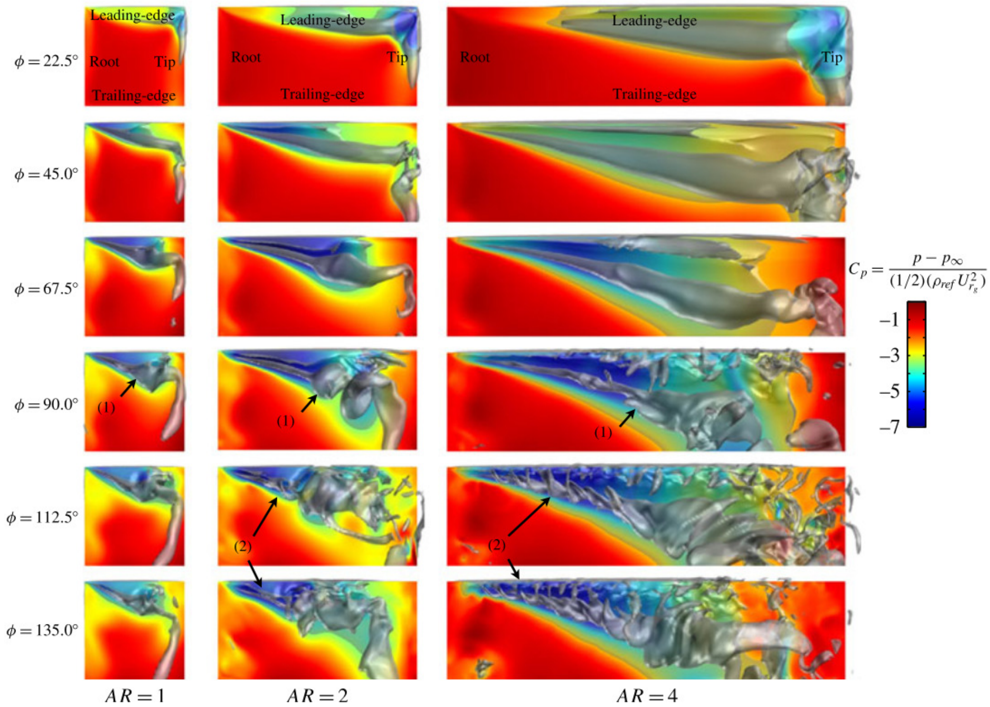

FIGURE 2.9: Garmann & Visbal (2014) showed that, after a certain rotation angle (ϕ), the LEV at higher Æ extends in chordwise direction to reach the trailing edge. The LEV breakdown (1) occurs at the midspan in all the cases. However, the undulations in the LEV core (2) are observed only for high Æ cases (figure reproduced with permission).

Æ values in the range 1.5 to 8, they suggested that the wing of Æ $= 3$ had the best aerodynamic performance, as can be seen in figure 2.10(a).

In an experimental study, Kruyt *et al.* (2015) rotated rectangular wings of Æ values in the range 2 to 10 at relatively high Reynolds numbers ($Re \sim 10^4$). For a high angle of attack, they proposed that the LEV remains attached for the normalised wing tip radius $R/c < 4$. By studying different aspect ratios ($1.5 \leq$ Æ ≤ 7.5) for three different wing shapes, Shahzad *et al.* (2016) observed that the trend in the variation of C_L depends on its scaling. They showed that using the tip velocity (U_t) as the reference, C_L decreases with an increase in Æ; however, using the velocity at the radius of gyration (U_g) as the reference, C_L increases with Æ in a lower range and remains relatively unchanged for Æ > 6. Phillips *et al.* (2015) showed an increase in the mean C_L computed from the LEV-circulation obtained from their PIV experiments, whereas Shahzad *et al.* (2016) showed a decrease in the mean C_L, which can be seen in figure 2.10(b). Ozen & Rockwell (2013) proposed that the organised swirl of the LEV degraded with an increase in Æ.

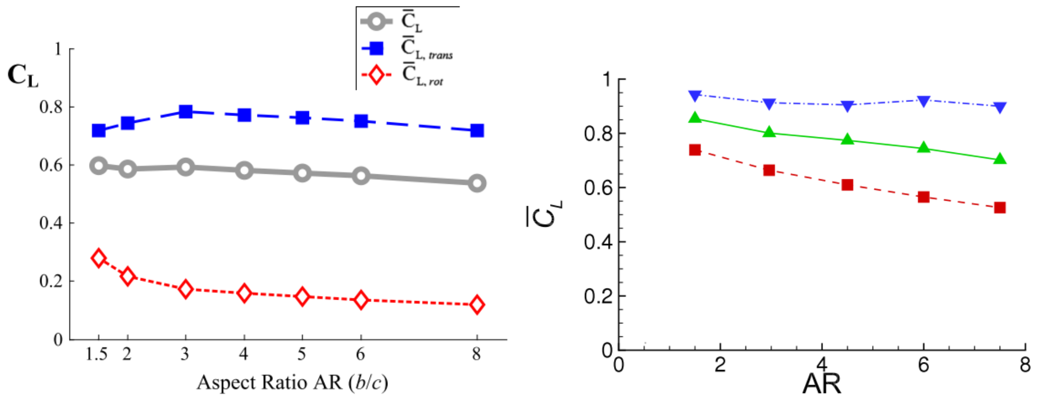

FIGURE 2.10: In (a), Han *et al.* (2015)[3] have shown the lift coefficient in translation to be maximum for $A\!\!R = 3$, whereas in (b), Shahzad *et al.* (2016)[4] have shown a monotonic decrease in the lift coefficient with an increase in $A\!\!R$. Here, the lift coefficients are calculated based on the wing tip velocity.

They also noted that the positive spanwise flow moved towards the trailing-edge for higher $A\!\!R$ values.

Remarkably, Harbig *et al.* (2013) observed a change in LEV structure with AR similar to that observed with a change in Re and proposed a decoupling of the two parameters by scaling Reynolds number based on span. This scaling of the Reynolds number (Re_b) indeed showed insensitivity of the LEV structure to $A\!\!R$, as shown in figure 2.11. With this scaling, at relatively higher values of Re_b ($\sim 10^3$), they observed that C_L remained relatively unaffected with an increase in aspect ratio in the range $A\!\!R \leq 5.1$, beyond which it started reducing. However, at a low Re_b ($\sim 10^2$), C_L decreased monotonically with an increase in $A\!\!R$.

Carr *et al.* (2015) verified this scaling of Reynolds number with experiments. However, they observed different split locations for the LEV with a change in AR. An interesting relation between angle of attack (α) and $A\!\!R$ by Kruyt *et al.* (2015) showed that for $\alpha > 20^0$, the wing with $AR = 4$ outperformed the wing with $AR = 10$ in terms of the force coefficients. But for $\alpha < 20^0$, the $AR = 10$ wing outperformed the $AR = 4$ wing. It should be noted that the Reynolds number in these experiments were very high ($Re_b \sim 27,000$). This can help explain why revolving helicopter blades have lower α than hovering insect wings.

[3]Republished with permission of SPRINGER-VERLAG, from Han *et al.* (2015); permission conveyed through Copyright Clearance Center, Inc.

[4]Reprinted from Shahzad *et al.* (2016), with the permission of AIP Publishing.

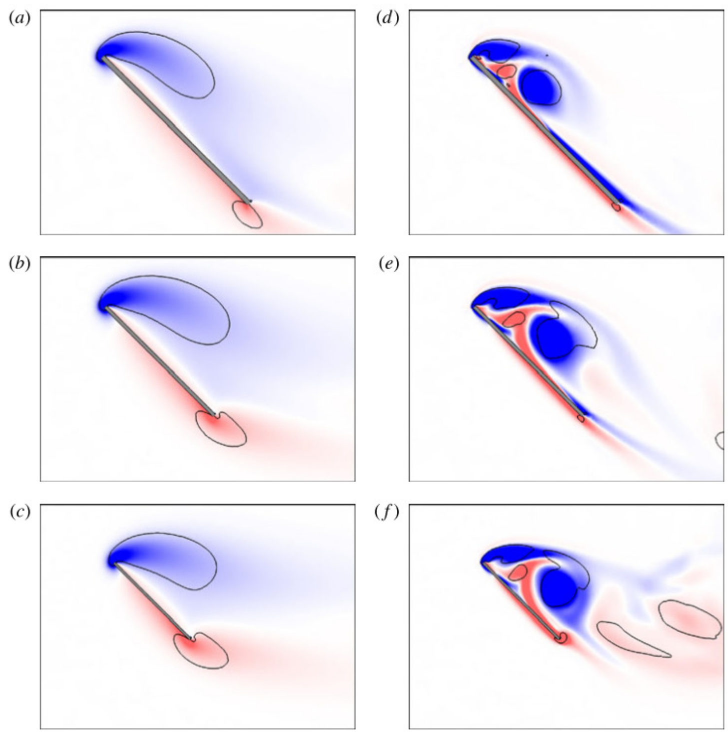

FIGURE 2.11: Span-wise vorticity ($\omega_z s/U_g$) contours for 3 different ARs (2.91, 5.1 and 7.28) at the different Reynolds numbers $Re_b = 613$ (a,b,c) and $Re_b = 7667$ (d,e,f) by Harbig *et al.* (2013). Scaling of Reynolds number with span decoupled the effect of AR (reproduced with permission).

2.4.4 Central body size and Rossby number

It could be expected that LEV formation and its spanwise growth might be affected by the presence of the insect body at the centre of rotation. The central body causes the wing root to offset from the axis of rotation by an amount ($b_0 = d/2$), where d is the diameter of the body. The body size (both length and diameter) of adult insects vary over a large range. The length, for example, of *Hymenoptera*, a large order of insects with membrane wings, varies from 0.15 to 60 mm and that of *Coleoptera*, or beetles, varies from 0.25 to 180 mm (Minelli *et al.*, 2010). The maximum size of their bodies is limited by their individual tracheal respiration systems (Harrison *et al.*, 2010). The wings grow mostly after the body is fully grown and the wing size adjusts to the body size (Nijhout & Callier, 2015).

The weights of insects directly depend on their body sizes, requiring different lift forces for flight. A higher lift may be obtained with a larger wing area and a change

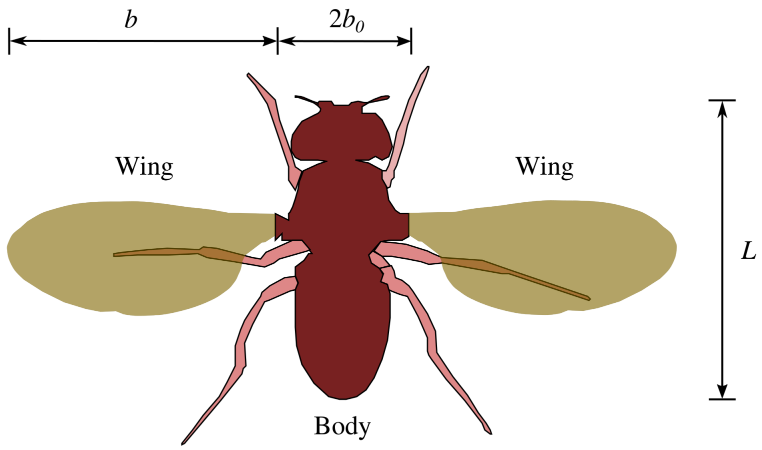

FIGURE 2.12: The schematic of a fruit fly (*Drosophila Melanogaster*), adopted from `https://bugguide.net/node/view/204667`, shows its central body size with respect to the wing size.

in wing kinematics. This causes a significant change to the Reynolds number, which affects the near-field and far-field vortex structures, as shown by Liu & Aono (2009). Even the fully grown fruit flies of four different species have different sizes and weights, and fly at four different Reynolds numbers in the range $[70 < Re < 270]$ (Lehmann, 2002).

The fruit fly body and wing dimensions are shown by a schematic in figure 2.12. The insect dimensions can be normalised using chosen length scales. Ellington (1984a) has reported such normalised lengths and diameters for a wide range of insects. Thus, the *normalised offset*, which is defined as the ratio of the offset and the wing span ($\hat{b}_0 = b_0/b$), can be calculated for all these insects, as shown in table 2.2. For a wide range of insect species, the normalised offset values are found in the range $(0.035 < \hat{b}_0 < 0.14)$. An increase in the offset changes the radius of gyration (R_g), resulting in a change in rotational acceleration terms acting across the wing. This may affect the stability of the LEV.

The effects of the change in the insect body size relative to its wings do not appear to have been studied, although there are some numerical studies showing the effects of the presence of the insect body. Lee *et al.* (2012) and Liu *et al.* (2016) observed the differences between force production on model wings with and without an insect body, and concluded that the total lift production increased in the presence of the insect body. As can be seen in figure 2.13, different LEV topologies have been obtained for the cases

Species	$\hat{L} = \frac{L}{b}$	$\hat{d} = \frac{2b_0}{L}$	$\hat{b}_0 = \frac{\hat{L}\hat{d}}{2}$
Coleoptera			
Coccinella	0.73	0.26	0.095
Diptera			
Tipula obsoleta	0.85	0.11	0.047
T. paludosa	1.04	0.10	0.052
Episyrphus	1.10	0.16	0.088
Eristalis	1.22	0.20	0.122
Hymenoptera			
Apis	1.62	0.17	0.138
Psithyrus and *Bombus*	1.47	0.18	0.132
Lepidoptera			
Emmelina	0.78	0.12	0.047
Manduca	0.81	0.16	0.065
Neuroptera			
Pterocroce	0.77	0.10	0.039
Chrysopa	0.68	0.12	0.041

TABLE 2.2: The data for normalised mean insect body lengths ($\hat{L}$) and mean insect body diameters ($\hat{d}$) are obtained from Ellington (1984a) and the normalised offsets ($\hat{b}_0$) are calculated using these data.

with and without the presence of the insect body. The strong vortices, namely, the thorax vortex (TXV) and the posterior body vortex (PBV), are not present in the case without the body.

Wan *et al.* (2015) investigated cicada aerodynamics in forward flight and observed that the vortex generated from the cicada thorax enhanced the overall lift. Bomphrey *et al.* (2005) performed the smoke flow visualisations and PIV analysis of the LEVs over the wings of real insects flying in a wind tunnel. They identified different LEV topologies for different insects.

The presence of a central body is unavoidable in experimental models. The central shaft and a connecting rod cause the wing to be offset, resulting in a change in the Rossby number ($Ro = R_g/c$). As discussed in § 2.4, the Rossby number could influence the centripetal and Coriolis acceleration terms which are responsible in stabilising the LEVs. Wolfinger & Rockwell (2014) have systematically varied the radius of gyration by extending the length of the connecting rod and found that the vortex system degraded rapidly with an increase in the Rossby number, reflecting a change to the relative influence of the rotational acceleration to other force components. With an increasing

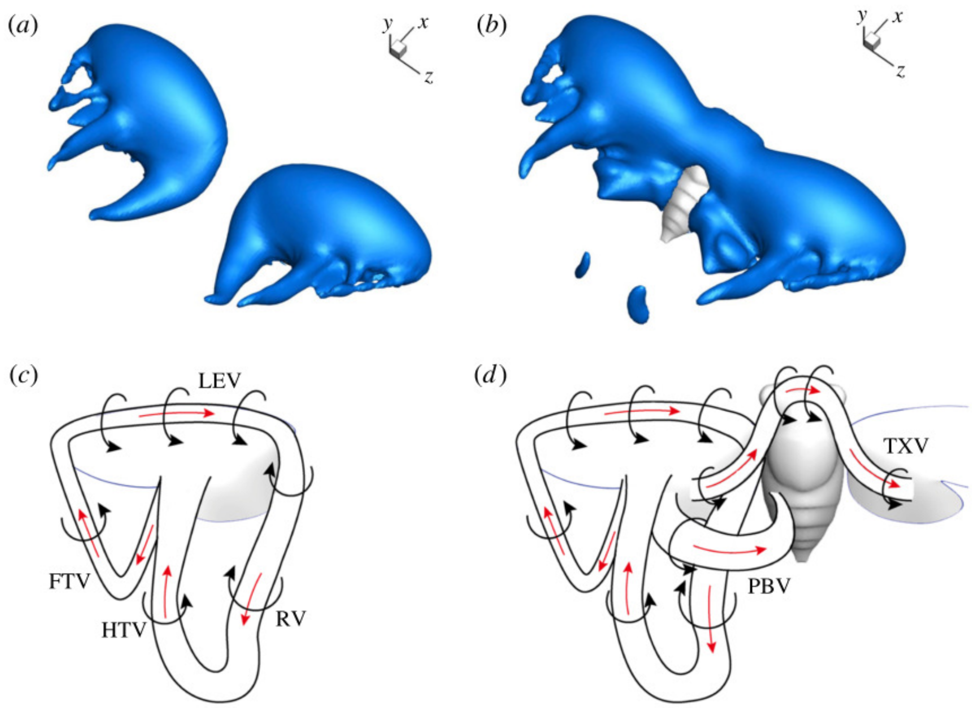

FIGURE 2.13: A comparison of the LEV topologies has been identified in terms of the isosurfaces of pressure coefficient ($C_p = -0.2$) by Liu *et al.* (2016) for the wings without an insect body (a) and with the body (b). The corresponding schematic of the wakes has been shown in (c) and (d) (reproduced with permission).

Ro, the flow structure approached that for the translating wing case, as can be seen in figure 2.14.

Tudball Smith *et al.* (2017) have observed a variation in the lift coefficients for a rotating wing over a wide range of Rossby numbers ($0.7 < Ro < 9$). By observing the time traces of the lift coefficients for the different cases, they have confirmed that the lift reduces with an increase in Rossby number. Also, the flow over the wing at a high *Ro* approached a near-symmetric flow of a translating wing, as can be seen in figure 2.15. However, in the experimental studies in the past, the central body size was not changed, whereas the radius of gyration was changed by varying the length of the connecting rod. Moreover, in most of these studies, since the connecting rod was attached to the centre of a rectangular wing's root, the LEV might be unaffected by the secondary flow.

In the aspect ratio studies, for example, Kruyt *et al.* (2015) observed an optimum performance for the wing with $Æ \sim 4$, whereas Garmann & Visbal (2014), Carr *et al.*

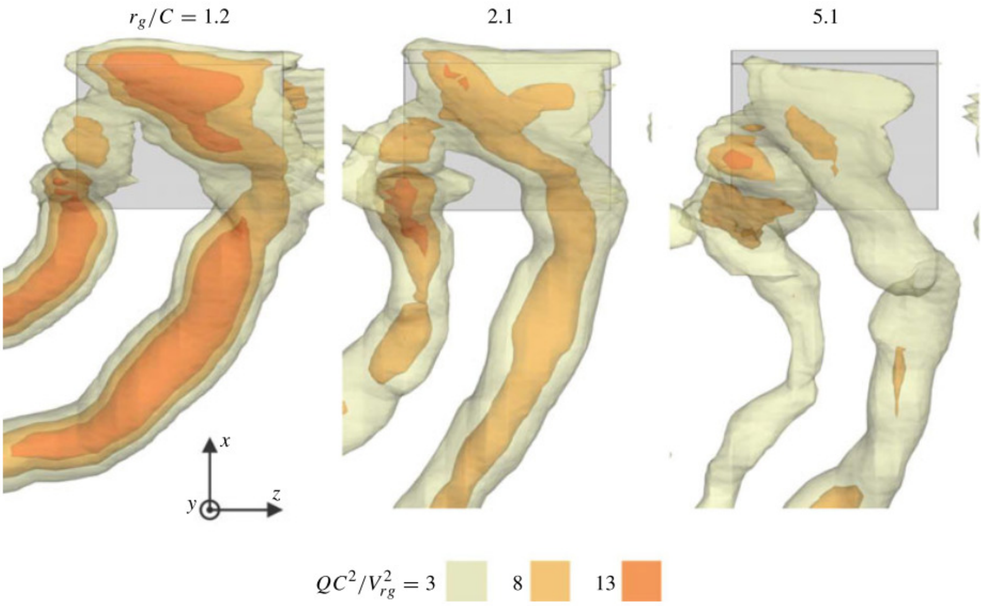

FIGURE 2.14: Wolfinger & Rockwell (2014) observed that the vortex system degraded rapidly with an increase in *Ro* (reproduced with permission).

(2015), and Luo & Sun (2005) observed a negligible effect of Æ on the forces. In these studies, the radius of gyration was also changed with a change in aspect ratio, since the offset and the chord were maintained to be constant. The discrepancies regarding the influence of Æ were explained later by Lee *et al.* (2016) by studying the Æ-*Ro* coupling.

Recently, Phillips *et al.* (2017) have studied the 3D LEV structures on the flapping petiolate wings by extending the root of a rectangular wing from its flapping axis. The petiolation has been calculated as the ratio of the wing-offset to the wing-chord ($P = b_0/c$). They observed that the LEV's size and strength increased with the petiolation. Interestingly, by identifying the footprints of the LEV near the wing surface, they noted that the LEV was larger at midspan and inboard regions for a longer petiolation. However, the predicted LEV circulatory lift values were shown to increase with petiolation in contradiction to the numerical predictions by Lee *et al.* (2016) and Tudball Smith *et al.* (2017), who reported a decrease in the lift with the increasing petiolation. Like the other experimental studies, the study by Phillips *et al.* (2017) also involved a uniform central body with a changing connecting rod length to extend the offset.

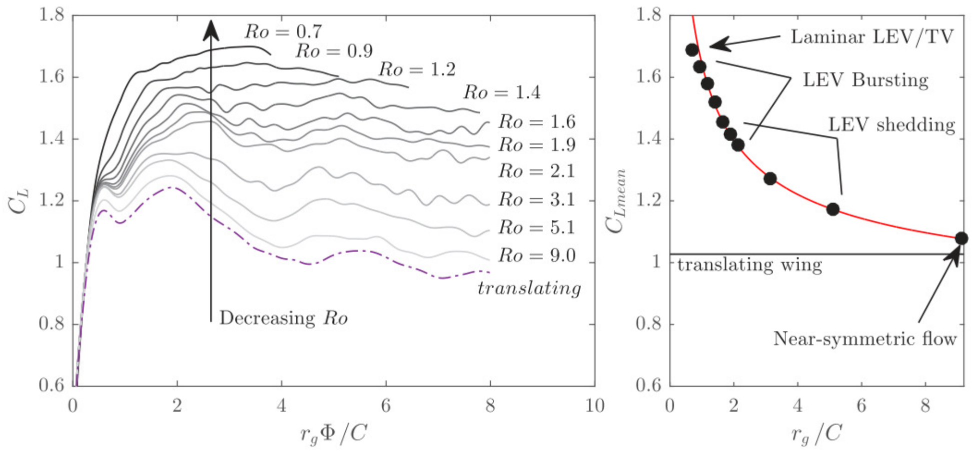

FIGURE 2.15: C_L continuously increases with a decrease in Ro, shown by Tudball Smith *et al.* (2017)[5].

2.4.5 Wing shape and flexibility

The effect of wing shape and camber has been studied by many researchers including Vogel (1967), Luo & Sun (2005), Ansari *et al.* (2008b) and Phillips *et al.* (2010). It is unanimously agreed that camber produces higher lift. Wings of actual insects have corrugated cross-section. The effect of corrugations was studied by Kesel (2000) and Luo & Sun (2005). At low Reynolds numbers and large angle of attack, the corrugations do not make any significant difference in the aerodynamic performance. Hence, while investigating the aerodynamics of flapping insect wings, a flat-plate wing can be used instead of an actual corrugated wing.

Several optimisation models have been used to determine the optimised wing shapes for different flight conditions, such as those by Ghommem *et al.* (2014); Nabawy & Crowther (2016); Throneberry *et al.* (2017). In an extensive numerical study, Ansari *et al.* (2008b) simulated various generic symmetric and asymmetric wing shapes such as a rectangle, triangle, reverse triangle, semi-ellipse, inverted semi-ellipse and half-ellipse. The wing-area was kept constant. Among the symmetric shapes, the reverse triangle was found to have the maximum mean lift; however, among the asymmetric wings, the reverse semi-ellipse was found to have the maximum mean lift. Indeed, in most insects, the wing shapes can be approximated by semi-ellipses (Weis-Fogh, 1973). It can be seen in figure 2.16 that for *Hymenoptera* (sawflies, wasps and bees) and *Lepidoptera*

[5]Reprinted with permission from Tudball Smith *et al.* (2017). Copyright (2017) by the American Physical Society.

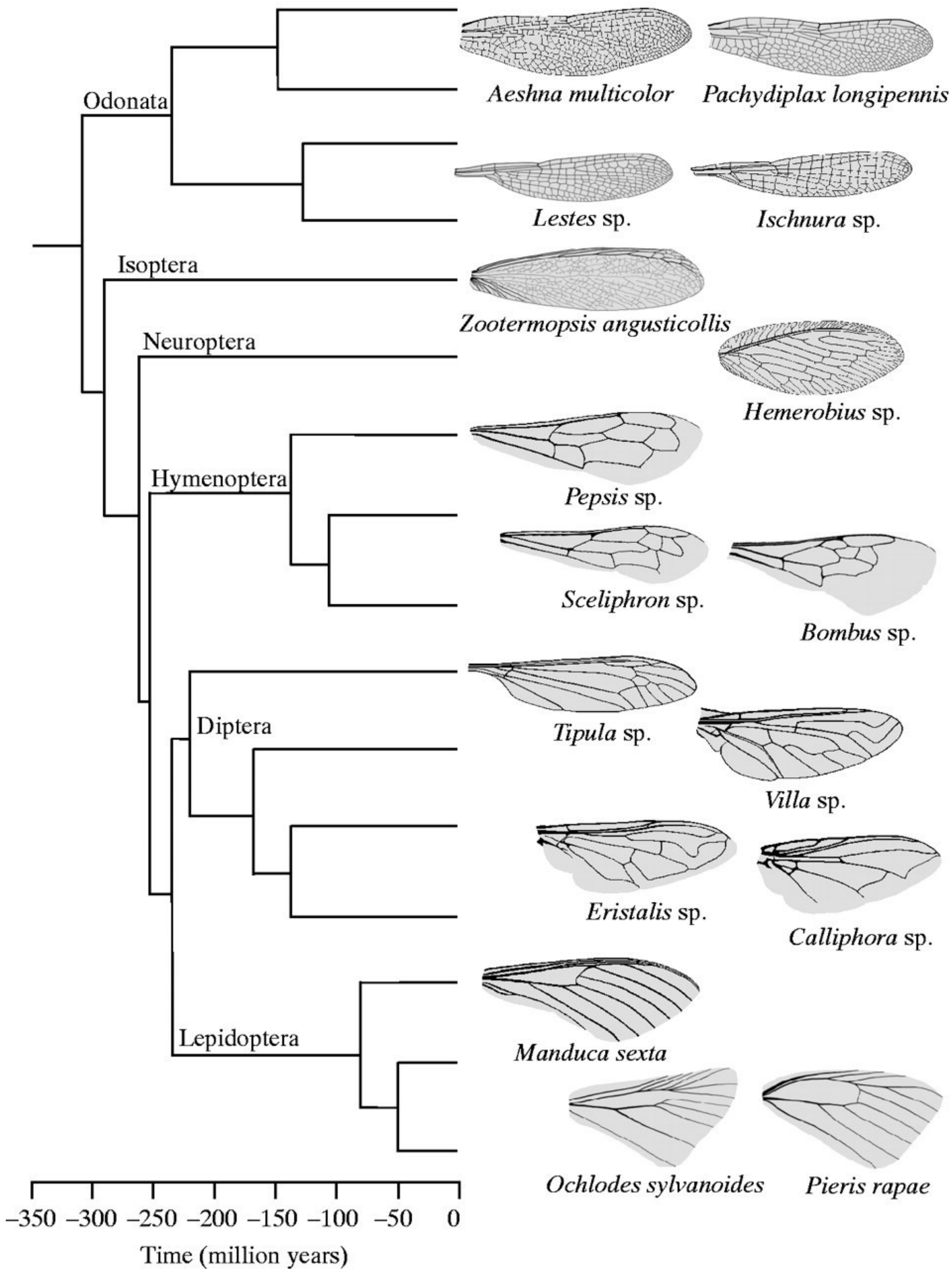

FIGURE 2.16: Wings of various insect species by Combes & Daniel (2003) (figure reproduced with permission).

(butterflies and moths), the wing shapes resemble a reverse triangle whereas for all other species, the wing shapes resemble a semi-ellipse.

In an experimental investigation of flapping wings of four different generic shapes, Phillips *et al.* (2010) observed the general flow structure to be very similar, irrespective of the wing shape. Combes & Daniel (2001) conducted a theoretical study of two dimensional wings of various shapes obtained by redistributing their area. They established that the wings of the higher proportion of the area in the outer part have higher thrust. However, the same wings are less efficient than the wings with a lower proportion of area in the outer part. It should be noted that this two-dimensional model did not involve the effects due to the tip vortices and the spanwise flow, which are commonly observed in the wings of low aspect ratios in nature. Nabawy & Crowther (2016) conducted a theoretical analysis of the hovering wing planforms. They showed that the elliptical wing shape had a minimal profile power whereas the a highly tapered planform similar to a hummingbird had a minimal induced power.

Luo & Sun (2005) have classified the wing shapes based on the radius of the second moment of inertia ($\overline{r}_2$). They found that the variation of the wing shape had a negligible effect on the force coefficients when the velocity at $\overline{r}_2$ was used as the reference velocity. Ellington (1984a) proposed the use of the *Beta distribution* function to represent the wing shapes analytically, which can be written as

$$\hat{c}(\hat{r};\alpha,\beta) = \frac{\hat{r}^{\alpha-1}(1-\hat{r})^{\beta-1}}{\int_0^1 \hat{r}^{\alpha-1}(1-\hat{r})^{\beta-1}d\hat{r}}, \tag{2.11}$$

where, $\hat{c}$ is the local chord-length normalised by the mean chord and $\hat{r}$ is the local spanwise radius normalised by the wing span. The parameters α and β are defined as

$$\begin{aligned} \alpha &= \overline{r}_1 \frac{\overline{r}_1 - \overline{r}_2^2}{\overline{r}_2^2 - \overline{r}_1^2}, \\ \beta &= (\overline{r}_1 - 1)\frac{\overline{r}_1 - \overline{r}_2^2}{\overline{r}_2^2 - \overline{r}_1^2}, \end{aligned} \tag{2.12}$$

where $\overline{r}_1$ is the radius at the centre of mass. Wang *et al.* (2013) adopted this method to analyse various wing planforms. They observed the wings of larger $\overline{r}_1$ values to be more efficient than those with lower $\overline{r}_1$ values.

Shahzad *et al.* (2016) analysed three different wing shapes created by varying the area distribution from more-inward to more-outward proportions, as can be seen in figure 2.17. They classified the wing shapes based on normalised radius of the first moment of inertia ($\overline{r_1}$). For all the investigated Reynolds numbers, the wings with a

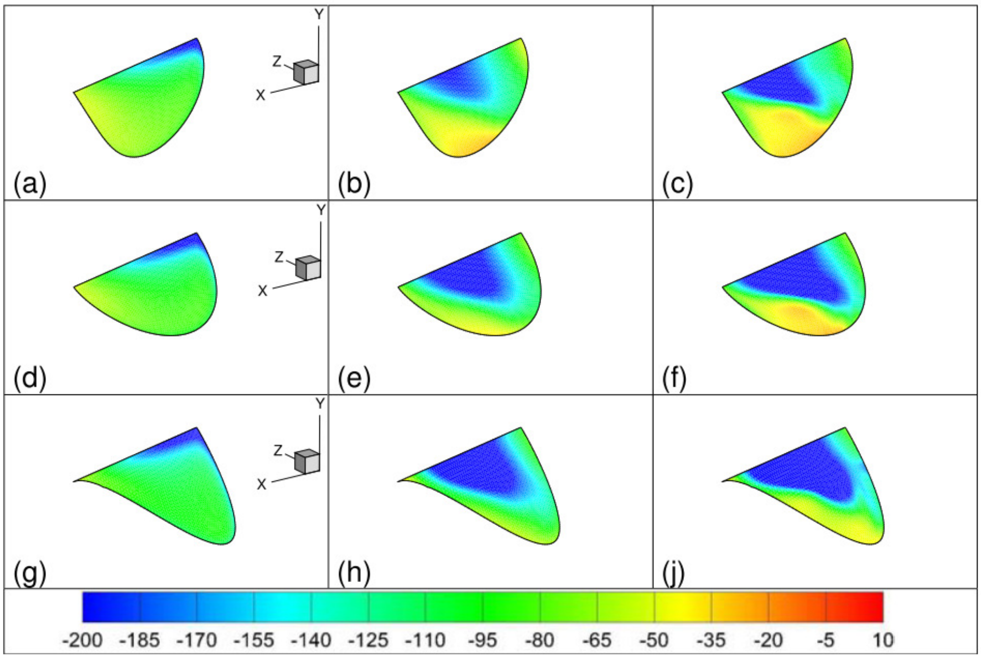

FIGURE 2.17: The normalised surface pressures on the wings of $\overline{r_1} = 0.43$ ((a)–(c)), $\overline{r_1} = 0.53$ ((d)–(f)), and $\overline{r_1} = 0.63$ ((g)–(j)) flapping at $Re = 12$ (left), 400 (centre), and 13500 (right), shown by Shahzad *et al.* (2016)[6].

higher $\overline{r_1}$ outperformed those with a lower $\overline{r_1}$ in terms of the mean lift coefficient ($\overline{C}_L$). However, in terms of the power economy ($\overline{C}_L/\overline{C}_P$), the wings with a lower $\overline{r_1}$ performed better. Their further analysis, by introducing the flexibility to the wings, showed that both the chordwise and the spanwise flexibility helps in increasing the lift in high $\overline{r_1}$ wings (Shahzad *et al.*, 2017). Recently, Chen *et al.* (2018) have pointed out that the shape of the forewing of a hawkmoth matches the formation of the LEV over it.

Wing flexibility also has a significant influence on the wing aerodynamics. Combes & Daniel (2003) have investigated the flexural stiffness of a wide range of insect wings. In insects, wings tend to bend more along the chord as the span-wise bending stiffness is 1- or 2-orders higher than the chord-wise bending stiffness. Nakata and Liu, for the first time, applied a comprehensive 3D flexible wing model in their study of a hawkmoth wing (Nakata & Liu, 2012a,b). Their predictions of spanwise bending agreed well with literature.

Flexibility increases downwash for the same angle of attack and thus increases the aerodynamic forces. The effect of flexibility has been studied mostly using numerical

[6]Reprinted from Shahzad *et al.* (2016), with the permission of AIP Publishing.

simulations by researchers (see Naidu *et al.* (2013), Shyy *et al.* (2008) and Kang & Shyy (2014)); however, it has not been studied experimentally in detail, with very few exceptions such as Zhao *et al.* (2010) and Beals & Jones (2015). Zhao and co-workers found the lift-to-drag ratio insensitive to flexural stiffness for $20^0 < \alpha < 60^0$. However, at higher α, as stiffness was decreased, the L/D ratio increased. Thus, the flexible wing outperformed the rigid wings for high angles of attack.

Nguyen *et al.* (2016) have conducted a comprehensive aerodynamic and structural analysis of a fruit fly wing by simulating the wing veins and membranes with a given stiffness. In addition to the increased lift and reduced drag with a flexible wing, they have shown an increase in the storage of elastic energy of deformation, which is released as kinetic energy during the translation phase. This increased the flapping amplitude compared to the rigid wing.

2.5 Research challenges

It has been agreed by researchers that the leading-edge vortex is responsible for stable lift generation on flapping wings of insects (Ellington (1999), Birch *et al.* (2004) and Lentink & Dickinson (2009b), etc.). The presence of a central holder is unavoidable in experimental models and robotic flyers as it helps to hold and rotate the wing. The effects of the change in the central body size relative to its wings do not appear to have been studied. Experimental studies implicitly assume that the flow over a wing at a given Rossby number is the same with or without a holder. The question that arises while comparing these studies is whether in fact the presence or absence of the holder makes any difference. Since the central holder in experiments also rotates with the wing, it can be hypothesised that the secondary flow near the wing root due to the rotating holder may interfere with the LEV formed at the root. Beyond a certain size of the holder, the increased secondary flow may well influence the forces on the wing.

The study of the wing aspect ratio on the wing performance has gained a significant interest due to the contradictory results presented by researchers in the past. Lee *et al.* (2016) attempted to conclude this debate by discussing various past studies and the *AR-Ro* coupling of their respective geometries that converged to a common conclusion in terms of a contour map of the lift coefficient in the plane of $\mathcal{R}$ and Ro. It can be inferred from their trend that the lift coefficient can be maximised by increasing $\mathcal{R}$ for any given Ro. These results were obtained at a low Re, at which only low-$\mathcal{R}$ wings are observed in nature. Therefore, this and past studies do not provide a satisfactory explanation of why certain aspect-ratio wings are observed only at certain Reynolds numbers in nature. Moreover, the effects of AR and Re are also observed to be coupled (Harbig *et al.*, 2013), which might have added an additional level of controversy in the predicted trends of the lift coefficients. Hence, a comprehensive study of the effects of AR Ro, and Re is important to determine their combined effects.

Insect wings have additional features such as wing venation and varying thickness, which may be functional in providing the structural strength and allowing the passive bending as a response to the aerodynamic forces. However, the MAV wings can generally be simplistic in design, made from a flat plate without any venation. For such wings, it would be interesting to study the optimum shape that can have a maximised lift. Most optimisation studies seem to have used the force predictions based on the quasi-steady models. However, an approach, purely based on the aerodynamic pressure distribution on the wing, can explain the reasons behind the increased aerodynamic forces with an optimised shape. Such a study does not seem to have been undertaken in the past.

The velocity profile of the wing motion is another parameter that may have an effect on the wing performance. The LEV has been observed to be stable on account of centripetal and Coriolis accelerations of the flow over the rotating wing (Lentink & Dickinson, 2009b). A change in the velocity profile can result in a change in a mean lift generation throughout the stroke. Research on motion profiles until the last decade concentrated mostly on timing and phase of rotation with respect to translation. Few numerical and optimisation studies indicate that the insects' motion profiles are optimised for minimum power. However, many studies on the flapping wings continue to use either the harmonic or the triangular waveforms for the wing motion. Hence, it is important to investigate how the aerodynamic forces and power change with the various motion waveforms and to provide experimental evidence of an optimum flapping motion waveform.

Chapter 3

Methods

The present study uses experimental and computational methods to investigate the rotating and flapping wing aerodynamics of insect wings. This chapter presents a detailed description of both the experimental and the computational techniques.

The experiments were conducted in a fluid tank in the Fluids Laboratory for Aeronautical and Industrial Research (*FLAIR*) at Monash University. Two experimental rigs were developed for rotating and flapping a wing. Techniques such as particle image velocimetry (PIV) and force measurement were used to study the flow over a rotating and flapping insect wing. A scanning PIV technique was developed to obtain the flow measurements of the three-dimensional leading-edge vortex (LEV) by rapid acquisition of images of different spanwise planes. The experimental rigs and techniques were validated prior to conducting the experiments from which results were obtained.

The computational analysis was performed on a rotating wing. The computational fluid dynamics (CFD) models were adopted from those used by Harbig *et al.* (2013) using the commercial code ANSYS CFX version 17.2. The governing equations were solved in a rotating frame of reference. The models were modified as per the geometries being investigated. In this chapter, the details of the experimental rigs, techniques, and their validation are presented in § 3.1. The governing equations for the numerical analysis, details of the rotating-wing model, and its validation are explained in § 3.2.

3.1 Experimental system and techniques

The experiments on a rotating and flapping wing were conducted in a quiescent flow in a tank. Both rigid and flexible wings were fabricated and the wing geometry was varied, mainly by changing its aspect ratios. The details of the wing geometry in experiments are described in the following section. The details of the experimental rigs and the measurement techniques are described later.

3.1.1 Wing geometry

The wing geometry was based on a generic fruit fly (*Drosophila melanogaster*) wing. This representative wing-shape has been extensively studied by many researchers both numerically and experimentally (Liu & Aono, 2009; Birch *et al.*, 2004; Vogel, 1966; Zanker & Götz, 1990; Hawkes & Lentink, 2016). The basic wing was scaled from the actual fruit fly wing planform (Zanker & Götz, 1990), so as to have a wing-span of 120 mm and an aspect ratio of 2.91. The wing span, b, is measured from the wing root to the wing tip, whereas the chord, c, is measured from the leading edge to the trailing edge. The wing aspect ratio is defined as the ratio of the wing span to the mean chord ($\mathcal{R} = b/c_m$).

The wings of different aspect ratios were designed by stretching or compressing the original wing shape in the chordwise direction. The thickness to chord ratio of the wings was maintained to be less than 5%. The wing was attached to a cylindrical central body to hold and rotate the wing, as shown in figure 3.1. Due to this, the wing root was offset from the rotation axis by an amount b_0 such that the total span is $R = b + b_0$. The wing-root offset, b_0, was normalised by b to give the offset ratio, $\hat{b}_0$. Two types of wings were fabricated, rigid and flexible, as shown in figure 3.1.

3.1.1.1 Rigid wings

Most of the experiments were performed with the rigid wings. The wings were fabricated using a CNC machine from stainless steel (SS) and acrylic sheets of thickness up to 2 mm. The material was chosen to avoid corrosion when used in water. The SS wings were painted with a flat black spray paint to reduce the surface-reflections of the laser during the PIV experiments. Two independent rigs were developed to provide the rotational and flapping motion to the wing. The motion was controlled with the help of servo motors driven by computer-controlled drives. The two rigs are described in sections 3.1.2 and 3.1.3.

3.1.1.2 Flexible wings

We attempted to validate the possibility of studying the effects of wing flexibility, necessitating an investigation into how to fabricate flexible wings. In this section, some details of the flexible wing geometry are presented, which may be helpful for a future

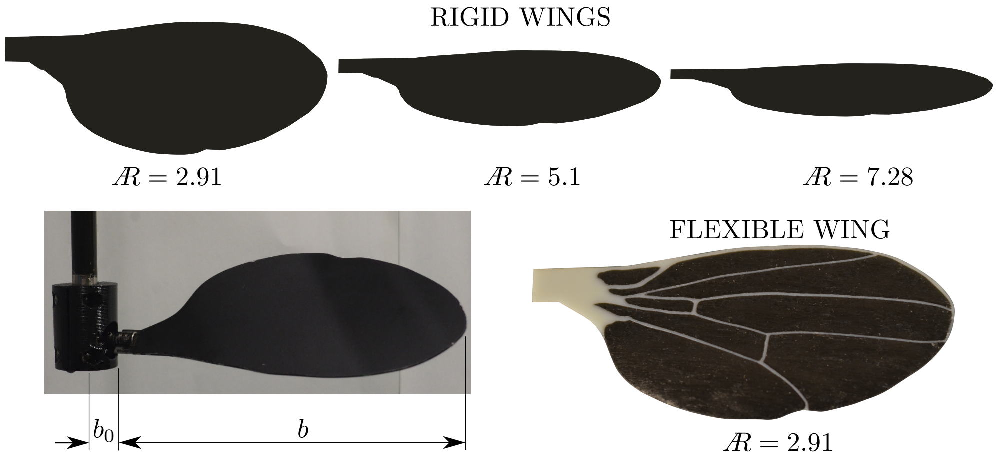

FIGURE 3.1: Rigid wings of different aspect ratios (top) were fabricated from stainless steel and a flexible wing (bottom-right) was 3-D printed using a white plastic frame and black rubber planform. The wing was held and rotated using a cylindrical central body attached to the bottom of a rotating shaft. During the experiments, the wing was inverted to point the leading edge downward so as to allow the laser sheet to illuminate the leading edge vortex from the bottom.

study on flexible wings. In this preliminary study, three different flexible wings were fabricated to test various flexural rigidities. The three wings are as follows.

1. FlexWing1: 3D printed wing - (1-mm thick VeroWhitePlus plastic frame and TangoBlackPlus rubber wing planform)

2. FlexWing2: 1-mm thick stainless steel frame and 100-μm polythene sheet wing planform

3. FlexWing3: 0.75-mm PTFE frame and 100-μm polythene sheet wing planform

It should be noted that the wing frame in all these wings was based on the wing-venation pattern of fruit fly wings. FlexWing1 was found to warp significantly with small changes in the ambient temperature. Thus, FlexWing2 and FlexWing3 were chosen for further validation. We first identified the flexural rigidity of the two wings by following the method described by Combes & Daniel (2003). The wing was supported at its root and deflected by pushing against a pointer. The force exerted on the pointer (F) was measured by the ATI Nano17 IP68 force transducer. The applied deflection and the corresponding force were noted to compute the value of the flexural rigidity as

$$EI = \frac{FL^3}{3d}, \tag{3.1}$$

Wing	Spanwise EI (N-m^2)	Chordwise EI (N-m^2)
FlexWing2	1.11e-2	7.28e-4
FlexWing3	2.04e-4	4.64e-5

Table 3.1: Flexural rigidity of the wings for spanwise and chordwise bending.

where L is the distance of the pointer from the wing root and d is the deflection of the wing. The EI values corresponding to the spanwise and chordwise bending can be seen in table 3.1.

Here, FlexWing3 has a flexural rigidity in the range of EI values for real insect wings given by Combes & Daniel (2003). There were some challenges while performing the PIV measurements on the rotating FlexWing3 due to its spanwise bending. The bending of the wing tip blocked the view of the LEV. Moreover, the chordwise and spanwise bending of the wing could be affected by the wing venation pattern. It could also be affected by the wing thickness, which is not uniform in real insects. Therefore, these factors would require experimentation over a very large parameter space; this could form the basis of a separate extensive study on flexible wings. However, considering the focus of the present study, which included the investigation of the parameters such as the wing aspect ratio, wing-root offset and the wing motion profile, only the rigid wings were used to avoid the further complications arising from wing flexibility.

3.1.2 Rotational motion

As described in chapter 2, the flow structure obtained over a flapping wing during its mid-stroke can be approximated to the flow structure obtained over a rotating wing with a constant angular velocity at the same Reynolds number. Therefore, the study of the flow structure over the wing in pure rotation can provide useful insights into the flight stability of insects, which is mainly governed by the stable LEV during most of its flapping stroke. The experimental rig and the wing kinematics for the rotational motion are described below.

3.1.2.1 Rotation rig

For the experiments on a rotating wing, the wing was held using a central holder attached to the central driving shaft, as shown in figure 3.2. The mounting was such that the wing root was offset from the central axis by an amount equivalent to the radius of the wing holder (b_0). The angle made by the wing plane with the horizontal

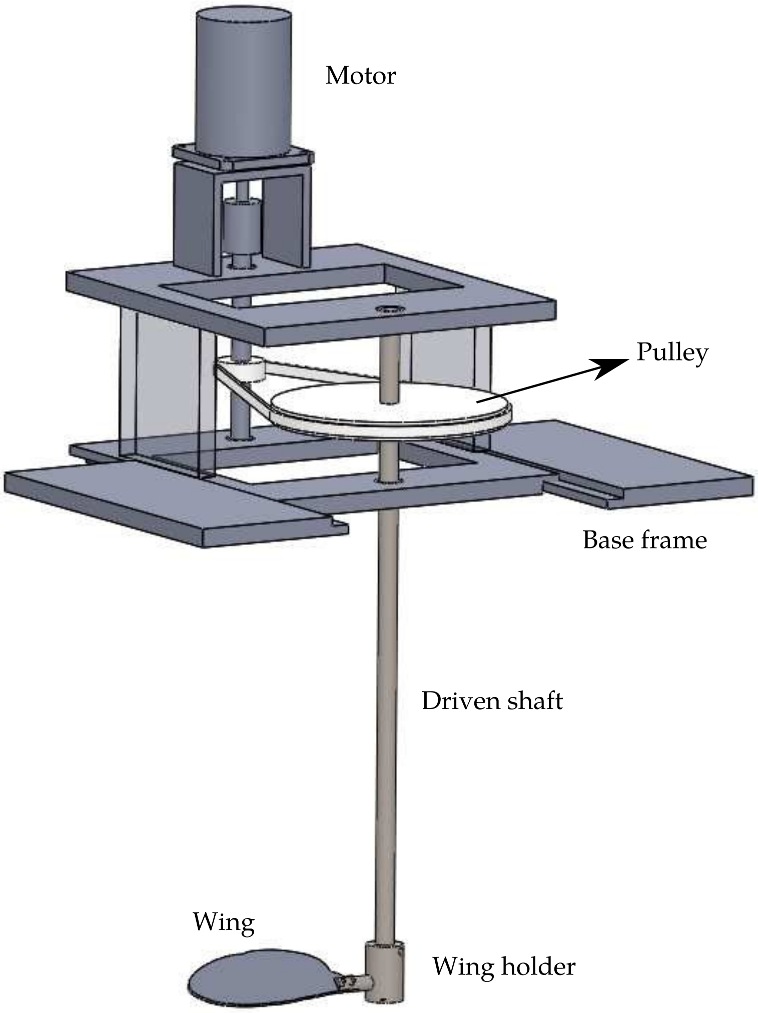

FIGURE 3.2: The rotation rig consists of a belt-and-pulley mechanism in order to reduce the motor speed and increase the applied torque.

is known as the angle of attack (α). In experiments, the leading edge was pointing downwards, as shown in the schematic in figure 4.1. This allowed the laser plane to be projected from bottom of the tank, to better illuminate the LEV.

The rotational speed of the wing-shaft was reduced by a belt-and-pulley system by the ratio 4.5:1. The rotational motion was driven by a brush-less DC motor (model: EC-max 30, Maxon Motor) equipped with an encoder (model: ENC24 2RMHF, Maxon Motor) with 5000 counts per turn, and a gear box (model: Koaxdrive KD 32, Maxon Motor) to further reduce the rotational speed by 63:1. This reduction also helped in providing sufficient torque to drive the model. The rig was mounted in such a way that the wing shaft was positioned at the centre of the tank.

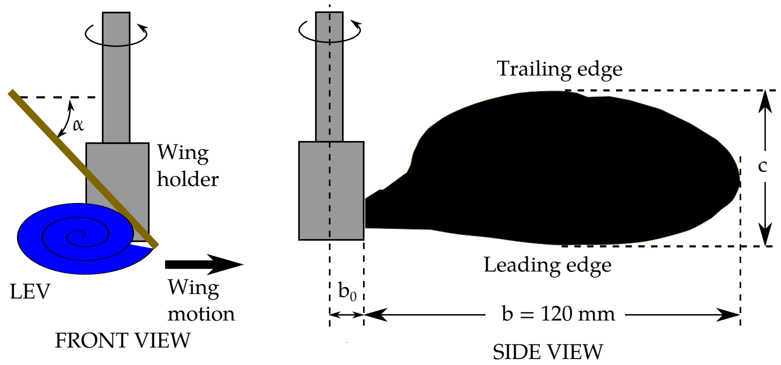

FIGURE 3.3: The wing is mounted on a holder that causes it to offset from the axis of rotation by an amount b_0.

3.1.2.2 Wing kinematics

During the experiments, a simplified motion was prescribed to the wing to obtain the LEV structure that is formed during the mid-stroke of a typical flapping cycle of an insect. This required the wing to be held at a constant angle to the horizontal ($\alpha = 45°$) and rotated with a constant angular velocity (Ω) without requiring the wing-flip and stroke-reversal. The wing was initially uniformly accelerated over a time of $\Delta t = 0.084T$, where T is the total time for one complete rotation. This acceleration period was chosen as the impulsively started wing has been shown to be comparable to the beginning of the downstroke of a flapping cycle (Poelma *et al.*, 2006), with the acceleration period typically ranging between 6 and 10% (Birch *et al.*, 2004; Lentink & Dickinson, 2009b). After this acceleration, the wing reached a constant angular velocity corresponding to the chosen span-based Reynolds number given by

$$Re_b = \frac{U_g b}{\nu}. \tag{3.2}$$

Here, U_g is the velocity at the radius of gyration ($U_g = R_g\Omega$), R_g is the radius of gyration of the wing, b is the wing span, and ν is the kinematic viscosity of water. The wing was decelerated over the last $0.084T$ and stopped.

The flow field was captured using a scanning PIV technique at the fixed phase angle of $\phi = 270°$. This phase angle was chosen to allow the flow to reach a near asymptotic (steady) state without running into its own wake. In practice, as demonstrated in § 4.3, the flow pattern does not vary significantly between 90° and 315° for moderate Reynolds numbers. The flow in the tank was disturbed by the wing rotation during each experiment. Hence, it was allowed to dissipate the residual vorticity for 10 minutes before starting the next recording. This was found to be a near-optimal waiting time. A longer time could result in thermal convection driven by a small temperature difference between the fluid and the surroundings.

3.1.3 Flapping motion

The study of various flapping motion profiles required a flapping motion rig. The rig was designed to provide a simplified flapping motion to the wing, with two degrees of freedom. The wing could move along the sweep or phase angle (ϕ) and the angle of attack (α). The pitch angle is defined as $\psi = 90° - \alpha$. In this simplified motion, the pitch axis always remained in a plane, avoiding the out-of-plane flapping of the wing. The flapping motion rig and the motion profiles are described below.

3.1.3.1 Flapping motion rig

The flapping motion rig, as shown in figure 3.4, was fabricated to perform experiments on the flapping wing. The flapping motion of the wing was comprised of the motion about two axes, the rotation axis and the pitch axis. Two Maxon EC-max30 servo motors were employed to provide the motion about these two axes. The rotation axis was aligned with the main central shaft driven by Motor-1 at the top. The rotation about this axis caused the wing to move in a horizontal plane, by changing its phase angle (ϕ). The pitch axis was aligned with the wing span at the wing root. The rotation about this axis made the wing to change its pitch angle (ψ).

The pitch motion was transferred to the wing from Motor-2 at the top, using a timing belt and timing pulleys. The centrally mounted shaft was chosen to be hollow to allow the transfer of the motion through the belt-and-pulley mechanism. A timing pulley was mounted on the motor shaft that transferred the motion to the timing belt placed inside the hollow shaft. The belt drove another pulley situated at the bottom of the shaft covered with a cylindrical wing holder. The pulley was mounted on a miniature shaft of diameter 2-mm that was held in its place by two miniature ball bearings fitted inside the holder. Finally, the connecting rod that held the wing was attached to the miniature shaft. It should be noted that as Motor-1 rotated the central shaft, Motor-2 also revolved around the central axis along with it. The flapping motion required the sweep angle to be varied by less than 180° peak-to-peak.

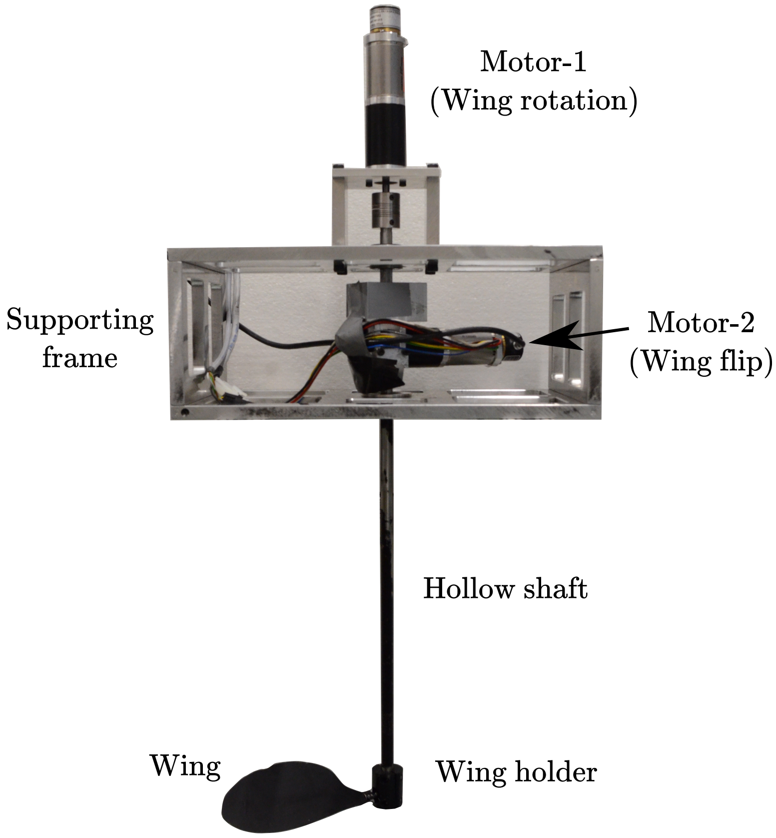

FIGURE 3.4: The flapping motion rig.

3.1.3.2 Flapping wing kinematics

The flapping wing kinematics involved the 2-DOF system with varying flapping profiles, adopted from Berman & Wang (2007). The time-variation of the sweep angle (ϕ) is defined as

$$\phi(t) = \frac{|\phi|}{\sin^{-1} K} \sin^{-1}[K \sin(2\pi f t)], \tag{3.3}$$

where $|\phi|$ is the magnitude of oscillations in sweep, f is the frequency of oscillations, and K is the sweep profile parameter varying in the limit $0 \leq K \leq 1$. A sinusoidal profile is defined by the limit $K \rightarrow 0$, whereas a triangular profile is defined by the limit $K \rightarrow 1$. In short, the time taken for the wing reversal can be varied by varying K. Similarly, the time-variation of the pitch angle (ψ) is defined by a periodic hyperbolic function as

$$\psi(t) = \frac{|\psi|}{\tanh C_\psi} \tanh[C_\psi \sin(2\pi f t + \Phi)], \tag{3.4}$$

where $|\psi|$ is the magnitude of pitch oscillations, Φ is the phase difference between the sweep and the pitch oscillations (which was maintained to be $\pi/4$), and C_ψ is the pitch

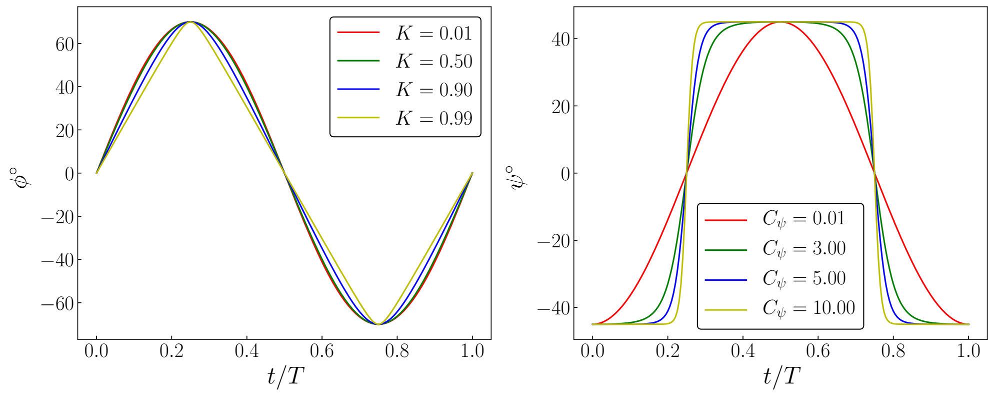

FIGURE 3.5: Flapping profiles for the sweep angle (ϕ) and the pitch angle (ψ), with varying profile parameters.

Tank	Length (mm)	Width (mm)	Height (mm)
WT1	500	500	600
WT2	1000	1000	800

TABLE 3.2: Sizes of two tanks of quiescent fluid used for experiments.

profile parameter. The profile is sinusoidal as $C_\psi \to 0$, and it is a step function when $C_\psi \to \infty$. The variation in the profiles can be seen in figure 3.5.

3.1.4 Fluid tank

The experiments were conducted in quiescent, fluid-filled square cross-section tanks. Two different tank sizes were used for the experiments, as tabulated in table 3.2.

3.1.4.1 Tank size validation

It is important to validate the tank size, since the proximity of its walls can affect the flow structures over a wing. During the wing rotation, the flow structures near the wing are shed in the wake and can be transported towards the tank walls depending on their acceleration. The validity of the results for the given size of the tank was checked by rotating the wing and observing the evolution of the flow structures in a horizontal plane, as shown in the schematic in figure 3.6. The flow was seeded with PIV particles and illuminated by a laser sheet in a horizontal plane close to the mid-chord. The flow field was recorded using Dimax PCO high speed camera. The images were processed to give the velocity and vorticity measurements in the illuminated plane.

For this validation study, rectangular wings of three different aspect ratios were

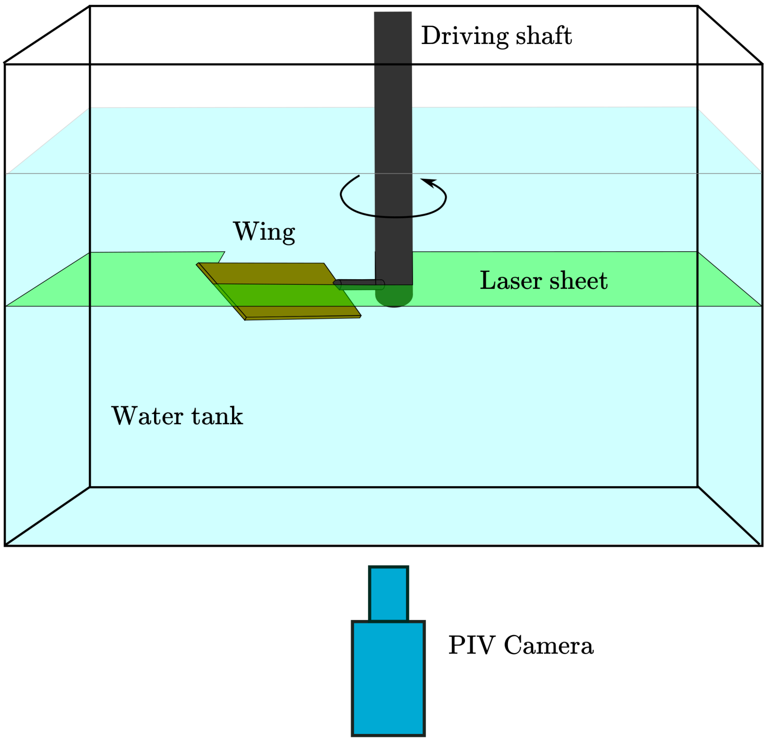

FIGURE 3.6: Schematic of the PIV experiments setup used for validating the tank size

chosen such that they had a constant chord and different spans. The wing with a higher aspect ratio sweeps a larger area in the tank. The wings were rotated with a constant velocity at $Re = 1500$. PIV images were obtained at different phases of the rotation of each wing. The normalised vorticity plots at different phases for the wings are shown in figure 3.7. Vorticity contours plotted at different phases of rotation show that the vortices from the tip are mostly left in a curved wake pattern that diffuses with time. In all the cases, the vorticity near the tank wall remains low, indicating no significant impact due to the wall-proximity.

3.1.4.2 Tank settling time

As the wing rotates inside the water tank, the quiescent state of water is disturbed. The vortices formed at the wing edges are shed in a circular wake which diffuses with time. However, the wing may encounter the residual vorticity left in the wake by the wing in a previous rotation cycle, which may interfere with the flow over the wing. Hence, the rotating wing experiments were conducted in such a way that the data were recorded during one rotation of the wing and the rotation was then stopped to allow

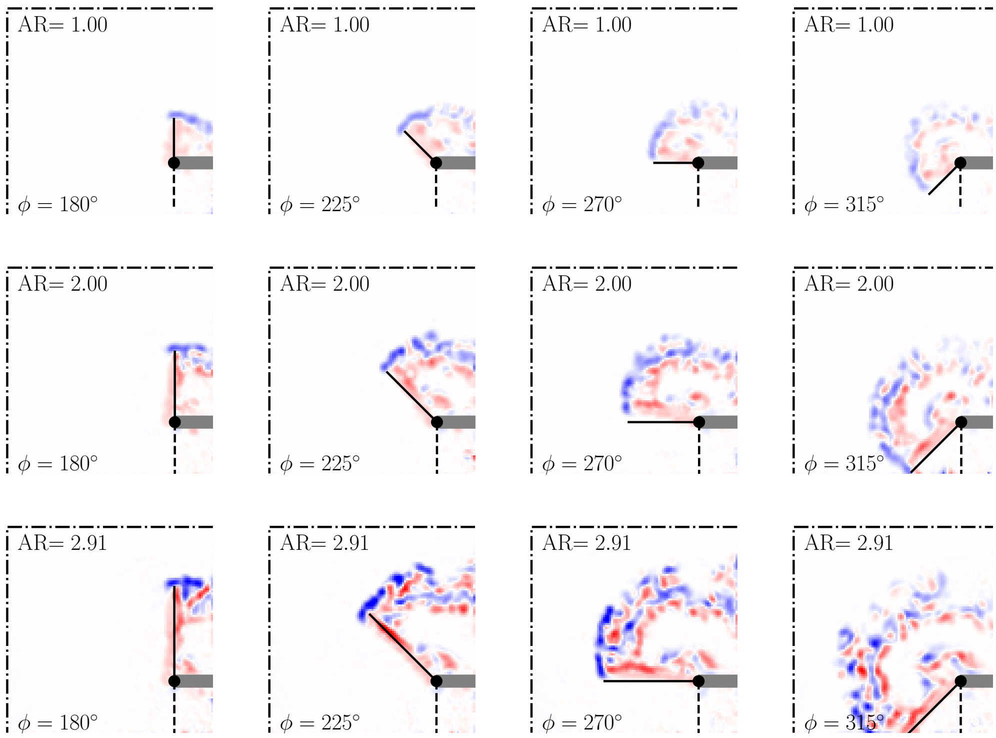

FIGURE 3.7: Normalised vorticity ($\omega_y^* = \omega_y U_g/c$) contours are plotted at different phases of rotation for wings of $\mathcal{R} = 1, 2$, and 2.91. Here, the counter-clockwise vorticity is considered to be positive. The dashed line represents the starting position of the rotating wing. The dash-dot line represents the tank wall. The grey colour shows the shadow cast by the central holder of the wing. The vorticity near the wall even for the largest wing span is low.

the flow to settle. The duration between two consecutive rotations of the wing is called as the tank settling time t_s.

The tank settling time was found by recording the time-variation of the mean velocities in the vertical plane passing through the wing-tip, where the instantaneous velocities were maximum. The wing of $\mathcal{R} = 2.91$ was initially in the tank WT1 (refer table 3.2) rotated through 360° and stopped. The PIV images were recorded right from the time when the wing rotation was stopped till the next 20 minutes at the intervals of 30 seconds. The time variations of the mean horizontal and vertical velocities (u and v), and the mean vorticity (ω_z) are plotted in figure 3.8. Two sets of data were recorded, for a low and a high Reynolds number rotation ($Re = 120, 1500$).

After the wing was stopped, the velocities were observed to fluctuate, but decrease drastically in the first 5 minutes. Later, the velocities decrease with a lower rate, reaching values less than 5% of the reference velocity (U_g) at times beyond 10 minutes.

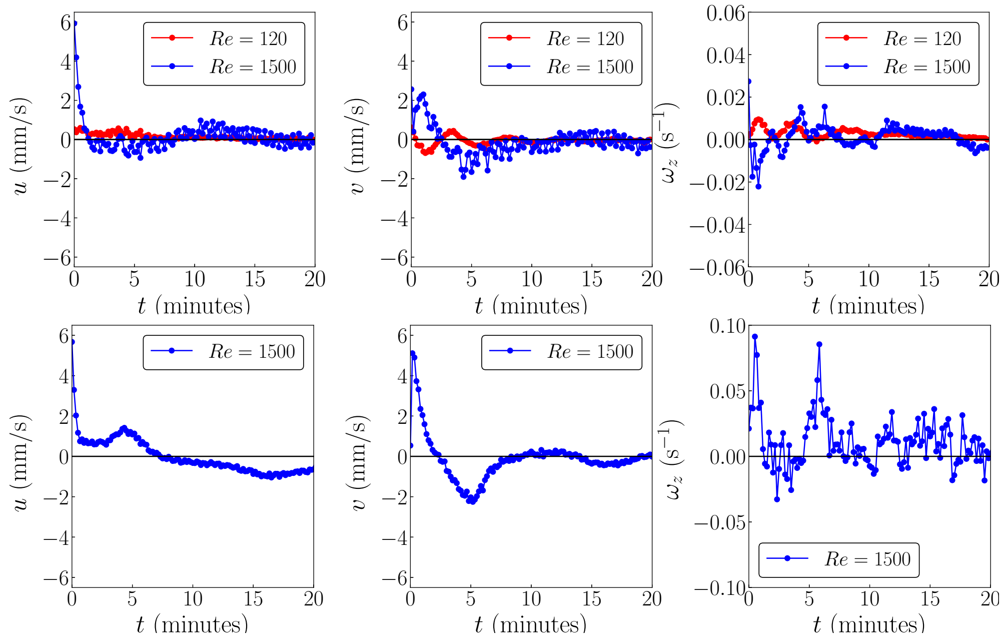

FIGURE 3.8: The horizontal velocity (u), vertical velocity (v), and spanwise vorticity (ω_z) reduce with time after the wing rotation was stopped at $t = 0$ minutes, both for the small and the big tank. The top row shows the velocity and vorticity records for the small tank (WT1) and the bottom row shows the velocity and vorticity records for the big tank (WT2).

The vorticity also initially fluctuated with time and then decreased to a low value ($\omega_z < 0.01$) after 10 minutes. Hence, the tank settling time was determined to be 10 minutes for all experiments in the range of Reynolds numbers $120 \leq Re \leq 1500$.

This procedure was repeated with the bigger tank (WT2) with the wing rotating at $Re = 1500$. It can be observed from figure 3.8 that the flow in the smaller tank settled relatively earlier than that in the big tank. However, even with WT2, the velocities and vorticity decreased to low values 10 minutes after the wing rotation was stopped. Moreover, in this case, the horizontal velocity began changing its direction after 15 minutes. It increased in magnitude in the negative direction, indicating a possible large scale convection flow in the large fluid volume. The rotating wing experiment with $Re = 350$ was repeated using different time intervals between the two experiments in order to observe the impact of the tank flow velocities present at these time intervals.

A comparison of the flow structure was made with the reference case obtained from the experiment in the small tank (WT1) by comparing the vorticity contours at different spanwise locations, shown in figure 3.9. The flow obtained for the cases using the settling time of 10 minutes and 12 minutes matched well with the reference case. In

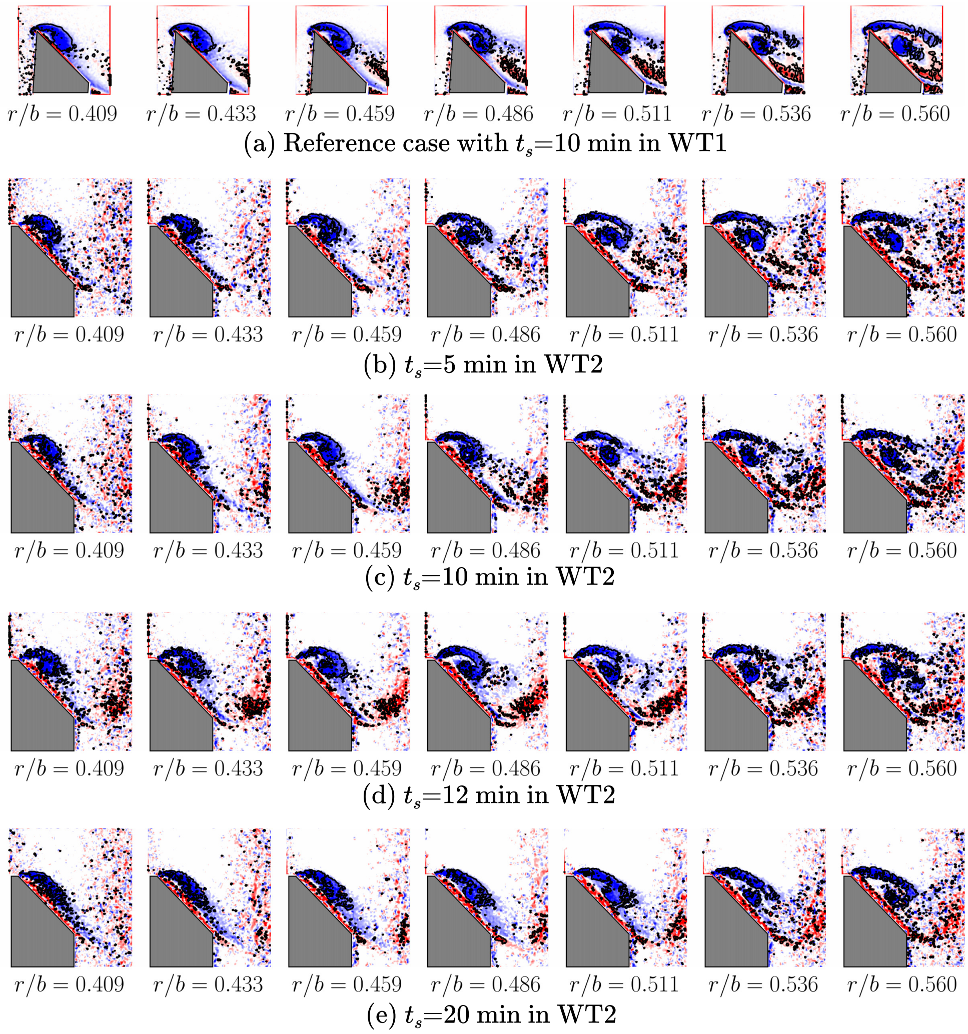

(a) Reference case with t_s=10 min in WT1

(b) t_s=5 min in WT2

(c) t_s=10 min in WT2

(d) t_s=12 min in WT2

(e) t_s=20 min in WT2

FIGURE 3.9: The normalised vorticity contours are plotted at different spanwise locations and compared for the cases by varying the settling time (t_s). The LEV structure and its split position is observed to change with t_s.

other cases, the background velocity interfered with the LEV structure as can be seen in the figure. Hence, the settling time between the two wing rotations was maintained at 10 minutes.

3.1.5 Scanning PIV technique

The LEV was observed to have a 3D structure. The studies, such as those by Cheng *et al.* (2013) and Jones *et al.* (2016), have employed 3D PIV or stereo PIV techniques to capture the 3D structure. The LEV-vorticity is aligned predominantly in the spanwise direction. Hence, the structure of the LEV could be characterised by obtaining the

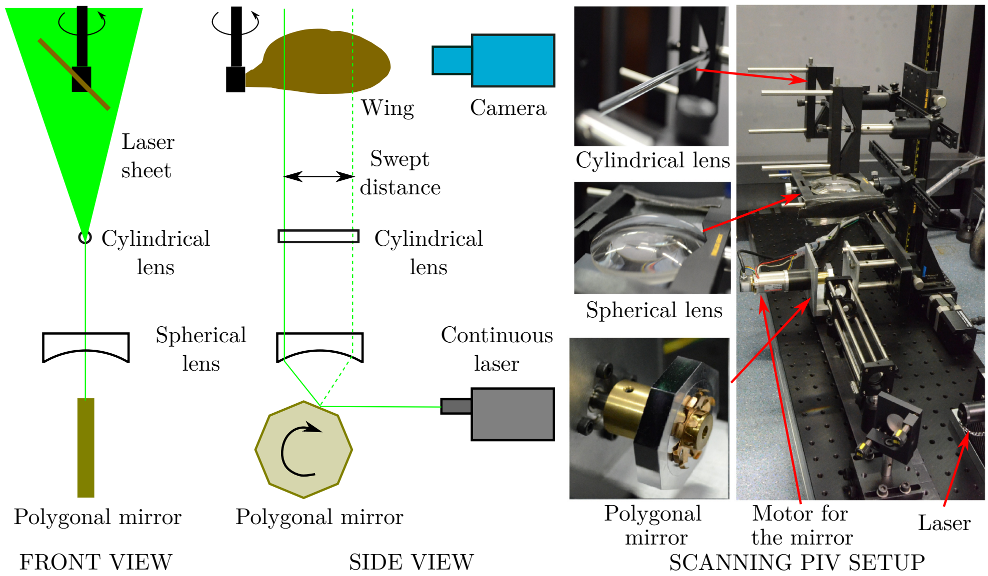

FIGURE 3.10: Schematic of the scanning PIV system shown in the front and side views. As the polygonal mirror rotates, the laser sheet scans the distance in spanwise direction.

spanwise vorticity field in cross-sectional planes at multiple spanwise locations of the wing. This would require the laser apparatus, or at least the laser sheet, to be shifted to different locations for every recording. Considering an idle time of 10 minutes between two recordings, obtaining PIV images at different spanwise locations with standard PIV could be a time-consuming process.

Researchers in the past have developed scanning PIV systems for fast recording of multiple planes within a volume. For instance, Brücker (1995), David *et al.* (2012), and Lawson & Dawson (2014) used an oscillating mirror, whereas Green *et al.* (2011) and Albagnac *et al.* (2014) used a mirror mounted on a high-speed linear traverse to scan the volume. David *et al.* (2012) performed scanning PIV measurements for an airfoil of a finite aspect ratio flapping in two dimensions (linear translation and pitch).

In the present work, a scanning PIV system was developed with a rotating mirror. It allowed multiple images to be taken at high speed during a rotation of the wing. It also provided a scanning resolution of about $\Delta(r/b) = 0.025$ in the spanwise shift. A schematic of this scanning PIV setup is shown in figure 3.10. A laser beam from a continuous laser (model: MLL-N-532nm-5W, CNI) is reflected by a polygonal (octagonal) mirror. The reflected beam then passes through a plano-concave spherical lens. The spherical lens is aligned such that the beam is refracted only in the vertical

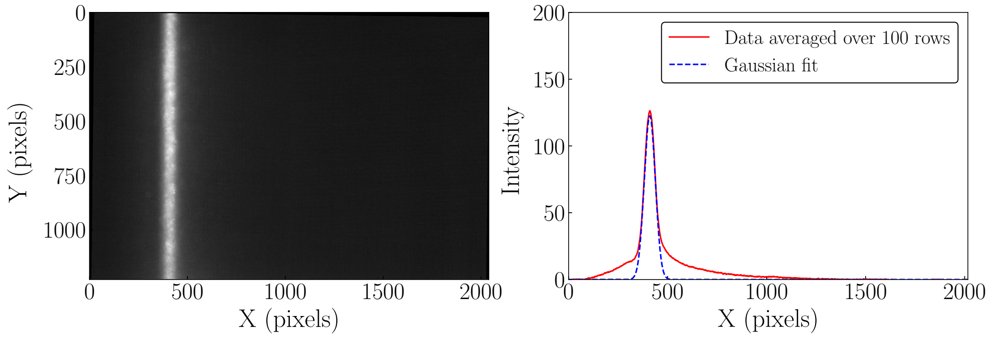

FIGURE 3.11: Measurement of the laser sheet thickness. The laser sheet appears as a line from the side view. The intensity is averaged over the central 100 rows. The width is considered to be the full width at half maximum (FWHM) of the Gaussian.

direction. This is followed by a cylindrical lens that forms a laser sheet. The laser sheet illuminates the PIV particles (model: S-HGS-10) around the wing in the fluid.

The rotation of the polygonal mirror was achieved using a Maxon EC-max 30 servo motor and a Maxpos 50/5 position controller. As the polygonal mirror rotated, the laser sheet shifted its position along the wing span. PIV images were obtained at different spanwise positions using a PCO Dimax S4 camera sampling at a rate of 1000 frames per second (FPS). An exposure of 0.75 ms was set so as to limit the thickness of the shifting laser to within 3 mm. In the side view, the laser sheet appeared as a thick line. Images were also captured from the side to measure the shifting location and width of the laser sheet.

Figure 3.11 shows a typical image of the laser sheet captured from the side view. The intensity of the central 100 rows is averaged to quantify the intensity variation shown in the figure. The laser sheet width is calculated by measuring the full width at half maximum (FWHM) of the Gaussian fit to the intensity curve. The location of the laser sheet is identified by the location of the peak of the Gaussian fit.

For a single set of PIV measurements, the polygonal mirror was rotated through 720°. The mirror had 8 reflecting faces. Each mirror face could reflect the beam for 45° rotation of the polygon. The camera was triggered only for the 15° rotation of each face when the laser plane fell in the volume of interest. During the remaining 30°, the laser plane was shifted out of the volume of interest. Overall, 16 such scanning sets were obtained during the measurements, with each set containing 26 images. Only the central four scanning sets were processed to obtain the three sets PIV image pairs

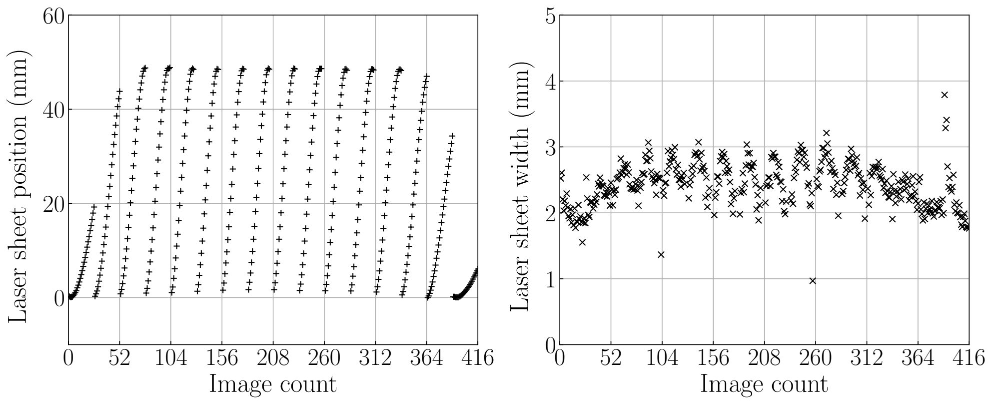

FIGURE 3.12: Measurements of the laser-plane location in motion. The scanning motion of the laser plane is tracked from the side view. The position of the laser plane is tracked based on the location of the Gaussian peak. The system is capable of scanning a distance of 50 mm across the span consistently, except for the first and last 3 cycles, where the rotating mirror is accelerating or decelerating. The laser sheet width is consistently between 2 and 3 mm.

used to reconstruct the velocity field. The scanning PIV was performed in the range, $600 < Re_b < 1500$. During the recording time of the central four sets, in the worst case ($Re_b = 1500$), the wing rotated through 269.45°–270.55°. The LEV structure remained unchanged for a wide range of phase angles, as described in the results. For higher Reynolds numbers ($Re_b > 1500$), fixed-plane PIV was performed.

To calibrate the laser plane position with respect to the mirror rotation, images were obtained from the side view. Figure 3.12 shows the results of the laser plane position and the corresponding laser sheet width varying across the imaging sequence. From the figure, it can be seen that the laser sheet is able to consistently scan through a distance of 50 mm except for the first and last 3 scans. This is because when the mirror accelerates or decelerates, the distance travelled by the laser sheet in the chosen interval of time is less than that at the constant rotation speed programmed. The laser sheet width observed is between 2 and 3 mm in, approximately, 90% of the images. The laser plane position in a particular scan can be identified to an accuracy of 1 mm by the index of the image in the scan.

For PIV measurements, the camera was focussed at the centre of the scanned distance. The aperture opening was set to $f/8$ to provide a greater depth-of-field. Images of the same index from two consecutive scans were paired. Cross correlation was performed between the pairs using in-house codes originally developed by Fouras *et al.*

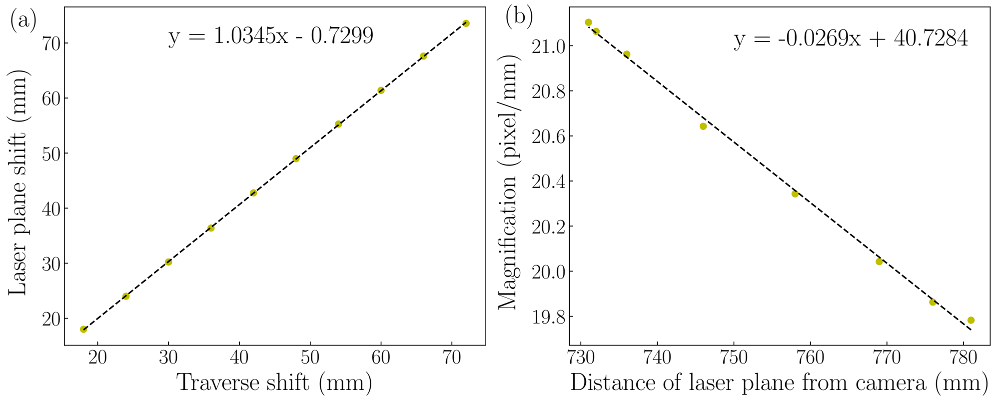

FIGURE 3.13: The calibration curve for positioning the traverse to give a specific laser plane location is shown in (a). The imaging magnification factor is shown to vary linearly (b) as the laser plane position changes.

(2008). An interrogation window of 32 pixels $\times$ 32 pixels with 75% overlap yielded a 249×198 array of velocity vectors in a captured area of approximately 80×64 mm^2. The number of bad vectors in the cross correlation was more for the out-of-focus images, as illustrated in figure 3.14. The PIV images sampled in the middle portion of the scan, equivalent to a normalised distance $\Delta(r/b) = 0.25$, resulted in a total number of bad vectors below 5%.

To reconstruct the two-component velocity field over the entire wing span, the optical components were shifted to different positions along the span. The camera focus was readjusted and the scanning PIV measurements were repeated at the new positions. This was achieved by mounting the optical components on a motorised linear traverse (model: Zaber T-LSR450) controlled using Zaber Console software. However, it was observed that the laser plane position shifted slightly more than the traverse travelled. This was due to a small error introduced by a minute misalignment of the optics. Hence, the traverse was calibrated to give the actual travel matching the laser plane position. The calibration showed the resultant laser plane shift for a given traverse shift, as can be seen in figure 3.13 (a).

During the scanning PIV recording, the laser plane was shifted by a certain distance towards the camera; however, the camera position remained fixed. Hence, the distance between the laser plane and the camera changed, thereby changing the magnification factor. This change to the magnification factor was calibrated with the laser plane position. The calibration results show a linear relationship in figure 3.13 (b). Based on

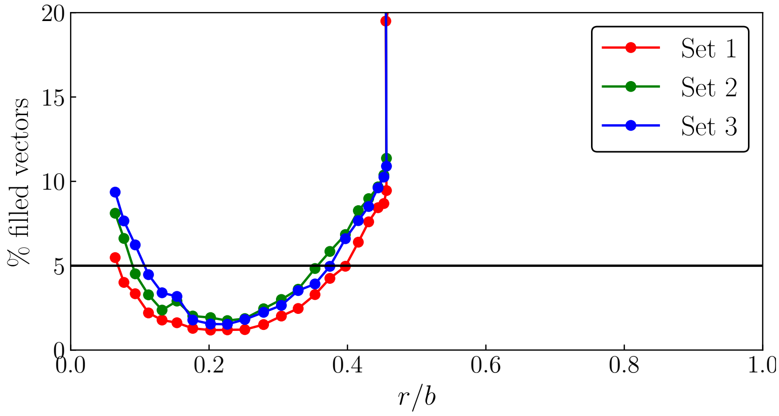

FIGURE 3.14: Measurements of the filled (bad) vectors in PIV imaging.

the actual distance of a PIV image, the magnification factor was determined by linear interpolation.

During the recording of scanned PIV images, the position of the linear traverse was fixed and the fluid volume was subsequently scanned. The distance of the laser plane from the wing root (r) was normalised by the wing span (b). The camera was focussed at the centre of the scanned volume. As the volume was scanned, the imaging varied from out-of-focus to in-focus and then to out-of-focus again. In general, images taken further from the focal plane resulted in a greater number of bad vectors than the better-focused images, as shown in figure 3.14.

At a fixed position of the traverse, scanning PIV measurements were undertaken to produce three full independent datasets. For each set, three central consecutive scanning cycles were chosen from 16 cycles, as discussed earlier. Thus, 9 sets of PIV images for each spanwise position were obtained. The two-dimensional planar velocity fields were computed separately for each set by cross-correlation. Finally, the flow quantities were averaged to give a mean flow field within each spanwise plane for each scanned volume. Figure 3.15 shows the evolution of typical LEVs using averaged vorticity contours obtained from the scans, where the vortex structures are identified by the Q-criterion (Hunt *et al.*, 1988) ignoring the unmeasured through-plane velocity component. It can be seen that the flow separates at the leading edge, forming the characteristic LEV. The LEV grows in size with increasing r/b. Increased numbers of bad vectors, due to poorer illumination in the scan, are observed in the last four images. Some noise is also seen in the contours at the start of the scan, where the particles were more out-of-focus. For

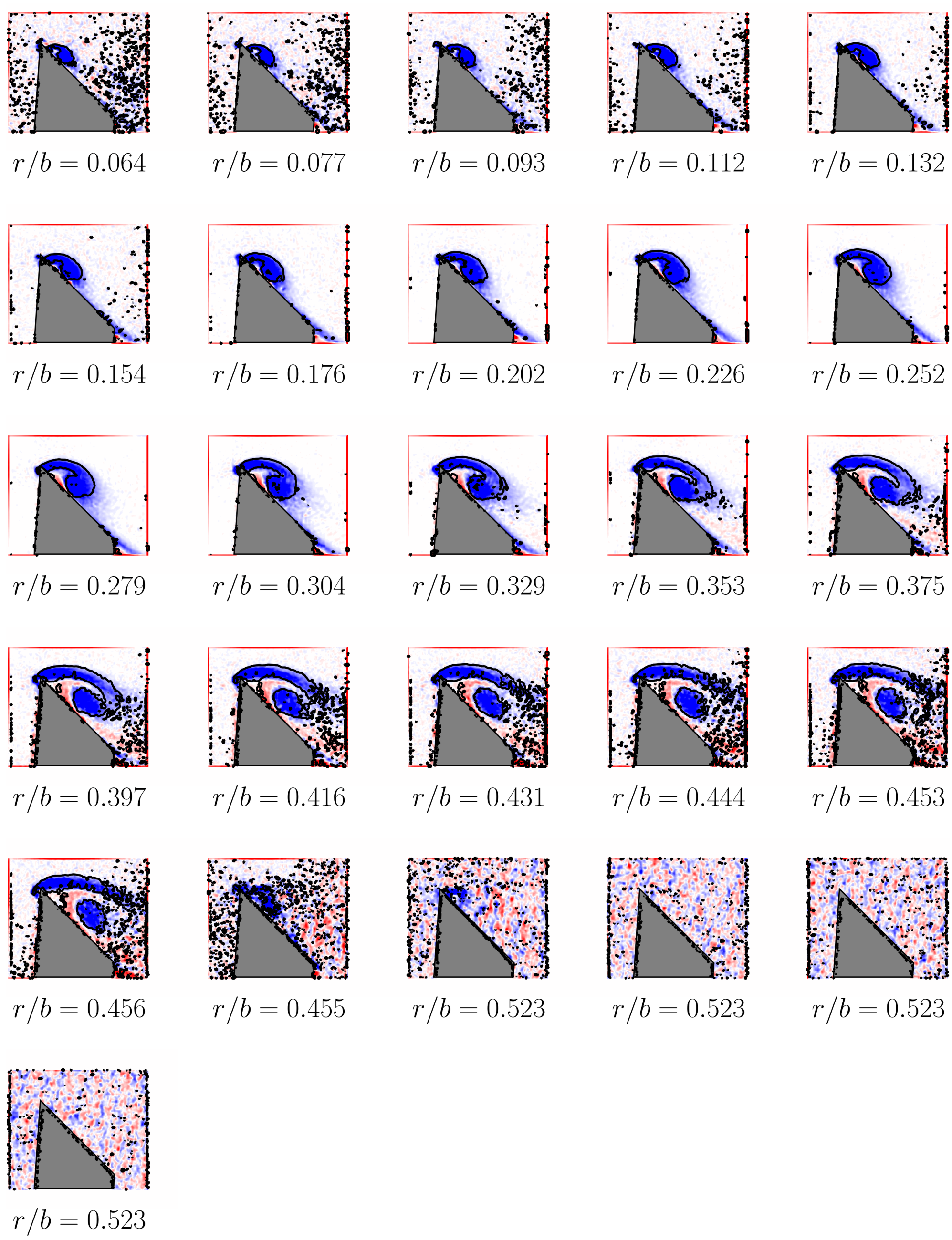

FIGURE 3.15: A typical series of vorticity contours obtained from a cycle of the scanning PIV. The normalised vorticity range is $\omega_z^* = \omega_z b/U_g \in [-30, 30]$. The black lines represent the vortices identified by the Q criterion. The images at the end of the scan are poorly illuminated, and hence, can be ignored. The noise levels for Q are also high for the planes that are out-of-focus. The LEV is observed to increase in size in the spanwise direction, and splits at $r/b \simeq 0.416$.

the above results, a scanning resolution of $\Delta(r/b) = 0.025$ was achieved with the help of the fast scanning speed coupled with a high-speed camera, both described earlier. The wing, camera, and the motor for the scanning laser sheet system were controlled by a real-time control system described in the following section.

3.1.6 Force measurements

The lift and drag forces on the rotating and flapping wing at low Reynolds numbers were estimated from the force coefficients in the literature. The estimated values for the wing motion in water were of the order of 10mN. Hence, an accurate, commercially available force and torque transducer, ATI Nano17 IP68 was employed to measure the forces and the torques on the wing.

The ATI Nano17 IP68 is a 6-signal F/T transducer providing the forces and torques in the three Cartesian coordinate axes. We were interested in measuring the forces and torques along the X and Y axes of the transducer, which were aligned in the normal and tangential direction, respectively, to the wing surface. The calibration for the measurements along these two axes was performed as described below.

3.1.6.1 Force and torque calibration

The schematic of the setup used for calibrating the F/T transducer is shown in figure 3.16. The ATI transducer was attached to a vertical plate rigidly mounted on a frame. The attachment was fabricated in such a way that either of the X or Y axes could be aligned vertically. The alignment of the frame was ensured using a digital spirit level. After the transducer was mounted, a horizontal bar with a flange was attached to it, which acted as a moment arm. A pan with chosen weights could be hung at any chosen distance along the moment arm.

The transducer cable was connected to the interface and power supply (IFPS) box, which was further connected to the Beckhoff analog input terminals attached to EK1100 EtherCAT coupler. The coupler transferred the input signals to the computer. The acquired signals were recorded using TwinCAT3 software. The IFPS box was calibrated by the supplier and a calibration matrix was provided to convert the raw voltages into the forces and torques. This calibration was verified by applying the forces and torques along the axes of interest, i. e. along X and Y axes.

First, the weight of the moment arm and the pan were noted by weighing them on an electronic balance. The applied force was varied by systematically changing the

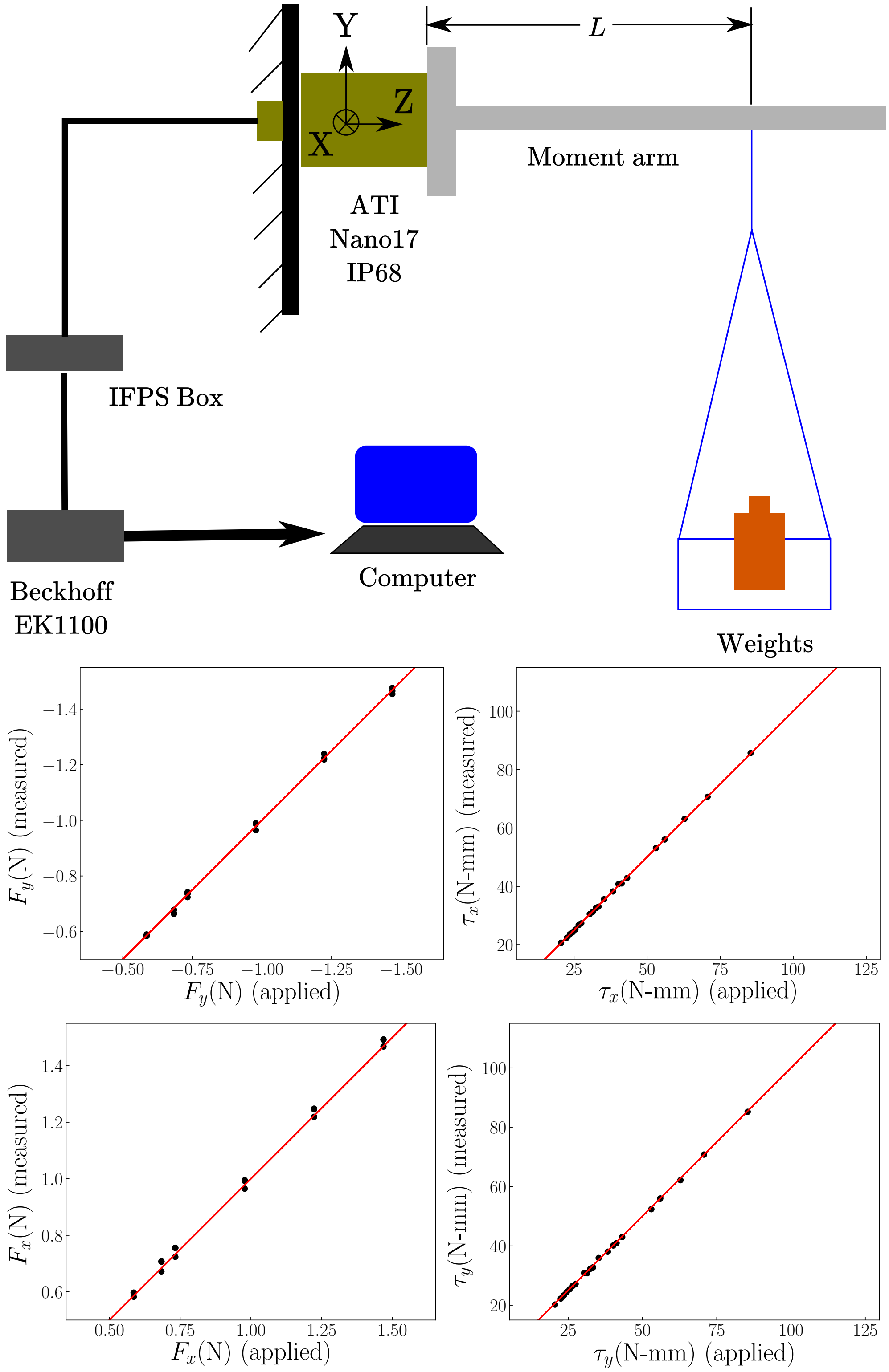

FIGURE 3.16: Schematic of the setup used for the calibration of the F/T transducer (ATI Nano17 IP68) and the calibration plots for the forces (F_x and F_y) and torques (τ_x and τ_y).

weights in the pan. The value of torque applied can be computed as the force multiplied by the distance on the moment arm (L), where the weight was hung. For every applied weight, the transducer signals were recorded for 60 seconds. The recorded signals were averaged to compute the mean measured forces and torques.

Firstly, the Y axis was aligned in the vertical direction and the forces were applied along the negative Y axis. The same force also implicitly applied a torque along the X axis. The force and torque were varied by adding different weights in the pan hanging at a distance L from the transducer. In addition to the change in the weights, the distance L was also varied to change the applied torque. By changing L, for a constant applied weight, the value of the measured force varied slightly with an error of $< 4\%$. The torque measurements were found to be relatively more accurate, with an error of $< 1\%$. The same procedure was repeated by aligning X axis in the vertical direction and applying the forces along the positive X axis that simultaneously applied the torques about Y axis. The plots of the measured forces and torques against the applied forces and torques can be seen in figure 3.16.

3.1.7 Real-time control system

A real-time control system with high temporal accuracy was required to accurately control and trigger such a complicated experimental rig consisting of a high-speed camera for PIV imaging and motors for driving the wing model and the rotating mirror and the force/torque measurement sensor (ATI Nano17 IP68). This was achieved by developing a system based on EtherCAT (Ethernet for Control Automation Technology). In this system, the motor drives (model: Maxpos 50/5, Maxon Motor), the analog input modules for recording the signals from the F/T sensor and the digital I/O modules for the triggers were connected to an EtherCAT coupler (model: EK1100, Beckhoff). The coupler was connected via an Ethernet cable to a high-performance workstation computer that was equipped with the Beckhoff TwinCAT3.1 real-time software providing a real-time accuracy of 0.125 ms. Customised GUI (graphical user interface) programs were developed to control the real-time tasks. The schematic of the real-time control system is shown in figure 3.17.

3.1.8 Flow visualisation

The flow around a rotating or flapping wing of finite span is three dimensional. Dye visualisation and hydrogen bubble visualisation techniques were validated to observe

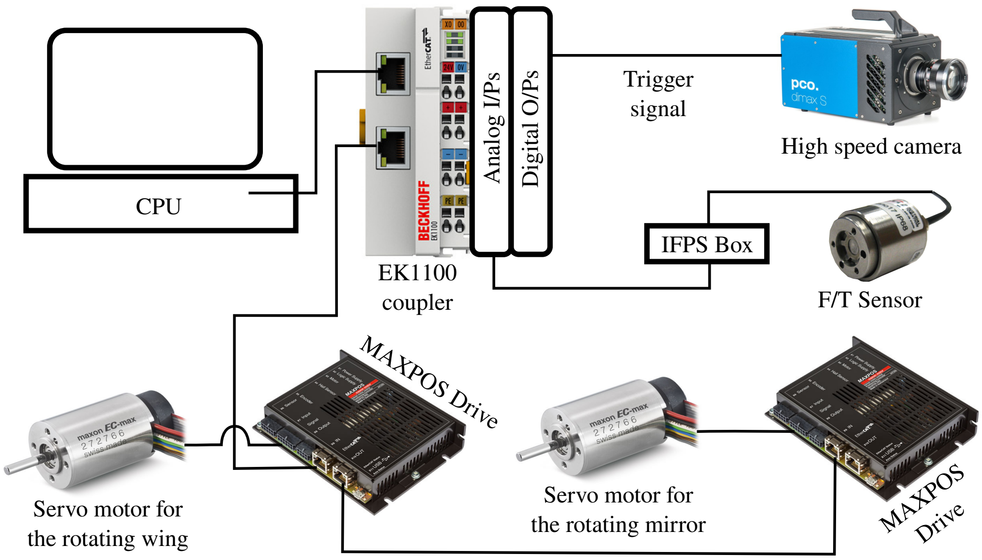

FIGURE 3.17: The real-time control system included servo motors, controllers, a high speed camera and a F/T sensor connected to a computer via an EtherCAT coupler.

the flow qualitatively.

3.1.8.1 Dye visualisation

The traditional dye visualisation technique involves a continuous flow of a dye injected in the flow close to the formation of the shear layer. In the present study, the leading edge acted as the location of the separation of the shear layer that formed the LEV. The continuous injection of a dye would require the dye velocity to be nearly equal to the velocity of the flow surrounding the point of injection. However, in the present study, the flow velocity varied in time due to the wing's motion profile and also varied along the wing span since the wing was rotated about the central axis, which made it difficult to inject the dye directly over the leading edge. Hence, a mixture of a dye and other chemicals was applied on the leading edge to adhere to it before inserting the wing in water. Leweke (2012) has suggested an addition of a thickening agent, such as honey, which makes the dye solution syrupy, making it easy to spread over a solid surface.

In our experiments, two different substances were tested as mixing agents. In the first test Rhodamine-B dye and honey were mixed and applied on the leading edge. The applied mixture was allowed to dry for 20 minutes and was then inserted in water. The dye was illuminated using white light from a halogen lamp. However, as soon

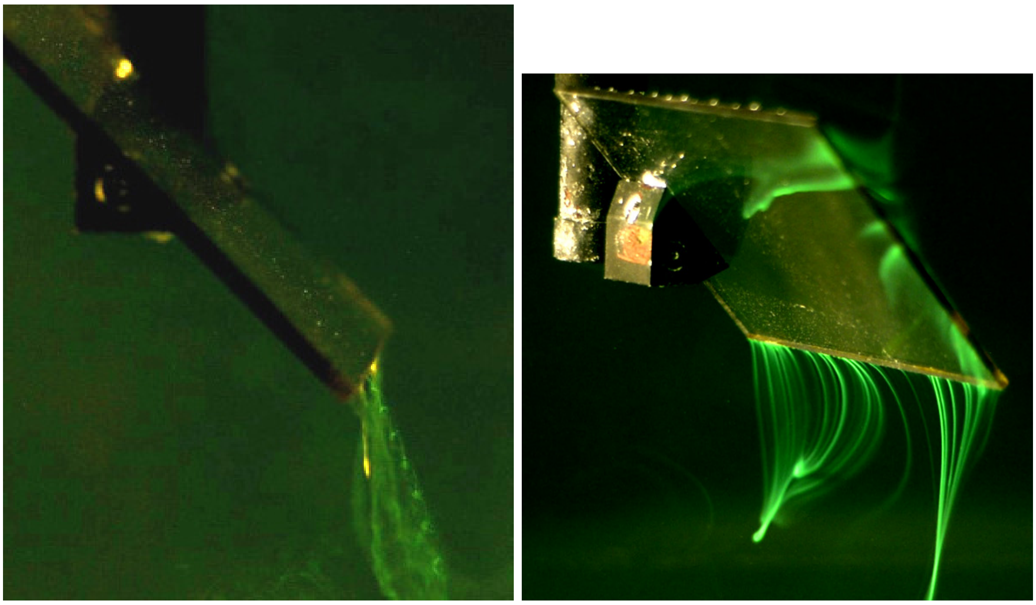

FIGURE 3.18: Dye mixed with, (a) honey gives poor contrast and higher density than water, (b) acrylic paint gives better contrast and density close to water.

as the wing was inserted in water, the heavy drops of honey (density $\sim$ 1400 kg/m^3) started dropping under gravity. The captured images show much less colour contrast as can be seen in figure 3.18 (a). In the second test, an acrylic paint (colourless Epoxy Enamel) was mixed with the dye (Rhodamine-B). The density of this mixture was close to that of water ($\sim$ 1000 kg/m^3). A similar procedure was followed as above, with a drying time of 10 minutes. This mixture had the density close to that of water. Hence, it did not flow downwards under gravity. It can be seen from figure 3.18 (b) that the illumination is better than for the dye-honey mixture.

However, it was challenging to maintain the dye adhering to the leading edge for a long period. Most of the dye would immediately flow out in the initial acceleration phase of the wing, leaving very little dye available to visualise the leading-edge vortex (LEV) formed later. Following these tests, the hydrogen bubble technique was validated to visualise the LEV.

3.1.8.2 Hydrogen bubble visualisation

The dye visualisation technique required repeated dismantling of the setup to apply the dye to the wing leading edge. However, hydrogen bubble visualisation did not require the setup to be dismantled between sets of experiments. In this technique, the flow

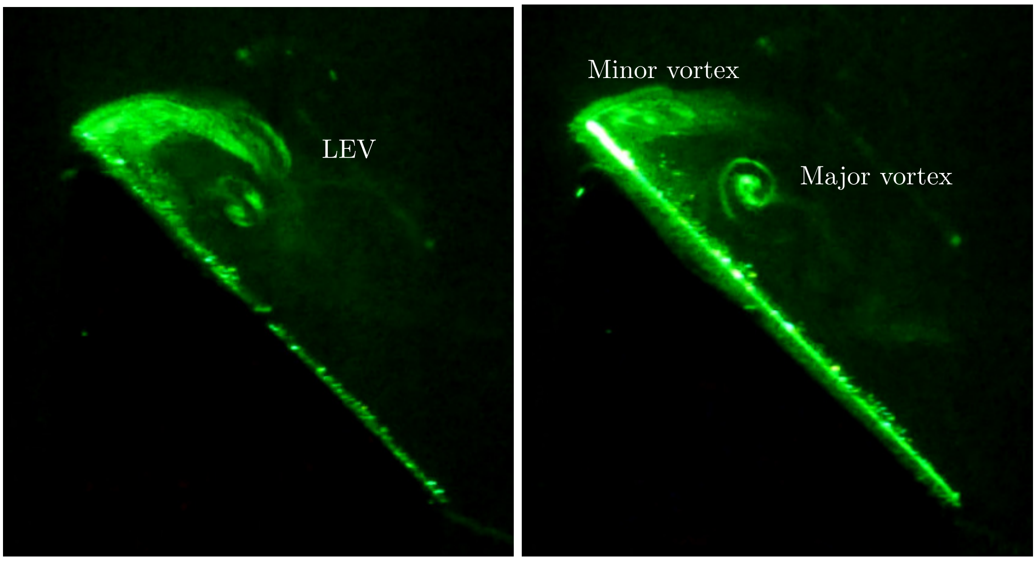

FIGURE 3.19: The hydrogen bubble visualisation of the leading-edge vortex of a fruit fly wing planform rotating at $Re = 1000$ can be see in (a). At a higher Reynolds number ($Re = 1500$), two co-rotating vortices, termed as the dual-LEVs, can be seen in (b). A minor vortex near the leading edge is formed by the secondary separation, while the primary shear layer has formed the major vortex.

is visualised by generating tiny hydrogen bubbles near the region of interest. In the present work, a tungsten wire of diameter 25 µm was attached to the leading-edge, which acted as a cathode. An aluminium bar inserted in the water tank acted as an anode. When connected in a DC circuit of 30V supply, the electrolysis of water caused the thin cathode wire to release hydrogen in the form of tiny bubbles. The smaller bubbles had lower buoyancy forces; hence, they followed the leading-edge shear layer before rising to the water's surface.

The bubbles were illuminated using either the white light or the laser sheet. The laser illumination in a plane provided a better view of the LEV than the poorly illuminated 3D view by the white light. In figure 3.19, the pictures of the LEV and the dual-LEVs can be seen, which are captured using the hydrogen bubbles illuminated by the laser.

3.2 Computational method

3.2.1 Solver setup

The computational method used in this study has been adopted from Harbig *et al.* (2013). The flow over a rotating wing was modelled by the Navier-Stokes and continuity equations cast in a non-inertial rotating frame of reference. The 'alternate rotation model' was used to minimise the numerical error, in which the solver advects the absolute frame velocity instead of the rotating frame velocity. Thus, the advection and transient terms of the N-S equation were modified to involve the absolute frame velocity. The solver equations were written as

$$\frac{\partial \rho \boldsymbol{u_{abs}}}{\partial t} + \boldsymbol{\nabla} \cdot (\rho \boldsymbol{u} \boldsymbol{u_{abs}}) = -\nabla p + \boldsymbol{\nabla} \cdot \boldsymbol{\sigma} - \rho \boldsymbol{\Omega} \times \boldsymbol{u} - \rho \boldsymbol{\Omega} \times (\boldsymbol{\Omega} \times \boldsymbol{r}) \tag{3.5}$$

and

$$\boldsymbol{\nabla} \cdot \boldsymbol{u} = 0, \tag{3.6}$$

where ρ is the density, p is the pressure, $\boldsymbol{\Omega}$ is the rotational velocity vector, $\boldsymbol{u}$ and $\boldsymbol{u_{abs}}$ are the velocity vectors in rotating and absolute frames respectively. The angular acceleration in included in the transient term as $\boldsymbol{u_{abs}} = \boldsymbol{u} + \boldsymbol{\Omega} \times \boldsymbol{r}$. The stress tensor $\boldsymbol{\sigma}$ can be defined as

$$\boldsymbol{\sigma} = \mu[\boldsymbol{\nabla u} + (\boldsymbol{\nabla u})^T - \frac{2}{3}\boldsymbol{I}\boldsymbol{\nabla} \cdot \boldsymbol{u}], \tag{3.7}$$

where $\boldsymbol{I}$ is the identity matrix.

These equations were solved directly using the commercial code ANSYS CFX version 17.2.

3.2.2 Wing geometry and motion

As described in § 3.1.1, the wing geometry was based on a generic fruit fly wing (*Drosophila melanogaster*). The basic wing was modelled to be of a similar scale to that of the actual fruit fly (Zanker & Götz, 1990) with a wing-span (b) of 2.47 mm and an aspect ratio ($\mathcal{A\!R}$) of 2.91. The wings of different aspect ratios were produced by stretching or compressing the original wing shape in the chordwise direction. The thickness to chord ratio of 0.03 was maintained. The wing root was offset from the rotation axis by an amount b_0 such that the total span is $R = b + b_0$. In some cases, the wing was attached to a cylindrical central body to match experimental designs with a wing holder. The central body causes the wing-root to be offset from the centre of

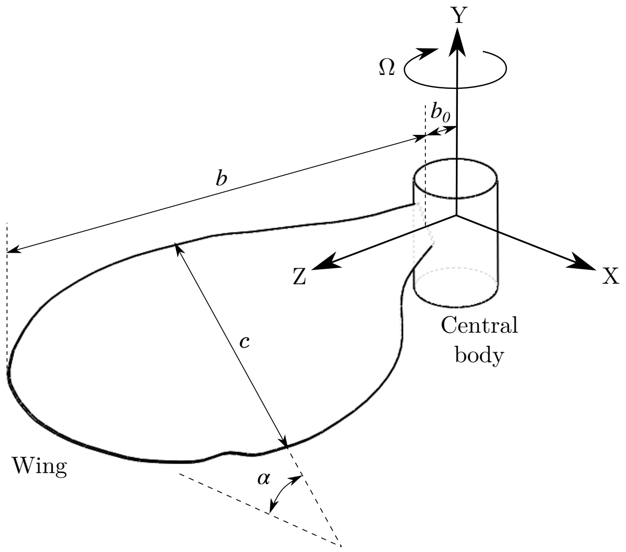

FIGURE 3.20: Schematic of the wing, central body, and the coordinate system.

rotation by an amount b_0. The schematic of the wing, central body, and the coordinate system is shown in figure 3.20.

A simplified wing motion was prescribed in order to obtain the LEV structure that is formed during the mid-stroke of a typical flapping cycle of an insect. This required the wing, initially at rest in a quiescent fluid, to be rapidly accelerated to a constant angular velocity (Ω_c) by rotating about the central axis. Throughout its motion, the wing maintained a constant angle of attack ($\alpha = 45°$) with the horizontal plane. The acceleration period was chosen to be $t = 0.084T$, the same as that used by Harbig *et al.* (2013), where T is the total simulation time. An impulsively started wing has been shown to be comparable to the beginning of the downstroke of a flapping cycle (Poelma *et al.*, 2006), with the acceleration period typically ranging between 6 and 10% of the total simulation time (Birch *et al.*, 2004; Lentink & Dickinson, 2009b). With a constant angular velocity, the flow over the wing achieved a quasi-steady state after about $t = 0.3T$, as can be seen in figure 3.21. The simulation was stopped after 270° rotation of the wing. The prescribed motion profile is given by

$$\Omega(t) = \begin{cases} \frac{1}{2}\Omega_c(1 - \cos(\frac{\pi t}{0.084T})), & t < 0.084T \\ \Omega_c, & t \geq 0.084T. \end{cases} \tag{3.8}$$

3.2.3 Computational domain

The geometry was embedded in a cylindrical computational domain similar to that used by Harbig *et al.* (2013). The domain had a diameter $18R$ and a length $48c$, where R is the distance of the wing-tip from the axis of rotation and c is the mean wing chord. The domain was meshed using an unstructured tetrahedral mesh with triangular prism elements near the wing surface. The overall mesh consisted of approximately 40 million elements, with a grid spacing of $0.00725c$ on the wing's surface. Mesh independence was verified by comparing the predicted forces to those with two other meshes generated by scaling the grid spacing by two and four, which resulted in 0.7% and 2.4% difference, respectively, in the lift coefficients averaged over the final 30° rotation ($\overline{C}_L$). The time step was chosen to be $0.00185T$. This was validated by halving the time step, which resulted in a less than 0.1% difference in the mean forces.

3.2.4 Validation studies

Mesh resolution, time-step resolution, and domain size verification studies were performed by Harbig (2014). After modifying the geometry to include the central holder, causing the wing to offset from the axis of rotation, the simulations were run to validate the modified mesh size. The wing of $\mathcal{R} = 2.91$, with a central body causing the normalised offset to the wing root of $\hat{b}_0 = 0.25$ rotating at a low ($Re = 80$) and a high ($Re = 1200$) Reynolds numbers, was used for the validation. The numerical errors were estimated using the *grid convergence index* (GCI) method proposed by Roache (1998). GCI between a coarse and a finer grid is given by

$$GCI = \frac{F_s|\epsilon|}{r^p - 1}, \tag{3.9}$$

where ϵ is the relative error given by $\epsilon = (f_2 - f_1)/f_1$, f_2 and f_1 are the solution values obtained with the coarse and fine grids respectively, r is the grid refinement ratio given by $r = (N_1/N_2)^{1/3}$, N_1 and N_2 are the number of mesh elements with the fine and coarse grids respectively, p is the order of convergence, and F_s is the safety factor. As per Roache (2003), the value of F_s was chosen to be 1.25 for a three-grid convergence study. The mesh sizes were doubled in two successive steps to obtain the fine, medium and coarse grids respectively. The corresponding values of GCI for the lift coefficient (C_L) and drag coefficients (C_D) were calculated for $Re = 80$ and $Re = 1200$, which can be seen in table 3.3. The values for GCI between the medium and the fine mesh

Mesh	Surface Size	Elements (million)	$Re = 80$			
			C_L	GCI(%)	C_D	GCI(%)
1	$0.0286\bar{c}$	6.59	1.346	–	1.536	–
2	$0.0145\bar{c}$	15.58	1.343	0.283	1.521	1.507
3	$0.0072\bar{c}$	80.39	1.338	0.226	1.513	0.319
Mesh	**Surface Size**	**Elements (million)**	$Re = 1200$			
			C_L	GCI(%)	C_D	GCI(%)
1	$0.0286\bar{c}$	6.59	1.666	–	1.572	–
2	$0.0145\bar{c}$	15.58	1.664	0.168	1.577	0.475
3	$0.0072\bar{c}$	80.39	1.665	0.044	1.583	0.250

TABLE 3.3: Mesh resolution study for rotating wing model with a central body.

Time-step	Time-step Size ($\Delta t/T$)	$Re = 80$			
		C_L	GCI(%)	C_D	GCI(%)
1	1/540	1.344	–	1.521	–
2	1/1080	1.338	0.176	1.515	0.164
Time-step	**Time-step Size ($\Delta t/T$)**	$Re = 1200$			
		C_L	GCI(%)	C_D	GCI(%)
1	1/540	1.664	–	1.577	–
2	1/1080	1.657	0.182	1.570	0.180

TABLE 3.4: Time-step resolution study for rotating wing model with a central body.

were found to be less than 0.5%. Hence, the medium mesh sizing was chosen for all the subsequent simulations. Similarly, the time-step resolution was validated by analysing the GCI for the time-steps $\Delta t = T/540$ and $\Delta t = T/1080$, where T is the total solution time. The results obtained at $Re = 80$ and $Re = 1200$ are summarised in table 3.4. The time-step of $\Delta t = T/540$ was chosen for this study, which showed a GCI of less than 0.5% for both C_L and C_D.

The results from the modified mesh sizing were compared to those from the literature. First, the results were compared with the experimental data by Birch *et al.* (2004). The wing of aspect ratio $\mathcal{R} = 2.91$ and an offset ratio $\hat{b}_0 = 0.067$ was rotated at two different Reynolds numbers. The lift coefficient varied with time, as can be seen in figure 3.21. The mean lift coefficient (averaged over last 30° rotation) was observed to be within 5% of that by Birch *et al.* (2004). The lift coefficient was defined by Birch *et al.* (2004) as

$$C'_L = \frac{L}{0.5\rho\Omega^2 R^2 \int_0^1 \hat{r}^2 \hat{c}(\hat{r}) d\hat{r}}, \tag{3.10}$$

where $\hat{r}$ is the normalised wing-radius ($\hat{r} = r/R$), $\hat{c}$ is the normalised wing-chord ($\hat{c}(\hat{r}) =$

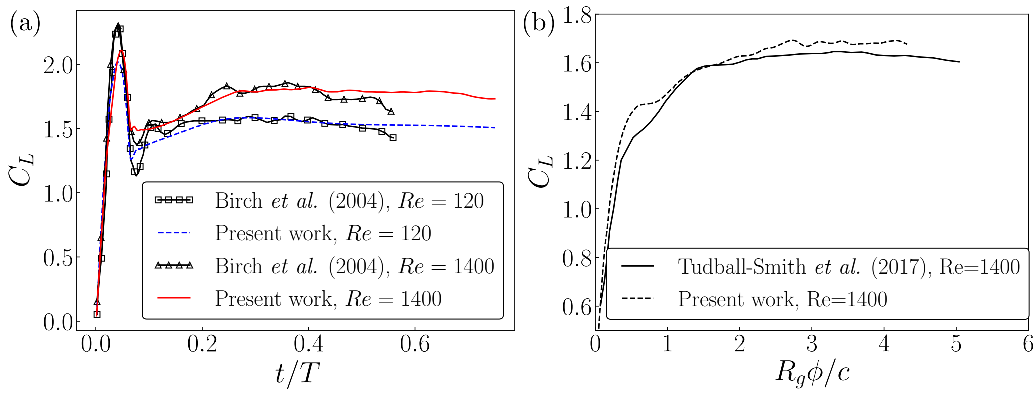

FIGURE 3.21: In (a), the time variation of the lift coefficient for a fruit fly wing planform rotating at $Re = 105$ and $Re = 1400$ is compared with the experimental data at similar Reynolds number by Birch *et al.* (2004). In (b), the time variation of the lift coefficient for a rectangular wing rotating at $Re = 1400$ is compare to that for the same wing from Tudball Smith *et al.* (2017).

$c(r)/\bar{c})$. The lift coefficient in the present work is defined as

$$C_L = \frac{L}{0.5\rho\Omega^2 R_g^2 S}, \tag{3.11}$$

where R_g is the radius of gyration ($R_g = \sqrt{(1/S)\int_0^R r^2.c(r).dr}$) and S is the wing area ($S = b\bar{c}$). Thus, equation 3.10 can be rearranged as

$$\begin{aligned} C'_L &= \frac{L.R}{0.5\rho\Omega^2 R_g^2.S.b} \\ &= C_L(R/b) \end{aligned} \tag{3.12}$$

To compare the experimental data by Birch *et al.* (2004) with the CFD results, the lift coefficient of Birch *et al.* (C'_L) was scaled by (b/R) to calculate C_L. No information was available about the wing-root offset distance in their experiments. Hence, a reasonable offset of $b_0/R = 0.1$ was estimated from their schematic. To match the present way of calculating C_L, the data from Birch *et al.* (2004) were scaled by b/R. The lift values predicted by the present method show a good match with the experiments, as can be seen in figure 3.21(a). A reduction in the forces after $t/T = 0.4$ in experiments may be due to the deceleration of the wing, whereas the wing in the numerical simulations continued to rotate at a constant angular velocity.

An additional validation was carried out for a different velocity profile and wing shape. Tudball Smith *et al.* (2017) ran the simulations with a unity aspect ratio rectangular wing rotating with a constant angular velocity reached after a relatively smooth velocity ramp initiated from rest. Their velocity profile was given as

$$\Omega(t) = \begin{cases} \Omega_c[-20(\frac{t}{\tau_1})^7 + 70(\frac{t}{\tau_1})^6 - 84(\frac{t}{\tau_1})^5 + 35(\frac{t}{\tau_1})^4], & t < \tau_1 \\ \Omega_c, & t \geq \tau_1, \end{cases} \tag{3.13}$$

where Ω_c was the constant final rotational velocity and τ_1 was the time after starting the wing from rest at which the constant rotational velocity was reached. The present computational setup was modified to simulate the rectangular wing with $AR = 1$ and the velocity profile as above. The time trace of the lift coefficient obtained using the present setup shows a close match with that from Tudball Smith *et al.* (2017) as shown in figure 3.21(b). Here, C_L is plotted as a function of the chord-lengths travelled by the wing at the radius of gyration, represented as $R_g\phi/c$, where ϕ is the angular displacement of the wing.

3.3 Summary

The present comprehensive study included both experimental and computational investigations of an insect wing's geometrical and kinematic parameters likely to affect their aerodynamics. The experimental study broadly involved two independent rigs for the wing rotation and flapping motion. The high-speed flow-field measurements were carried out using a newly-developed scanning PIV system and the force measurements were carried out using a force-torque transducer. All the components of the experimental setup and the methods were carefully validated. The computational method involved the setup adopted from a previously established analysis. The computational setup was re-validated successfully after modifying the adopted setup to model the geometries now under investigation.

Chapter 4

Effect of the Central Body

4.1 Introduction

Fluid motion within the leading-edge vortex (LEV) over a rotating insect wing is helical in nature, growing in size from the wing-root to the wing-tip (Ellington, 1999). It could be expected that LEV formation and its spanwise growth might be affected by the presence of a body at the centre of rotation. The central body causes the wing root to be offset from the axis of rotation by an amount ($b_0 = d/2$), where d is the diameter of the body.

The weights of insects directly depend on their body sizes, requiring different lift forces for their flight. A higher lift may be obtained with a larger wing area and a change in wing kinematics. This causes a significant change to the Reynolds number, which affects the near-field and far-field vortex structures, as shown by Liu & Aono (2009). The Reynolds number has been observed to be a significant factor affecting the LEV structure (Harbig *et al.*, 2013; Birch *et al.*, 2004; Lu *et al.*, 2006). However, the focus of the present study is on the change to the LEV structures with body sizes at a chosen Reynolds number. Different insects of similar weights may fly at the same Reynolds number. Their wings could be offset by different amounts depending on their body sizes relative to their wings. The relative change in the Coriolis acceleration can be studied by observing the offsets normalised with the wing spans, instead of studying the overall body sizes.

In the present study, the effects of a change in the central body size on the flow structure is systematically studied. A simplified motion was prescribed to the wing in order to obtain the LEV structure that is formed during the mid-stroke of a typical flapping cycle of an insect. This required the wing to be held at a constant angle to the horizontal ($\alpha = 45°$) and rotated with a constant angular velocity (Ω) without requiring

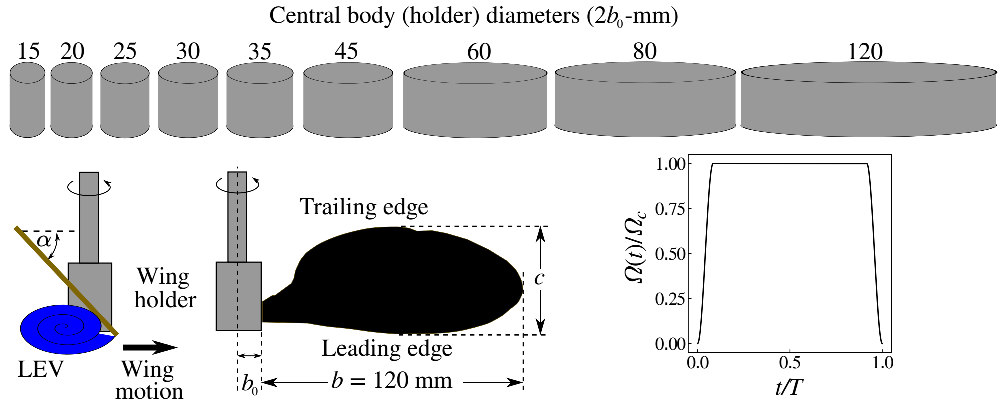

FIGURE 4.1: The different holder sizes allow the normalised wing offset to vary in the range ($0.063 < \hat{b}_0 < 0.5$). The wing was inverted to point the leading-edge downward so as to allow the laser sheet projected from the bottom to illuminate the LEV. The chart on the right shows the angular velocity profile in time. Here, the instantaneous angular velocity $\Omega(t)$ is normalised by the constant angular velocity reached after $t/T = 0.085$.

the wing-flip and stroke-reversal. The wing was initially uniformly accelerated over a time of $\Delta t = 0.085T$, where T is the total time for one complete rotation. After this acceleration, the wing reached a constant angular velocity corresponding to the chosen span-based Reynolds number given by

$$Re_b = \frac{U_g b}{\nu}. \tag{4.1}$$

Here, U_g is the velocity at the radius of gyration ($U_g = R_g\Omega$), R_g is the radius of gyration of the wing, b is wing span, and ν is the kinematic viscosity of water. Central bodies of different sizes are chosen such that the normalised offset varies in the range ($0.063 < \hat{b}_0 < 0.5$), which overlaps and extends beyond the offset-ratio range of most insects. The offset values scaled with the wing-chord vary in the range ($0.18 < b_0/c < 1.45$). Figure 4.1 shows a schematic of different holder sizes with respect to the wing. As indicated, the wing shape is chosen based on a generic fruit fly wing planform, which is kept constant throughout the range of studied offset ratios and Reynolds numbers ($600 < Re_b < 3000$). Although this range does not include the Reynolds number for *Drosophila Melanogaster* due to the experimental limitations, it includes a larger fruit fly species, *Drosophila Mimica*, and we note that different insects such as honeybees and bumblebees have similar wing aspect ratios as that of the chosen wing (Lehmann, 2002; Dudley & Ellington, 1990; Vance, 2009).

In the present study, the LEV structure for the rotating wing attached to different bodies is obtained by performing scanning-PIV experiments. Unlike insects, the central body in experiments also rotates with the wing. Due to the limitations of attaching the wing holder to the rotating shaft in experiments, a separate numerical study is conducted with and without the rotation of the wing holder. This study shows no significant effect on the LEV structure between the two cases.

The LEV is responsible for the low pressure region created on the suction surface of the wing. The pressure distribution on this surface depends on the LEV structure. The split that can occur in the LEV is a prominent feature that can affect the suction. Hence, in the experiments, the difference between the LEV structures for a range of body sizes and Reynolds numbers is observed by comparing the split location of the dual-LEVs, using a similar method to Harbig *et al.* (2013). Even though the LEV can be thought to be influenced by the change in the secondary flow near the wing root and also by the change in the rotational accelerations with the change in offset, at a given Reynolds number, a negligible effect on the LEV-split is observed in the present experiments for the offsets $\hat{b}_0 \leq 0.25$. Interestingly, the vorticity in the secondary vortex weakens with an increase in the offset and eventually, for the larger offsets, the secondary vortex does not split from the primary LEV. Hence, beyond a certain central body size, the LEV structure changes markedly. Coincidentally, the range of offsets showing a minimal effect on the LEV structure coincides with the range of offsets for most insects ($\hat{b}_0 \leq 0.14$).

4.2 Determining the LEV characteristics

The data sets obtained from the scanning PIV at different spanwise planes, for $\phi = 270°$, were stitched together to build a 3-D view of the LEV. The LEV centre was identified by the local maximum of the scalar γ_1 using the criteria of Graftieaux *et al.* (2001). Here, γ_1 was calculated from the PIV data at each spanwise interval as:

$$\gamma_1 = \frac{1}{N} \sum_S \frac{(PM \wedge U_M) \cdot z}{||PM|| \cdot ||U_M||}, \tag{4.2}$$

where M is any point in an area S around point P, z is the unit normal vector, U_M is the velocity vector at M, and N is the number of points M inside S. γ_1 is equivalent to the ensemble average of the term $\sin(\theta_m)$, where θ_m represents the angle between the radius vector PM and the velocity vector U_M. The locations of the vortex centres identified on different spanwise planes are plotted in figure 4.3(a). In this figure, two

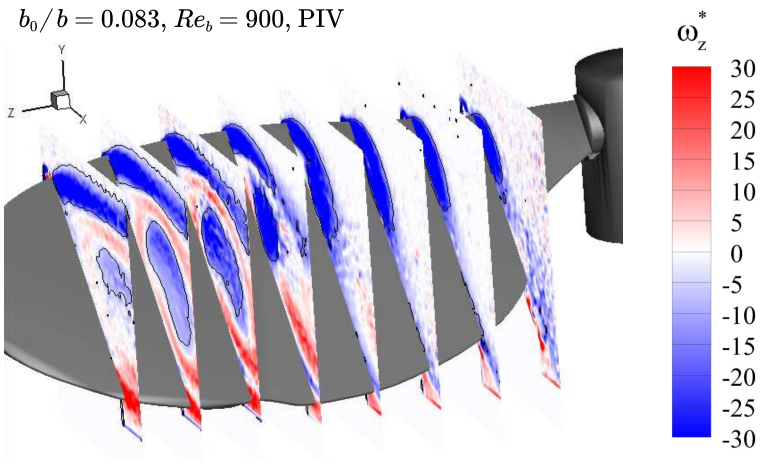

FIGURE 4.2: Vorticity plots at different spanwise locations, obtained from the scanning PIV are plotted. The normalised vorticity range is $\omega_z^* = \omega_z b/U_g \in [-30, 30]$. The black lines represent the vortices identified by the Q criterion.

different LEV centres can be seen. LEV1 remains close to the leading edge while LEV2 moves inward. The LEV centres identified from PIV images show a good match with the numerical predictions of Harbig *et al.* (2013).

An examination of the vorticity contours in figure 4.2 shows that as the distance between the leading edge and LEV2 increases and LEV2 grows in size, there exists a region of positive vorticity beneath LEV2, kinematically generated by the induced velocity gradient at the surface to satisfy the no-slip boundary condition. With an increase in r/b and an increase in LEV2 circulation, this region of positive boundary layer vorticity grows in size, diffuses away from the boundary, and is advected clockwise around LEV2. As this secondary vorticity moves towards the separating shear layer it will weaken and effectively sever it, stopping vorticity being fed into LEV2 and allowing LEV1 to form a separate structure. Lu *et al.* (2006) provide further discussion of this splitting process.

The location of the split can be quantified by computing the circulation of the LEVs. The circulation of the LEV structure was calculated using the field γ_2 of the vortex core identification algorithm of Graftieaux *et al.* (2001).

$$\gamma_2 = \frac{1}{N} \sum_S \frac{[PM \wedge (U_M - U_P)] \cdot z}{||PM|| \cdot ||U_M - U_P||}. \tag{4.3}$$

The region with $|\gamma_2| > 2/\pi$ represents the flow locally dominated by rotation. The circulation of the LEV was calculated by integrating the vorticity inside this identified

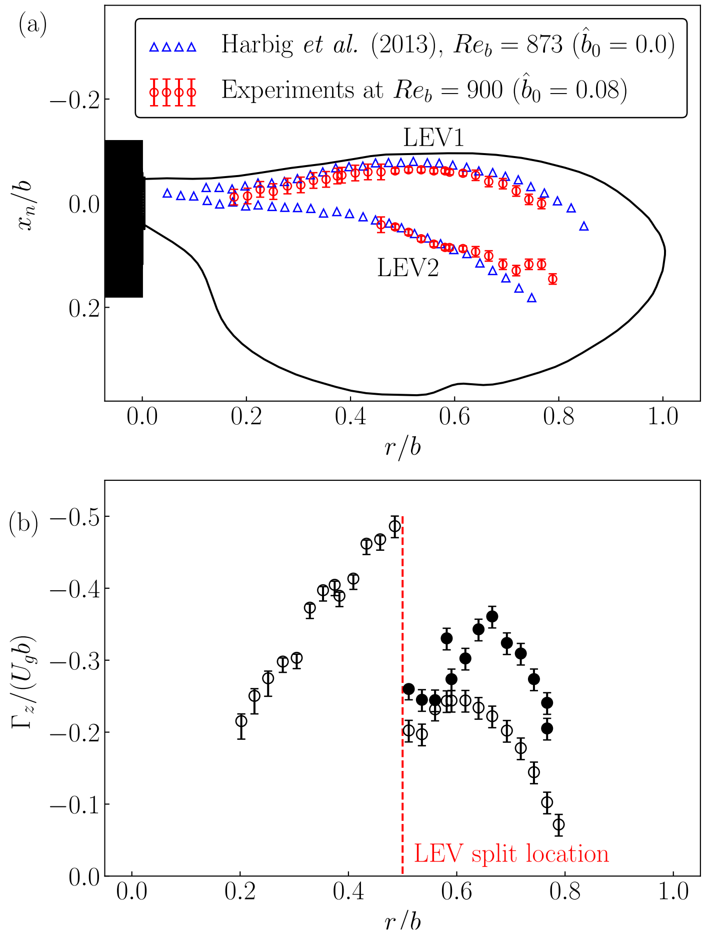

FIGURE 4.3: In (a), the LEV centres identified using the local peak of γ_1 from PIV images are plotted along with those reported by Harbig *et al.* (2013). The LEV split was identified by the sudden drop in the sectional circulation around the LEV region ($|\gamma_2| > 2/\pi$) as seen in (b). The open symbols represent the LEV close to the leading edge, whereas the filled symbols represent the secondary LEV split from it.

region. The normalised circulation ($\Gamma_z/U_g b$) was observed to increase as we move away from the wing root. At some spanwise location, the circulation drops and shows two values corresponding to the dual-LEVs. This location is identified as the LEV-split location, as can be seen in figure 4.3(b). The split location depends on the Reynolds number, as shown in a later section.

4.3 Effect of phase angle

Initially, the LEV formation and its overall variation with the phase angle of wing rotation (ϕ) was investigated experimentally. The wing, with an offset ratio $\hat{b}_0 = 0.08$,

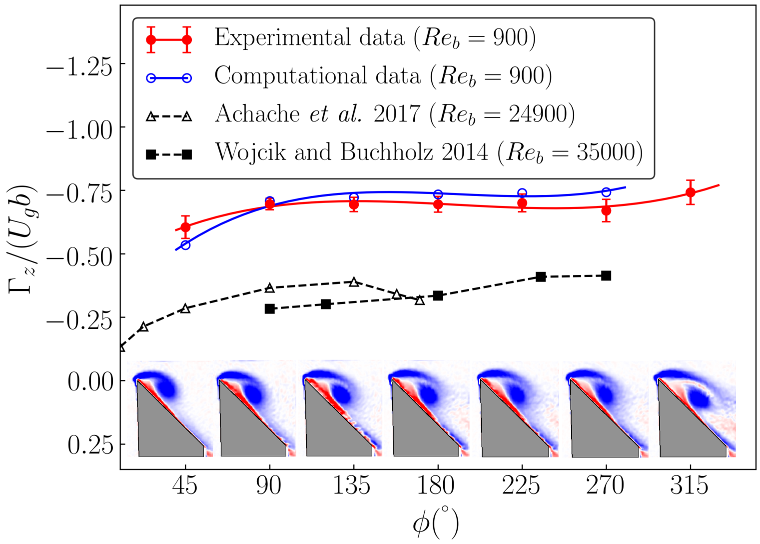

FIGURE 4.4: As the wing rotates, the LEV (shown by the contours of ω_z^* obtained at $z/R = 0.55$) is found to grow in size in the initial phases and then remains stable. The normalised circulation ($\Gamma_z/U_g b$) increases initially until $\phi = 90°$ and remains unchanged until $\phi = 270°$. The development of circulation is compared to the numerical predictions with a similar geometry. The results are also compared to the results at high Re_b reported by Achache *et al.* (2017) for a hummingbird wing ($\mathcal{R} = 3.35$) rotating with $\alpha = 30°$ and those by Wojcik & Buchholz (2014) for a rectangular wing ($\mathcal{R} = 4$) with $\alpha = 35°$, both at $z/R = 0.5$.

was rotated with a constant angular velocity corresponding to a Reynolds number of $Re_b = 900$, and PIV images were recorded at different phases in steps of 45°. Figure 4.4 shows the evolution of the LEV as the wing is rotated. The prominent vortical structure identified as the LEV is visualised through the spanwise vorticity field. The LEV is initially compact at $\phi = 45°$, and then increases in size. Beyond $\phi = 135°$, it maintains a constant size and strength over most of the rotation cycle. However, clearly the LEV size changes towards the end of the rotation period, possibly due to interference with residual vorticity generated at the start of the rotation. The generally accepted reason behind the stable size of the LEV, despite it being continuously fed circulation from the separating shear layer, is the stable rotational acceleration, as described by Lentink & Dickinson (2009b).

The stability of the LEV can be shown quantitatively by calculating the circulation in the area around the LEV and examining how it changes over the rotation. The circulation of the LEV is calculated using the method described in § 4.2. The development of the circulation with the phase angle (ϕ) can be seen in figure 4.4. The initial increase in the normalised circulation ($\Gamma_z/U_g b$) observed during the acceleration ($\phi < 90°$) has also been reported by Achache *et al.* (2017) and Elimelech *et al.* (2013). The circulation remains unchanged during the rotation phase over the range $90° < \phi < 270°$. This observation is consistent with the stable lift observed in the same range in experiments by Birch *et al.* (2004) (for $\alpha = 40°$) and numerical simulations by Harbig *et al.* (2013) (for $\alpha = 45°$). The normalised circulation values predicted numerically by simulating the same geometry are observed to be close to those observed in experiments, with a small variation ($< 10\%$). A comparison with the circulation obtained by Achache *et al.* (2017) and Wojcik & Buchholz (2014) also showed a relatively stable circulation post $\phi = 90°$. The values from both the studies have been scaled as per the present method of normalising the circulation. It should be noted that the overall lower values in both the cases, compared to the present results, may be due to their higher wing aspect ratios, owing to the fact that the circulation reduces significantly with an increase in Æ (Harbig *et al.*, 2013). The lower values of α and differences in the wing shapes in both compared to the present case could be the additional factors that may have caused this reduction in circulation. The drop in the normalised circulation post $\phi = 135°$ observed by Achache *et al.* is due to the deceleration of the wing.

4.4 Effect of holder rotation

Since it is difficult to maintain a stationary central body in experiments, the effect of its rotation was studied by simulating the wing rotation numerically with and without the motion of the holder. The two conditions were compared by observing the lift forces on the wing. A large holder ($b_0/b = 0.25$) and a large Reynolds number ($Re_b = 3000$) were selected to accentuate possible differences. As can be seen in figure 4.5, there is a negligible difference in the lift coefficients in the two cases with the rotation of the wing. Thus, the experiments with a rotating holder can be assumed to exhibit the same effects as that of a stationary central body.

4.5 Effect of Re_b and presence of a central body

An overall increase in the body size of an insect causes an increase in its mass and the Reynolds number. The effect of Re_b on the LEV structures was studied by tracking the change in the LEV-split location. Lu *et al.* (2006) have reported that the dual-LEVs could be observed only for the chordwise Reynolds numbers $Re > 640$. However,

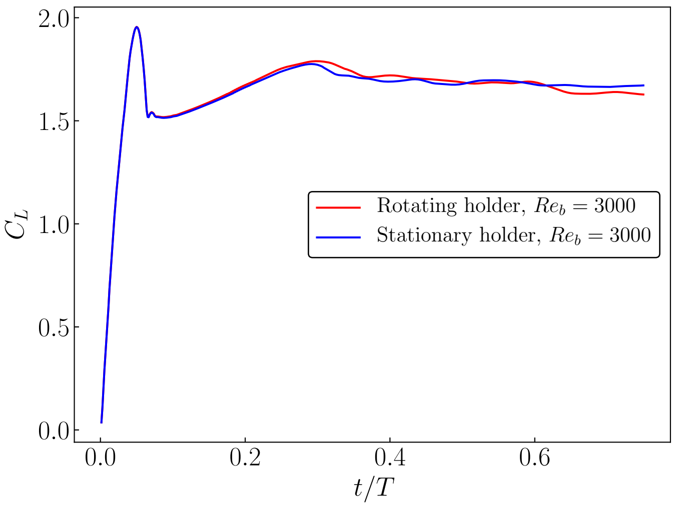

FIGURE 4.5: The lift coefficients on the wing for a large holder ($b_0/b = 0.25$) with and without its rotation remain mostly unchanged even at a large Reynolds number ($Re_b = 3000$).

we observed the dual-LEVs even at $Re_b = 900$ which corresponds to the chordwise Reynolds number $Re = 290$. Even though the existence of dual-LEVs was reported by Lu *et al.* and Carr *et al.* (2015), the split location was found to be tracked with Re only by Harbig *et al.*. Hence, to provide a level of validation, the experimental results are compared directly with the numerical predictions of Harbig *et al.*. The wing geometry and kinematics are identical for this comparison. The only difference is that the numerical study does not model the central holder that is present in the experiments. The Reynolds number range investigated was $920 < Re_b < 8750$. The split location normalised by the wing span (i.e. , r/b), is plotted as a function of Re_b in figure 4.6.

The present results and those of Harbig *et al.* (2013) show the same trend, with the split location shifting radially inwards as the Reynolds number increases. It should be noted that in the original analysis to determine the variation of the split location with Reynolds number, Harbig and co-workers used the standard Q-criterion including the spanwise velocity component. That leads to slightly increased outward split positions, as can be seen from the curve corresponding to Q3 in figure 4.6. Thus, their data were reanalysed here to use the same criterion (Q2) as in these experiments, i.e., still using the Q-criterion but neglecting terms involving the spanwise velocity component,

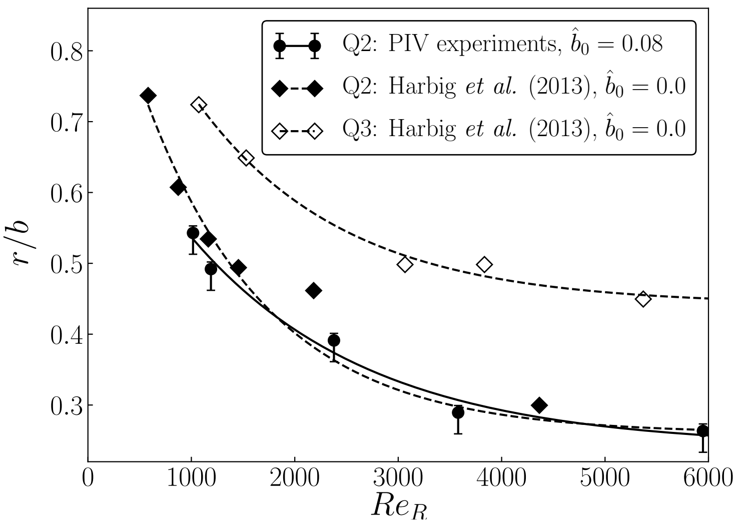

FIGURE 4.6: The normalised spanwise location (r/b) for the LEV split is shown as a function of Re_b. The experimental data are for the wing with a central body and the computational data by Harbig *et al.* (2013) are for the wing without a central body and no offset. Here, Q2 represents the use of 2D Q criterion and Q3 represents the use of 3D Q criterion.

which that was not measured in the experiments. Clearly, figure 4.6 shows that the experimental and computational split locations match to within a few percent over the Reynolds number range considered, despite the presence of the 10 mm radius holder, although noting that it equates to only $\sim 8\%$ of the wing span.

There may be several reasons behind the inward shift of the LEV split location with an increase in Re_b. First, at a high Re_b, the reduced viscous effects cause a reduction in the diffusion of the vorticity of LEV2, therefore confining it to a smaller volume and making it more concentrated. This increased vorticity of the LEV in proximity to the wall would induce stronger secondary positive vorticity at the surface beneath LEV2. This vorticity is then advected more strongly around the LEV at higher Re_b because the velocity closer to the surface will be higher, to interact with the leading edge separating shear layer, as discussed previously. This process may cause the LEV structure to separate and split at a more inward location than that at a lower Re_b. Second, the increased turbulence at even higher Re_b may make the LEV structure more unstable and prone to split at a more inboard location. This suggests that the movement of the LEV split towards the wing root at a higher Re_b may be due a combination of factors.

However, in general, the presence of the central wing holder causes the wing root to be offset from the axis of rotation, thus affecting the Rossby number. It also generates secondary flow at the root that may disturb the formation of the LEV. Since the presence of a central body was unavoidable in experiments, the effects due to its presence were assessed in detail using numerical analysis.

First, we modelled the wings with the holders, with offsets $\hat{b}_0 = 0.08$ and 0.25, rotating at $Re_b = 900$. The flow structures on the wings were compared to those from the scanning PIV experiments. Figure 4.7 shows a comparison of the LEV structures in these two cases for the wings rotating at $Re_b = 900$. The LEV structures were identified using isosurfaces of the constant Q criterion ($Q^* = 10$). In this figure, The dual-LEVs in CFD can be seen to be qualitatively similar to those from PIV, with a difference of the data close to the wing tip and the wing root. These small differences are seen because the data could not be obtained near the wing root and wing tip from PIV due to the shining surfaces. The quantitative comparison of the results from the two methods are shown by comparing the normalised spanwise circulation with the wing rotation, for $\hat{b}_0 = 0.08$, in figure 4.4.

Furthermore, we modelled two sets of geometries: first, with the holders of varying sizes that caused the wing to offset from the rotation axis by an amount b_0; and second, without the holders, but shifting the wing root away from the rotation axis by the same amount as that with the holders.

In all these cases, the wing was rotated with $Re_b = 1000$ The time traces of the lift coefficient for different offsets are compared in figure 4.8(a). The lift coefficient of the wing is similar with and without the holder for the offsets $\hat{b}_0 < 0.5$. When averaged over the final 30° of rotation, the difference between $\bar{C}_L$ acting on the wing with and without the holder is less than 1%. However, for larger offsets, the difference increases. Another striking difference is that the lift coefficient of the wing without the holder remains constant after $t/T \sim 0.5$, whereas the lift coefficient of the wing with the holder keeps reducing with time. This reduction in the lift coefficient with time is greater for larger holders, which indicates that this is caused by an influence of the presence of the holder.

The coefficient of lift exerted on the holder was also monitored separately, as shown in figure 4.8(b). C_L of the holder with $\hat{b}_0 = 0.23$ is negligibly small. When observed during the time $t/T < 0.25$, C_L of the holder increases dramatically with its size. For the holders in the range $\hat{b}_0 \leq 0.98$, post $t/T = 0.6$, C_L reaches a relatively stable value

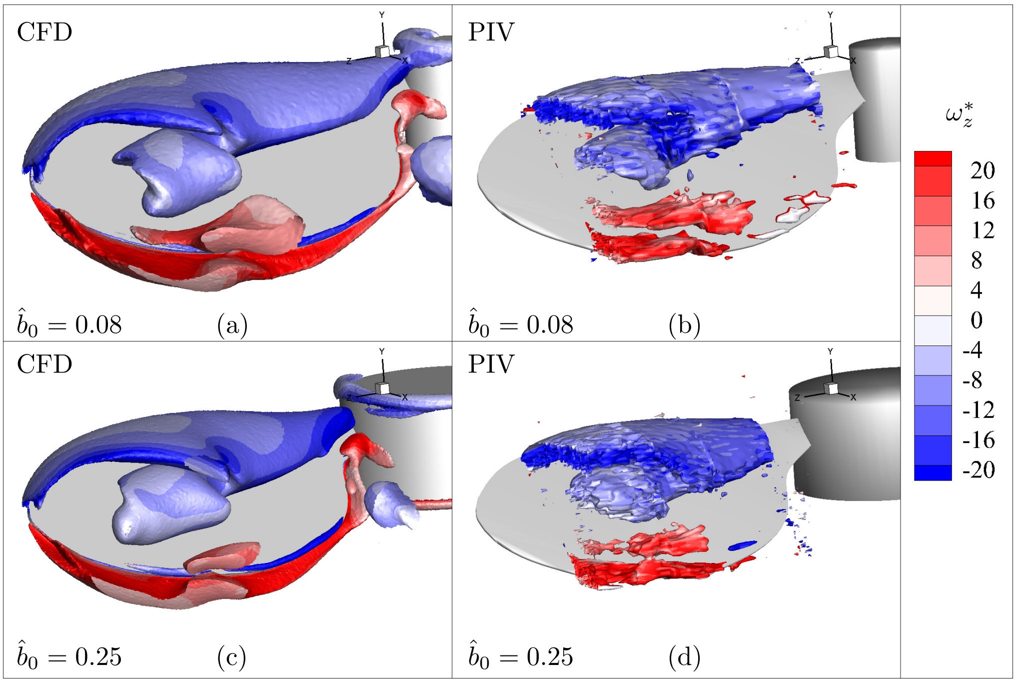

FIGURE 4.7: The figure shows the vortex structures identified using the constant Q-criterion for the wings rotating at $Re_b = 900$, with the holder causing an offset of $\hat{b}_0 = 0.08$ in (a) and (b), and the holder causing an offset of $\hat{b}_0 = 0.25$ in (c) and (d). The flow structures obtained from CFD, in (a) and (c), compare well with the corresponding flow structures obtained with the scanning PIV experiments, in (b) and (d).

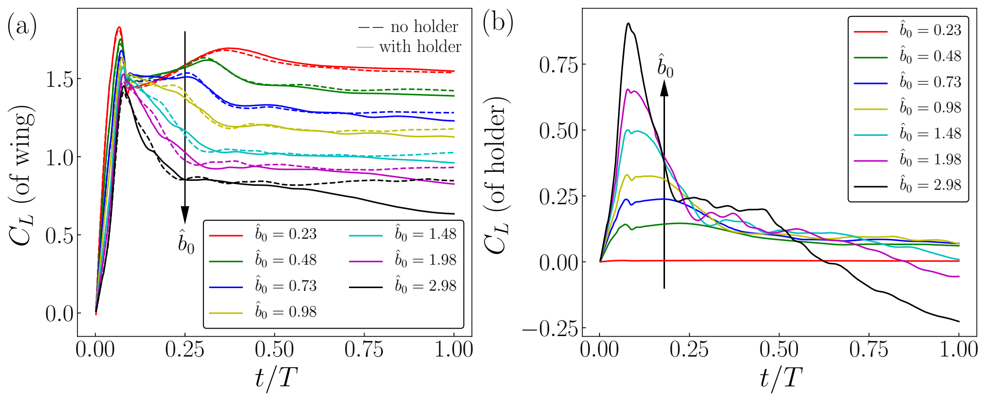

FIGURE 4.8: The time traces of the lift coefficient acting on the wing rotating at $Re_b = 1000$ with and without the holders for different offsets are plotted in (a). In (b), the time traces of the lift coefficient acting on the holders for the same cases show an influence of the holder size on the lift.

close to 0.1. However, for larger holders, C_L reduces continuously with time, without reaching a stable value. This might be on account of the increased secondary flow around the larger holder that continuously interacts with the LEV near the wing root, affecting its suction. This might result in a continuous decay of lift. Therefore, larger holders are observed to have more drop in C_L, which even applies to negative values for $\hat{b}_0 \geq 1.98$. Therefore, the presence of the central body can be assumed to have a negligible influence on the lift force only if its size (in terms of the wing offset equal to its radius) is less than $\hat{b}_0 = 0.5$. This confirms that the secondary flow at the central body wall affects the aerodynamics beyond this size. The effects due to the change in Rossby number caused by the increased wing-root offset were assessed experimentally by observing the 3-D LEV structure, as presented in the following section.

4.6 Effect of offset ratio

The central holder's diameter was varied between 15 and 120 mm keeping the same wing geometry. Hence, the wing root was offset from the axis of rotation,such that the offset ratio varied in the range ($0.063 < \hat{b}_0 < 0.5$). As there is an eight times change in the offset ratio, it was expected to also see a change in the LEV structure. Hence, the flow structure was obtained for different offset ratios, for the wing rotated at different Reynolds numbers ($600 < Re_b < 3000$). First, a comparison of the LEV structures at a chosen Reynolds number was made for different offsets. The 3-d LEV structures were visualised by observing the isosurfaces of the normalised $\gamma_2 = 2/\pi$ using the data obtained from the scanning PIV.

Figures 4.9(a)-(f) show a comparison of the LEV structures for the wing rotating at $Re_b = 1000$ with different holders. A large secondary LEV was observed to split from the primary LEV. However, the difference between the LEV structures did not seem significant for offsets $\hat{b}_0 \leq 0.25$. In figure 4.9(g)-(l), the normalised vorticity contours are plotted on different spanwise planes, which show that the LEV split occurred at a similar r/b location for $\hat{b}_0 \leq 0.25$. By comparing the vorticity contours on the spanwise planes at $r/b = 0.6$ for different offsets, it can be observed that the secondary vortex after the split becomes weaker as the offset is increased. This reduction in the strength is evident from the reduced mean vorticity inside the secondary LEV with an increase in the offset, as shown in figure 4.9.

It can be seen in figures 4.9(g)-(l) that, for lower b_0/b values, the regions near

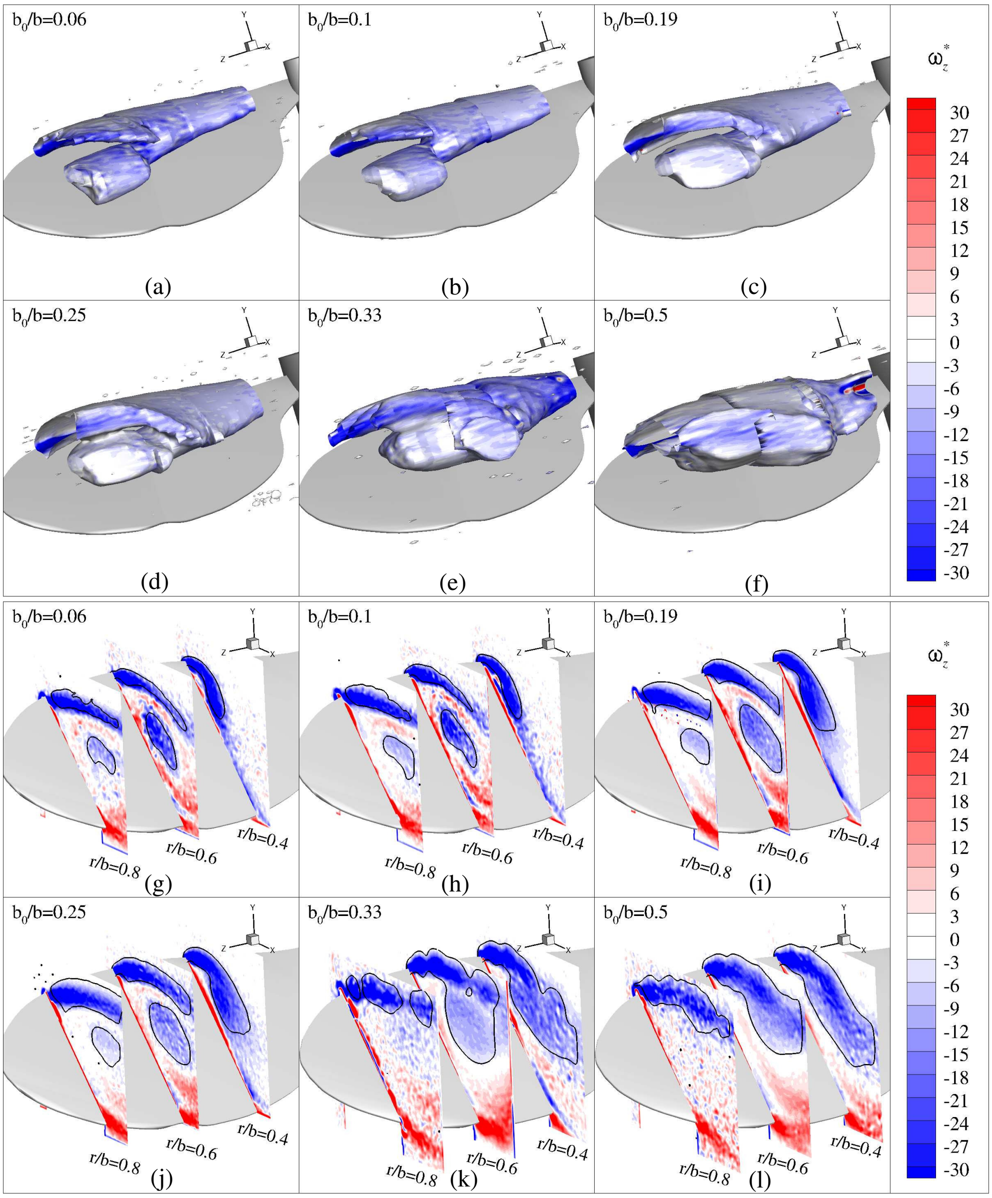

FIGURE 4.9: For the wing rotating at $Re_b = 1000$, the LEV structures for different offsets are obtained from the isosurfaces of $\gamma_2 = 2/\pi$ from the PIV data at various spanwise locations, shown in subfigures (a)-(f). The isosurfaces are coloured with normalised spanwise vorticity. Subfigures (g)-(l) show the normalised vorticity contours at three spanwise locations ($r/b = 0.4, 0.6$, and 0.8) for different offsets.

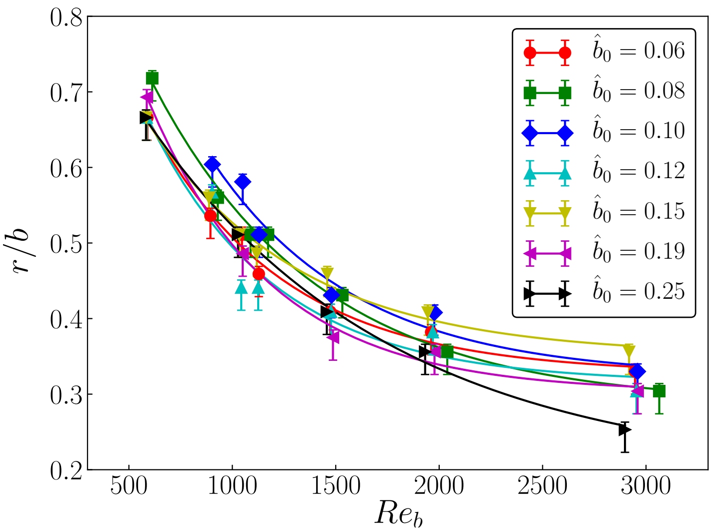

FIGURE 4.10: Although the LEV split position exponentially shifts towards the wing root with Re_b, it remains in a narrow region for any given Re_b, for the offset ratios $\hat{b}_0 \leq 0.25$. The smooth lines represent the exponential fits to the data. The LEV split could not be identified for the offset ratios 0.33 and 0.5.

the LEV centres LEV1 and LEV2 (as shown in figure 4.3) contain relatively larger magnitudes of the negative spanwise vorticity. As described earlier, a small region of positive vorticity induced by the LEV is observed to grow in size with an increase in r/b. At a certain location along the span, this vorticity gets entrained in the LEV structure, forming the dual-LEVs. With an increase in the wing-root offset, the spanwise flow and effects of the Coriolis force are reduced, in line with the reduced streamwise velocity difference between the wing root and tip. The Coriolis force is important for maintaining a compact LEV2 close to the wing surface, as shown by Jardin & David (2015). This change to the LEV structure with offset upstream of the split position is clearly seen in figure 4.9. This leads to a reduction in the boundary-layer secondary vorticity generated at the surface beneath the LEV structure, and hence a reduced tendency for the LEV structure to split. For very large offsets (such as $\hat{b}_0 = 0.33, 0.5$), the secondary LEV remains attached to the primary shear layer and hence, no clear split is observed. The LEV split location was tracked for $\hat{b}_0 \leq 0.25$ to represent the quantitative comparison of the flow characteristics.

Figure 4.10 shows the variation of the LEV split location with Reynolds number for different offsets. It can be seen that regardless of the offset ratio the split locations are close to each other, and only depend on the Reynolds number. The difference in the split locations at a given Reynolds number is within the uncertainty of the experiments. Since the split position is an important feature affecting the LEV structure, the above results show that, for the range of offset ratios $\hat{b}_0 \leq 0.25$, the central body size has a minimal effect on the LEV structure. In addition, it appears that the change to the spanwise flow onto the wing root induced by different holder sizes does not strongly affect the LEV split. However, it may affect the strength of the secondary vortex in terms of the spanwise vorticity. The strength of the secondary vortex for the offsets $\hat{b}_0 = 0.33$ and 0.5 is so low that it does not separate from the primary shear layer.

4.7 Summary

In this study, the effect of the Reynolds number and the central body size on the spanwise position where the LEV splits into dual-LEVs, which is often used as a proxy for overall LEV development, is studied experimentally for the flow over a rotating fruit-fly wing model. The range of offset ratios investigated includes the offset ratios for most insects.

The structure of the LEVs was obtained using a scanning PIV technique. The central body's rotational motion as compared to the stationary body of insects was found to have a negligible effect. Thus, the scanning PIV measurements were conducted with the wing and the central body rotated at span-based Reynolds numbers between 600 and 1500. The fixed-plane PIV measurements were conducted for $2000 < Re_b < 10000$. The dual-LEVs were observed to split at radially inward locations with an increase in the Reynolds number. The comparison of the split locations with those obtained from numerical simulations of an identical wing by Harbig *et al.* (2013) showed good agreement for a small central body size. Further experiments using a wide range of body sizes causing the offset ratios to be $0.06 \leq \hat{b}_0 \leq 0.25$ showed a negligible effect on the LEV split to within experimental uncertainty bounds. However, the larger offset ratios resulted in a significantly different LEV structure with no clear identifiable split. Interestingly, in the lower range of offsets, the values of C_L remained constant past $t/T = 0.5$ due to a stable LEV. However, for larger offsets ($\hat{b}_0 > 0.5$), C_L was observed to decrease continuously with time, suggesting a significant influence of the secondary flow originating near the central body wall.

It is interesting to note that for most insects, the body sizes create offsets in the range $\hat{b}_0 \leq 0.14$. Thus, despite the influence of a central body on the fluid feeding into the LEV and the relative influence of the rotational acceleration to other acceleration components, over this range of body sizes, the change in Reynolds number has a significant influence. However, the wing offset due to the change in the central body diameter was found to have a minimal effect in the normal insect range of offset ratios.

Chapter 5

Effects of Aspect Ratio, Reynolds Number and Rossby Number

5.1 Introduction

The complex aerodynamics of insect wings have been investigated by many researchers in the past and it has been established that the stable attachment of the vortex formed at the leading edge, known as the leading-edge vortex (LEV), plays a key role in achieving a stable flight (Maxworthy, 1979; Ellington *et al.*, 1996). The wing aspect ratio ($\mathcal{R}$), Reynolds number (Re) and Rossby number (Ro) are among the important parameters that can influence the LEV formation and its stability. Two independent studies, by Harbig *et al.* (2013) and Lee *et al.* (2016), have shown that the effects of any two of these parameters are coupled.

The most important geometrical parameter affecting the flapping and rotating wing aerodynamics is $\mathcal{R}$, defined as the ratio of the wing-span (b) to the mean wing-chord (c). The influence of $\mathcal{R}$ on the lift and drag forces has been a topic of debate for a long time, as discussed in chapter 2. Lee *et al.* (2016) pointed out that the $\mathcal{R}$ studies in the past did not preserve Ro, which would have resulted in a coupled effect of $\mathcal{R}$ and Ro. Here, the Rossby number has been defined as $Ro = R_g/c$, where R_g is the radius of gyration of the wing. However, all the simulations in the study by Lee *et al.* (2016) were conducted at $Re = 500$, which showed that for a given Ro, C_L could be maximised by increasing $\mathcal{R}$. On the contrary, at such Reynolds numbers in nature, only low-$\mathcal{R}$ wings are observed. Therefore, even though the $\mathcal{R} - Ro$ coupling explains the discrepancies in most of the past studies, it may not provide a satisfactory explanation of why certain aspect-ratio wings are observed only at certain Reynolds numbers in nature. Moreover, it is important to revisit the chord-based definition of the Rossby number since the wing-span has been shown to be the more relevant length-scale of the LEV structure (Harbig *et al.*, 2013).

Hence, in view of the recent understanding of the LEV structure and the associated length scales, the present computational study investigates the effects of $\AE$, Re and Ro simultaneously on a rotating wing by systematically varying each of these parameters. Harbig *et al.* (2013) have decoupled the effects of $\AE$ and Re by using the span-based Reynolds number for the wings with a zero wing-root offset. Since the scope of the present study extends to the wings with varying wing-root offsets, it is necessary to verify the use of the span-based scaling of Re for wings of different $\AE$ with an offset. In the present study, the use of span-based Reynolds number (Re_b) is shown to decouple the effects of $\AE$ on the flow structure, even for wings with an offset, $\hat{b}_0 = 0.16$. The reasons behind the influence of $\AE$ on the aerodynamic forces are investigated in detail. Furthermore, the span-based scaling is extended to Rossby number by revisiting the normalising terms of accelerations in the Navier-Stokes equations. The modified scaling decouples the effects of $\AE$ and Ro.

5.2 Span-based Reynolds number scaling

As discussed in chapter 2, Harbig *et al.* (2013) have proposed the use of a span-based Reynolds number in order to decouple Reynolds number and $\AE$ effects. They observed very similar LEV flow structures over wings of different aspect ratios rotating at a constant Re_b. However, in their numerical models, the wing-root offset was zero. Since the root offset, or the petiolation, can also influence the flow structure, in this study the flow structures for wings of different aspect ratios, and with a non-zero normalised wing-root offset of $\hat{b}_0 = 0.16$, have been investigated.

Wings of aspect ratios $1.8, 2.91, 5.1$, and 7.28, with a central body giving a wing-root offset of $\hat{b}_0 = 0.16$, were rotated at different Reynolds numbers in the range $300 \leq Re_b \leq 10\,000$. Note that this extends the aspect ratio range of that studied by Harbig *et al.* (2013), by including the case of $\AE = 1.8$. First, the flow structures at Reynolds numbers $Re_b = 300$ and $Re_b = 4000$ were compared for different aspect ratios. In all the cases, the LEV was observed to form and increase in size from the wing-root to the wing-tip. The LEV was identified using the Q-criterion (Hunt *et al.*, 1988), which is defined as

$$Q^* = Qb^2/U_g^2 = \frac{1}{2}[\Omega_{ij}\Omega_{ij} - S_{ij}S_{ij}] = \frac{1}{2}[||\boldsymbol{\Omega}||^2 - ||\boldsymbol{S}||^2], \tag{5.1}$$

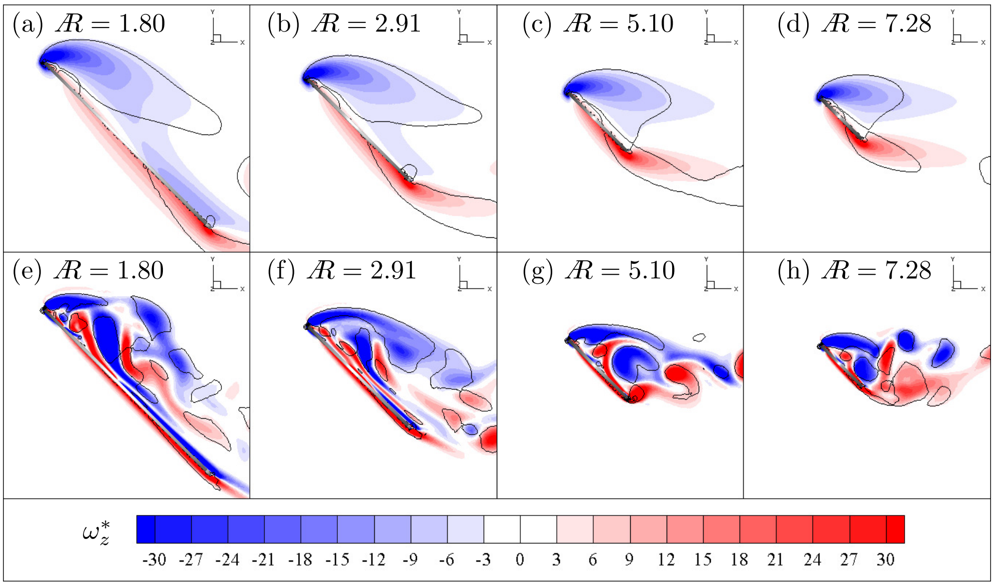

FIGURE 5.1: The normalised spanwise vorticity (ω_z^*) contours are shown at the spanwise location $r/b = 0.4$ for different aspect ratio wings rotating at $Re_b = 300$ in (a–d) and at $Re_b = 4000$ in (e–h). The black solid lines represent the vortices identified by the constant Q-criterion. The rotation angle in all the cases is $\phi = 270°$.

where Ω_{ij} and S_{ij} are, respectively, the asymmetric and symmetric components of the velocity gradient tensor. $Q^* > 0$ represents the region dominated by the rotational strain $||\mathbf{\Omega}||^2$. Figure 5.1 shows the normalised spanwise vorticity (ω_z^*) contours on the spanwise plane located at $r/b = 0.4$. The vortices are represented by the isocontours of $Q^* = 0$ shown by solid black lines. It can be seen that at $Re_b = 300$, there is a single LEV with relatively lower vorticity. However, at $Re_b = 4000$, the LEV is relatively stronger with a higher ω_z^* due to an increased swirl and it is split to form dual-LEVs. It should be noted that the flow structure for all aspect ratios is similar at a given Re_b, suggesting that the span-based scaling of the Reynolds number is the appropriate scaling that defines the flow structure. This was further confirmed by tracking the LEV split location, which is a prominent flow feature, for all these wings rotating at different Reynolds numbers.

The LEV-split is identified with the help of Graftieaux's vortex core identification algorithm (Graftieaux *et al.*, 2001), as discussed by Harbig *et al.* (2013). The circulation about a grid point P was computed as

$$\gamma_2(P) = \frac{1}{N} \sum \frac{[R_{PM} \wedge (U_M - U_P) \cdot z])}{||R_{PM}|| \cdot ||U_M - U_P||}, \tag{5.2}$$

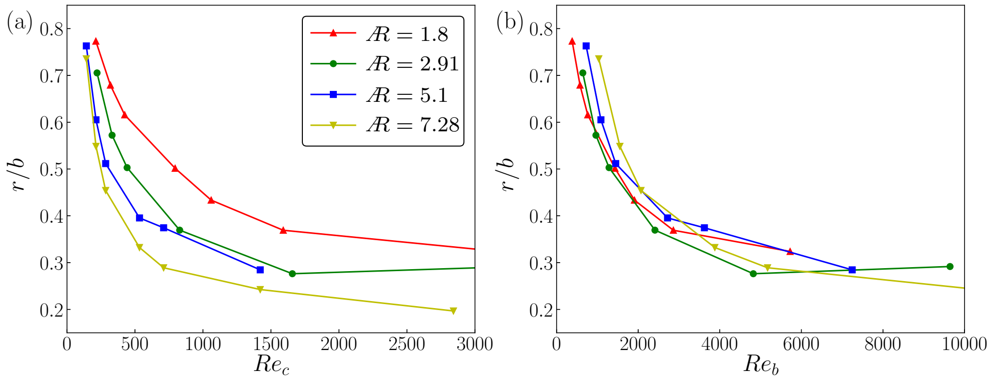

FIGURE 5.2: The curves for the split location as a function of Reynolds number scaled with the wing-chord for different aspect ratios in (a), collapse if the Reynolds number is scaled with the wing span (Re_b) in (b). The normalised wing-root offsets in all the cases were maintained to be $\hat{b}_0 = 0.17$.

where N is the number of grid points, M, inside a bounded square region with P as the centre, R_{PM} is the radius vector and U_{PM} is the velocity vector with respect to P. $|\gamma_2|$ was bounded by unity and calculated on two-dimensional velocity planes along the span, with z being the unit vector normal to the plane. The vortex core was identified by the regions where $|\gamma_2| > 2/\pi$ as being locally dominated by rotation. The circulation inside this region was calculated by integrating the spanwise vorticity. When plotted against the spanwise location, the circulation initially increased and then suddenly dropped to show two circulation values corresponding to the dual-LEVs. This location was referred to as the LEV-split location. The details of this approach can be found in Harbig *et al.* (2013).

As can be seen in figure 5.2, the LEV-split locations for the wings of four different aspect ratios were tracked over a range of Reynolds numbers ($300 < Re_b < 10000$). With an increase in Re_b, the split location for any $A\!\!R$ wing was observed to move towards a lower r/b, i.e. towards an inward location along the span. If plotted against the chord-based Reynolds number (Re_c), the curves of the split location for different aspect ratios are different. The splits at higher $A\!\!R$ at a chosen Re_c occur more towards the root than the lower $A\!\!R$ wings. However, if plotted against the span-based Reynolds number (Re_b), all the four curves appear to collapse onto a single curve with a variation of less than $\sim 5\%$ of the span, suggesting that the LEV-structures at any given Re_b are similar.

Of interest is that the chord-based Reynolds number scaling appears to work better

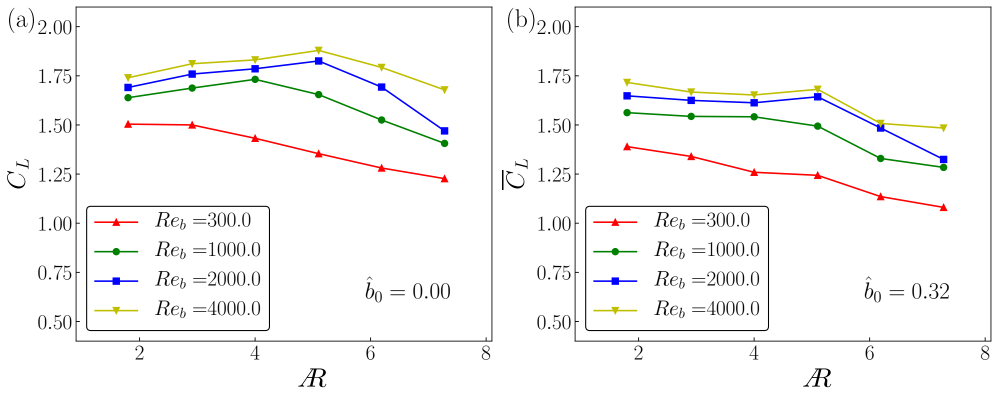

FIGURE 5.3: $\overline{C}_L$ is shown as a function of Æ for four different Reynolds numbers, with no wing-root offset in (a) and with the offset $\hat{b}_0 = 0.32$ in (b).

at smaller Reynolds numbers, as shown by the convergence of the curves in figure 5.2(a) for the lower end of the Reynolds number range. This would seem to be related to the fact that for smaller Reynolds numbers, the cross-sectional size of the LEV structure is relatively much bigger because increased diffusion prevents a tight roll up of the leading-edge separating shear layer. Adding to this is reduced spanwise flow, limiting the advection of vorticity towards the tip. Thus, at small Re_c, because of its larger length scale, the LEV growth during rotation will be more strongly influenced by the size of the chord. Despite this, even at $Re_b = 300$, corresponding to that of an actual fruit fly, figures 5.1(a)–(d) shows that the spanwise scaling still works reasonably well in characterising the LEV structure. Therefore, throughout this study, the span-based Reynolds number is used.

5.3 Effect of Æ and Re_b at different offsets

Since the LEV structure is similar for wings of various aspect ratios rotating at a constant Re_b, the lift acting on them might be expected to be the same. However, according to Harbig *et al.* (2013), the lift coefficient has been found to be influenced by Æ, depending on Re_b. Additionally, the wing-root offset can also influence the mean lift coefficient ($\overline{C}_L$); this offset has been shown to be responsible for the discrepancies in the values of $\overline{C}_L$ reported by various researchers. Thus, in this section, the reasons behind the variation of $\overline{C}_L$ at various Æ values are investigated for two different wing-root offset ratios ($\hat{b}_0 = 0$ and 0.32). Here, the time-mean lift coefficient ($\overline{C}_L$) has been obtained by averaging the instantaneous lift coefficients over the final 30° rotation of the

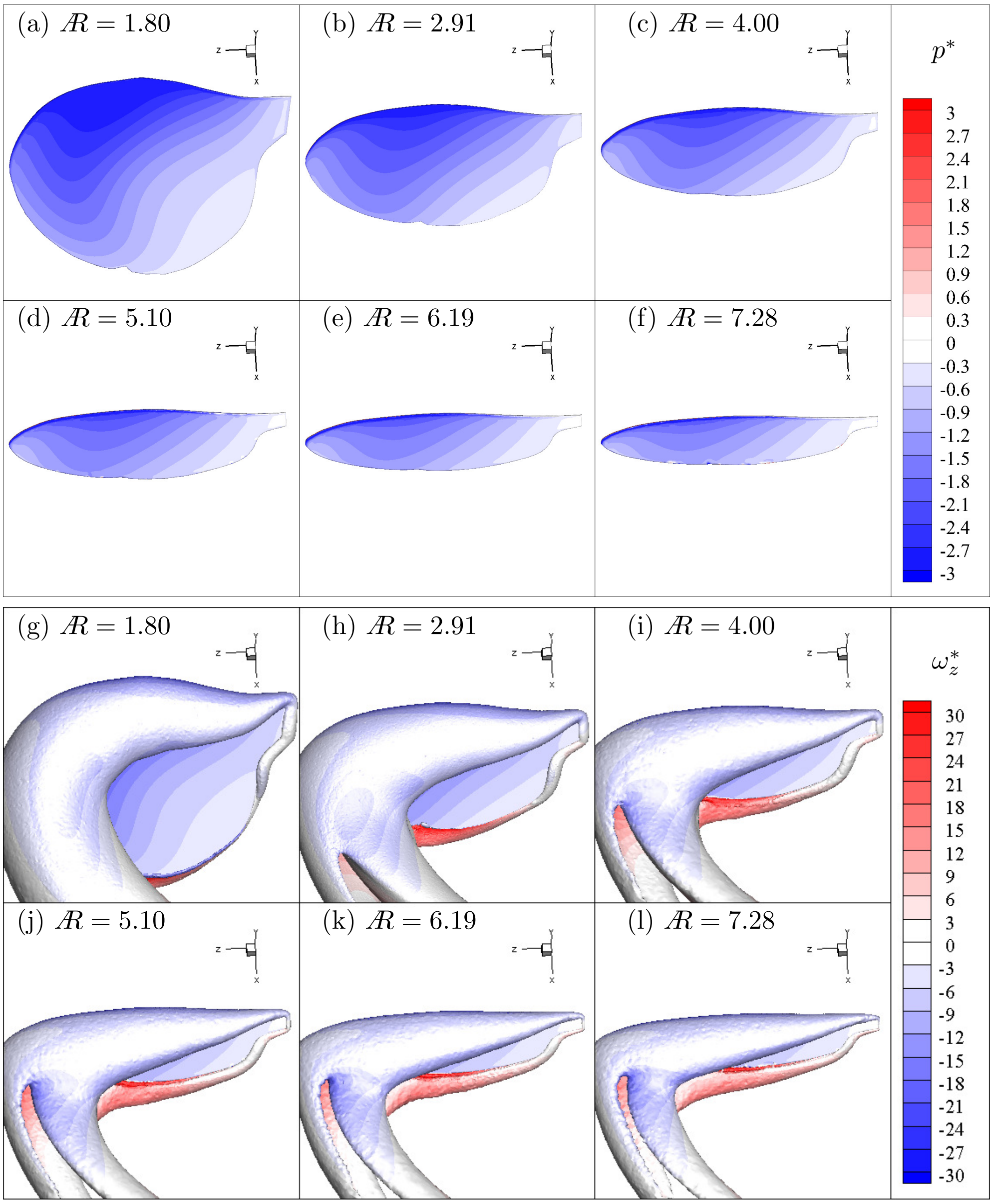

FIGURE 5.4: At $Re_b = 300$, the normalised pressure (p^*) contours on the suction-side surface of the wings of various aspect ratios are shown in (a–f). The LEV is represented using an isosurface of the constant Q-criterion coloured according to ω_z^* in (g–l).

wing, but noting that the variation over that angle is relatively small (see chapter 4).

For zero offset, figure 5.3(a) shows that, for $Re_b = 300$, $\overline{C}_L$ reduces continuously with an increase in $\mathcal{R}$ beyond the value 2.91. However, at a higher Re_b ($Re_b = 1000$), $\overline{C}_L$ increases slightly for $\mathcal{R} \leq 4$ and then decreases for higher $\mathcal{R}$ values. Further, with an increase in Re_b, the peak $\overline{C}_L$ is reached at $\mathcal{R} \simeq 5$. For an offset $\hat{b}_0 = 0.32$, in figure 5.3(b), $\overline{C}_L$ is not observed to increase, but remains relatively stable for the

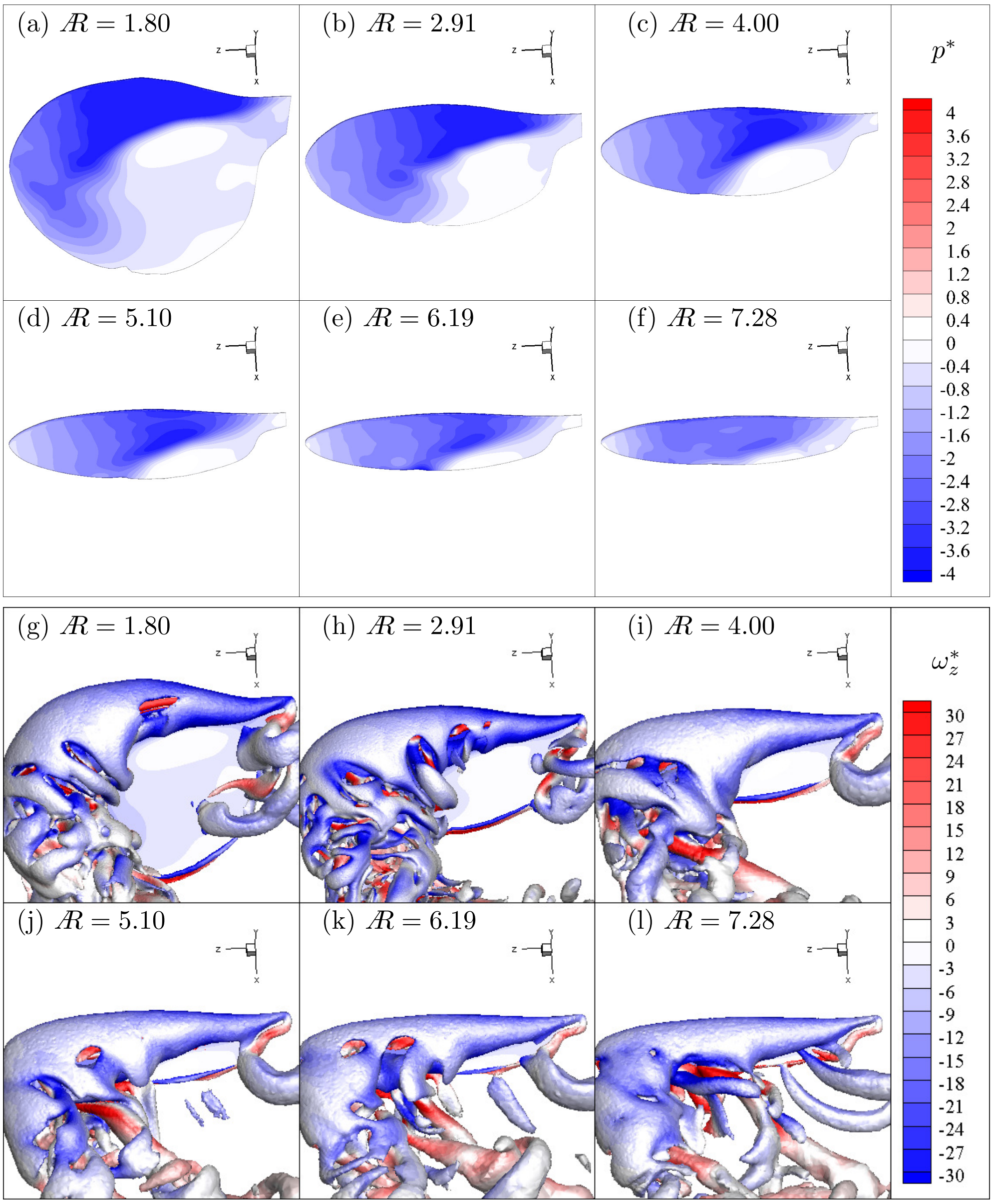

FIGURE 5.5: At $Re_b = 4000$, the negative pressure on the wing's surface on the suction-side is shown to be reducing with Æ in (a–f). The LEV is represented using an isosurface of the constant Q-criterion coloured according to ω_z^* in (g–l).

similar range of Æ values where it was observed to increase in (a). Thus, at lower Reynolds numbers, wings of lower aspect ratios appear to perform better; however, at higher Reynolds number, the wings of low and moderate aspect ratios perform similarly and better than those with higher aspect ratios. It can be inferred from these results that the wings of higher aspect ratios can perform optimally only at higher Reynolds numbers whereas the wings of lower aspect ratios can perform optimally at relatively low as well as higher Reynolds numbers.

The reason behind the different behaviours at low and high Reynolds numbers was further investigated. Figures 5.4(a–f) show the pressures on the wing-surfaces of different aspect ratios rotating at $Re_b = 300$. In all the cases, the highest magnitude of suction is present under the area covered with the LEV, as can be seen in figures 5.4(g–l). The magnitude of suction, identified by the negative pressure on the wing surface, is observed to reduce with an increase in $\mathcal{R}$, perhaps due to a lower area available to redistribute the pressure on the wing surface. It is important to note that the vortex breakdown has occurred after the LEV and the trailing edge vortex (TEV) have merged with the tip vortex (TV) and turned into the wake. Moreover, the stagnation point, identified by zero relative pressure, is always outside the wing surface. The continuous reduction in the magnitude of suction resulted in a reduction in the lift coefficient.

The magnitude of suction is relatively higher at a higher Re_b, as can be seen in figures 5.5(a–f). At this Re_b of 4000, the vorticity is transported at a higher rate through the LEV core, causing it to reduce in size compared to that at the lower Re_b. It can be noted from figures 5.5(g–l) that, unlike the low Re_b flow, the vortex breakdown occurs at a spanwise location before the LEV merges with the tip vortex. As per Shyy & Liu (2007), the vortex breakdown occurs at high Re_b due to a weaker swirling flow. The stagnation point is observed to be on the wing surface near the location of the vortex breakdown, past which the LEV connects to the tip vortex, creating a trail of small unstable vortices in the wake. With an increase in the aspect ratio, the trailing edge is observed to move closer to the stagnation point. For $\mathcal{R} > 5.1$, the stagnation point moves away from the wing surface, accompanied by a drop in the lift.

Thus, purely based on the lift performance in rotation, the optimal wing aspect ratio at $Re_b = 300$ is 2.91, which interestingly is the same as a real fruit fly wing flapping at the Reynolds number in the similar range. As Re_b increases, the optimal aspect ratio also increases. However, the aspect ratios lower than the optimal one have a lift performance that is not very different from that of the optimal wing. Hence, the low-$\mathcal{R}$ wings perform better over a wide range of Reynolds numbers whereas the high-$\mathcal{R}$ wings perform better only at high Reynolds numbers. Interestingly, even in nature, the low aspect-ratio wings are found in insects flying over a wide range of Reynolds numbers. For example, the fruit fly *Drosophila melanogaster* and the beetles *Cerambycid species* and *Melolontha vulgaris* fly at the approximate Re_b values of 350, 5000, and 13000,

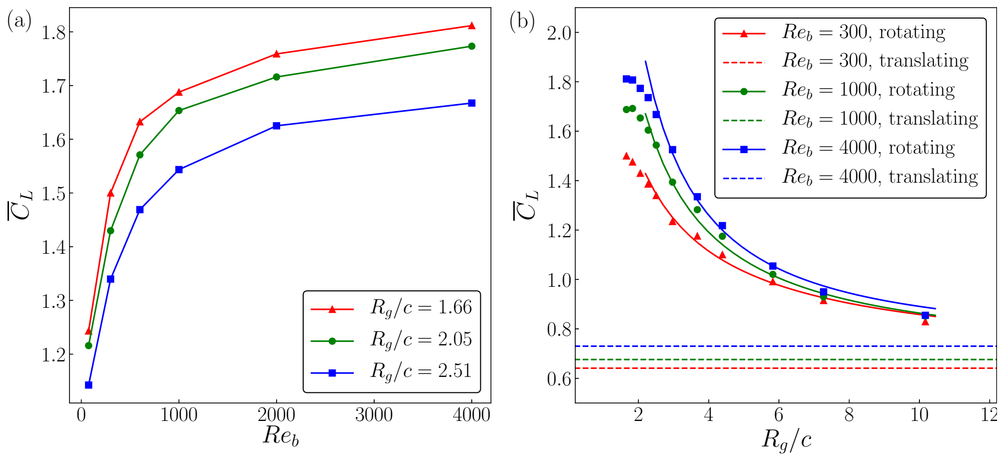

FIGURE 5.6: The variation of $\overline{C}_L$ with Re_b is shown in (a) for the wing of $\mathcal{R} = 2.91$ with three different offsets changing its Rossby number as $R_g/c = 1.66, 2.05$, and 2.51. The variation of $\overline{C}_L$ with R_g/c is shown in (b) for the Reynolds numbers $Re_b = 300, 1000$, and 4000. Here, the dashed lines represent the value for the purely translating wing at these Reynolds numbers.

respectively, and have wing aspect ratios close to 3 (Weis-Fogh, 1973). However, the high aspect ratios ($\mathcal{R} > 5$) can be found only in the insects that fly at high Re_b ($> 10^3$), such as the crane fly (*Tipula paludosa*, $\mathcal{R} = 5.5$, $Re_b \sim 3000$) and the common hawker (*Aeshna juncea*, $\mathcal{R} = 5.6$, $Re_b \sim 10000$) (Ellington, 1984a).

5.4 Effect of Re_b and Ro_b

In past studies, the lift on a rotating wing has been observed to be dependent on the Reynolds number. However, it should also be noted that the lift also depends on the wing-root offset, which essentially changes the Rossby number. This is shown by comparing the variation of $\overline{C}_L$ over a range of Reynolds numbers $75 \leq Re_b \leq 4000$ between three different wing-offsets $\hat{b}_0 = 0, 0.08$, and 0.16, such that the corresponding Rossby numbers were $R_g/c = 1.66, 2.05$, and 2.51, respectively. First, the wing with $R_g/c = 1.66$ was rotated about its rotation axis and the time-trace of C_L was obtained in a way similar to that described in chapter 3. Since C_L remains constant past $t/T = 0.3$, the mean lift coefficient $\overline{C}_L$ was obtained by averaging C_L over the last 30° of rotation, which corresponds to the normalised time $0.66 \leq t/T \leq 0.75$. $\overline{C}_L$ was observed to increase with Re_b due to an increased suction created by the increasingly compact LEV core, as shown in a later section. However, at higher Reynolds numbers, the reduction in viscosity becomes less important, with LEV bursting limiting the contribution of the

LEV.

As can be seen in figure 5.6(a), at a low Re_b, there is a relatively larger increase in $\overline{C}_L$ for the same increase in Reynolds number compared to that at a higher Re_b. The figure also indicates that the lift coefficient is dependent on Rossby number, which was varied by changing the wing-offset. With an increase in R_g/c, caused by increasing offset, the values of $\overline{C}_L$ decrease, which shifts the $\overline{C}_L - Re_b$ curves downwards. Extending these results, the Rossby number was varied over a wider range ($1.66 \leq R_g/c \leq 10.1$) and the variation of $\overline{C}_L$ was obtained, as shown in figure 5.6(b). $\overline{C}_L$ decreased with an increase in R_g/c and approached the value for the translating wing. This trend is in line with the variation of lift coefficient demonstrated by Tudball Smith *et al.* (2017) and Lee *et al.* (2016).

It is important to note that the ratio R_g/c can be varied in two ways; first, by varying the offset, thereby changing R_g and second, by varying the aspect ratio, thereby changing c (for a constant wing span). In most Rossby number studies, R_g/c is called the Rossby number. Since the wing span was found to be the more relevant parameter to define the flow structure, the use of R_g/c was revisited in this context. The scaling of the Navier-Stokes equations is revisited as shown in appendix A. Using an approach similar to Lentink & Dickinson (2009a), the length scale for the acceleration terms is taken as the wing span. The revised scaling shows that for a rotating wing, the centripetal and Coriolis accelerations scale with R_g/b.

The difference between using the ratios R_g/c and R_g/b for Rossby number was clear after observing the flow structures over the wings of various aspect ratios. First, the wings of $\mathcal{R} = 2.91, 5.1$, and 7.28 were rotated at $Re_b = 300$. The wings of smaller aspect ratios have a relatively larger chord (for a constant wing span). Hence, to maintain a constant R_g/c, the values of R_g for the wings of smaller aspect ratios were increased by moving their wing roots away from the axis of rotation. The LEV structures for various wings with a constant R_g/c are compared in figure 5.7(a–c) in the order of reducing $\mathcal{R}$. It can be seen that for $\mathcal{R} = 7.28$, the vorticity is transported through the LEV in the spanwise direction towards the wing tip. A vortex trail is left in the wake after the LEV merges with the tip vortex and tilts. However, with a reduction in $\mathcal{R}$, the spanwise transport of vorticity gradually decreases. This is due to the incremental increase in the wing-root offset that creates a reduction in the Coriolis effects, which are important to maintain the LEV structure intact (Jardin, 2017). However, if the ratio R_g/b is

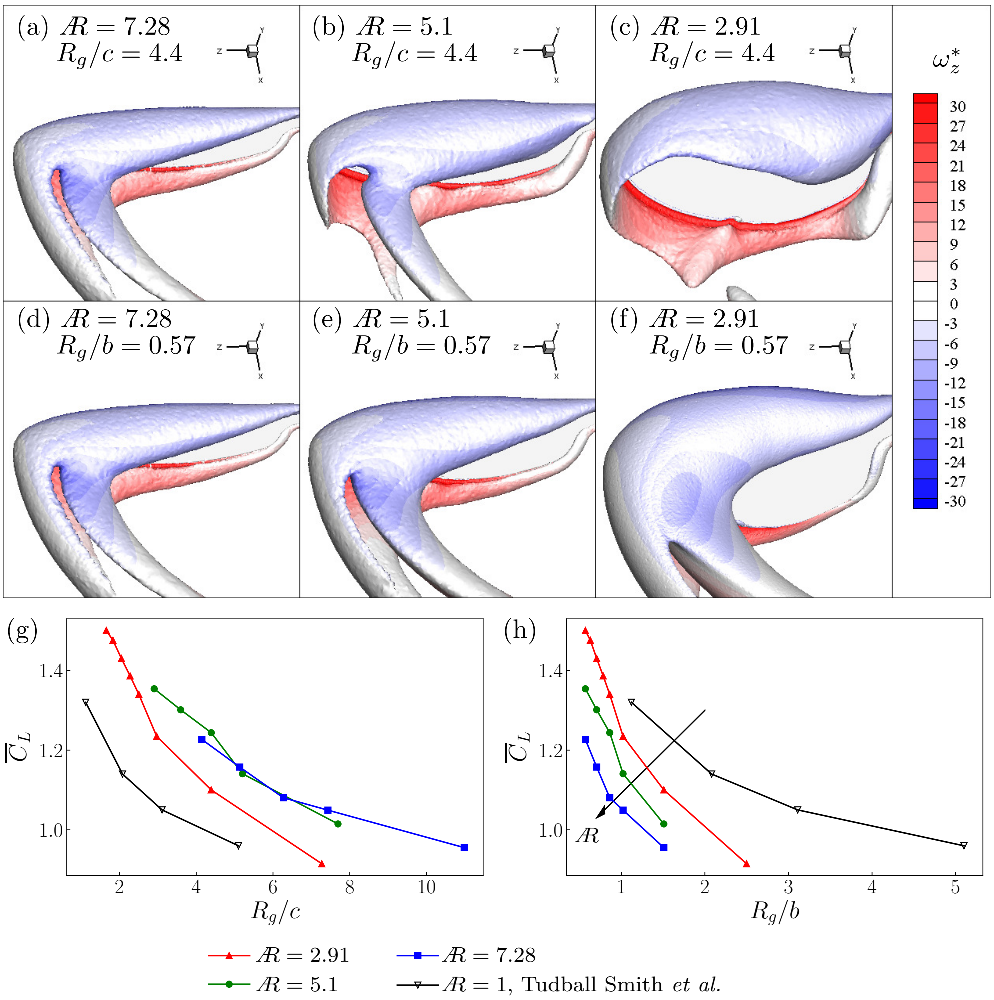

FIGURE 5.7: The LEV structures, identified by Q-criterion, for wings of $AR = 7.28, 5.1$, and 2.91 at a constant R_g/c rotating at $Re_b = 300$ are shown in (a–c). The LEV structures for the same wings at $Re_b = 300$, but with a constant R_g/b are shown in (d–f). The isosurfaces are coloured according to ω_z^*. The variation of $\overline{C}_L$ with R_g/c, in (g), and with R_g/b, in (h), is shown for the wings of various AR rotating at $Re_b = 300$. The data by Tudball Smith *et al.* (2017) are for the wing rotating at $Re_b = 350$.

maintained to be constant, the wing-root offset in all the wings is the same, resulting in similar Coriolis effects across all aspect ratios. Therefore, the LEV structure in the constant R_g/b cases is similar, as shown in figures 5.7(d–f). This suggests that the ratio R_g/b is a better choice to characterise the flow structure and resultant aerodynamics.

Moreover, when the variation of $\overline{C}_L$ with R_g/b is obtained for various aspect ratios, the comparison shows a monotonic decrease in $\overline{C}_L$ with AR, as can be seen in figure 5.7(h), unlike that in (g). This decrease in $\overline{C}_L$ with an increase in AR at $Re_b = 300$ is due to the decrease in the magnitude of suction pressure, as explained earlier in § 5.3.

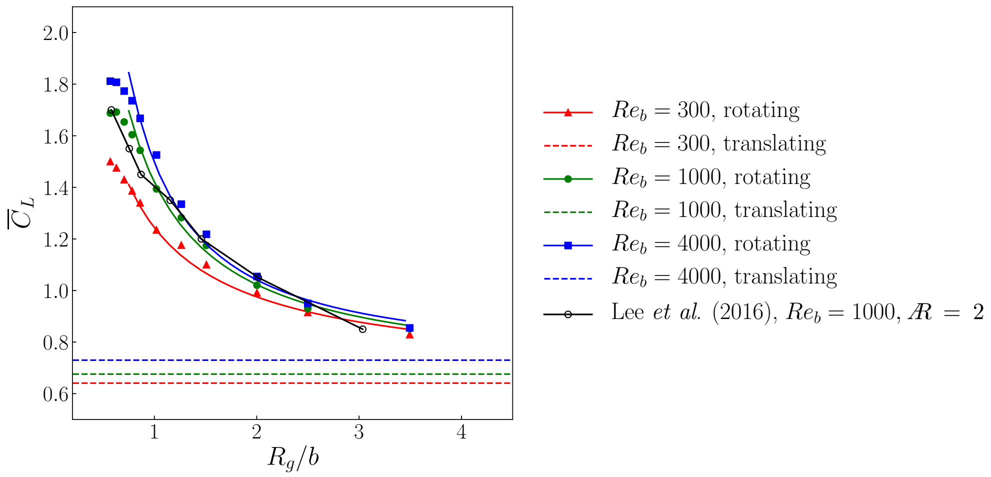

FIGURE 5.8: The variation of $\overline{C}_L$ with R_g/b is plotted for Reynolds numbers $Re_b = 300, 1000,$ and 4000 for the wing of $AR = 2.91$. The dashed lines represent the limit approached by the curves as $R_g/b \to \infty$ (purely translating wing) at the respective Re_b values. The data extracted from Lee *et al.* (2016) have been added for comparison.

Thus, the revised definition of the Rossby number that follows the span-based scaling is

$$Ro_b = R_g/b. \tag{5.3}$$

Following this definition, the curves from figure 5.6(b) are scaled as a function of R_g/b, as can be seen in figure 5.8. The data for a wing with $AR = 2$ rotating at $Re_b = 1000$ have been extracted by interpolation from the contour map by Lee *et al.* (2016). The curve obtained from their data compares well with that from the present study for the same Reynolds number. This is also consistent with the fact that, at $Re_b = 1000$, there is an insignificant change in $\overline{C}_L$ in the range $AR < 4$ (see figure 5.3). In all the cases, there is a decrease in $\overline{C}_L$ with an increase in Ro_b, which is investigated further.

The lift force on the wing is due to the difference in the pressures on the pressure-side and the suction-side. Hence, for the range $Ro_b \leq 1.02$, where the lift coefficient drops drastically, a comparison of pressures is shown in figure 5.9. The Reynolds number in all these cases was 1000. It can be clearly seen that the pressure distribution on the wing suction side changes dramatically with Ro_b. There is a relatively smaller change observed on the pressure-side. At a low Ro_b, the suction-side surface has a greater magnitude of negative pressure creating a higher suction contributing to the overall

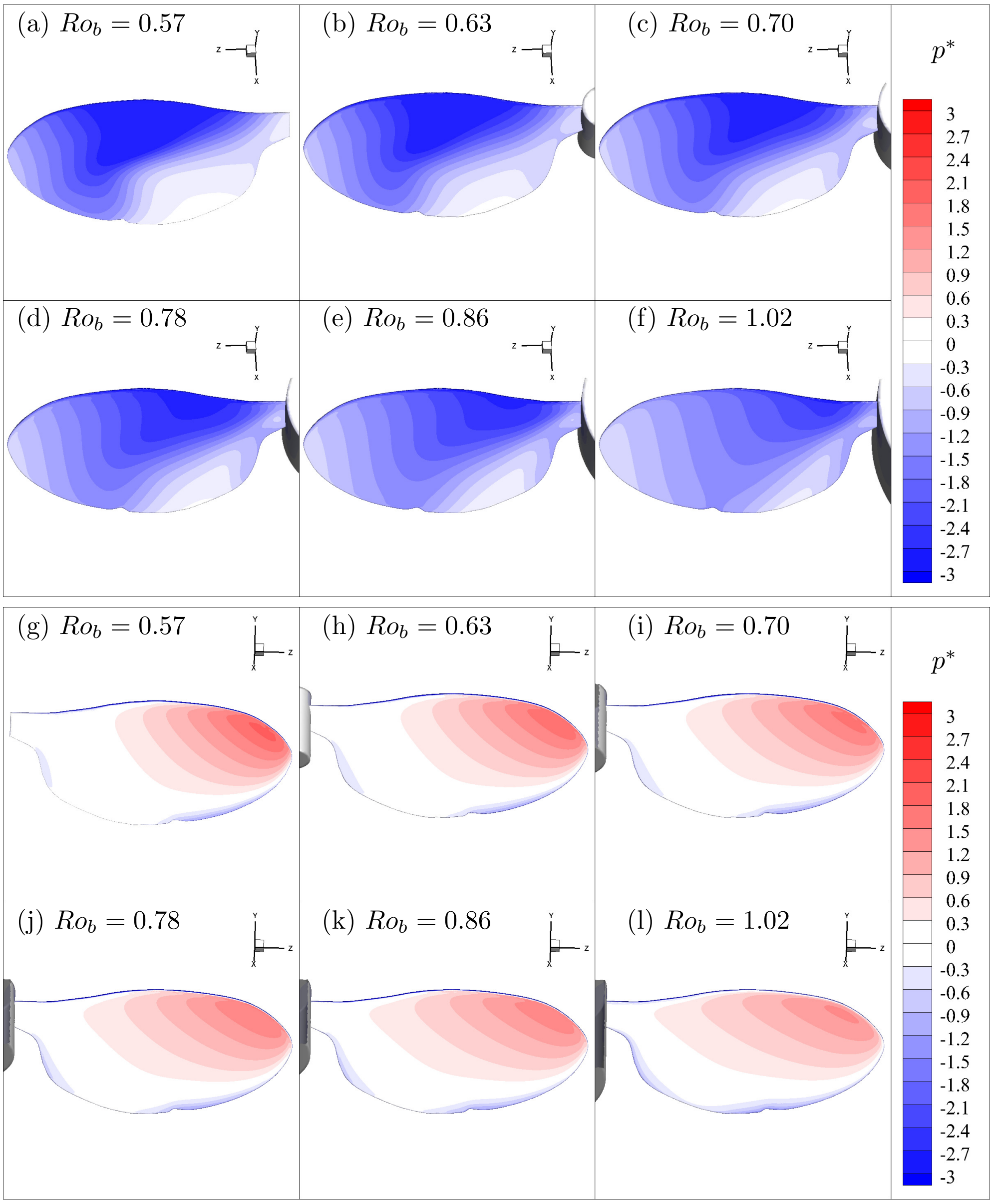

FIGURE 5.9: At $Re_b = 1000$, the comparison of normalised pressures on the suction-side surfaces are shown in (a–f) and those on the pressure-side surfaces are shown in (g–l) for different values of Ro_b.

lift. As the Rossby number is increased, the magnitude of the suction pressure on the wing surface reduces, thereby, reducing the lift. It should be noted that the presence of the central body in this range of Ro_b has a negligible impact on the lift since the corresponding offset ratios are in the range $\hat{b}_0 < 0.5$.

A detailed investigation is conducted by observing the flow structures. In figures 5.10(a–f), the LEV is shown using a semitransparent isosurface of the 3D Q-

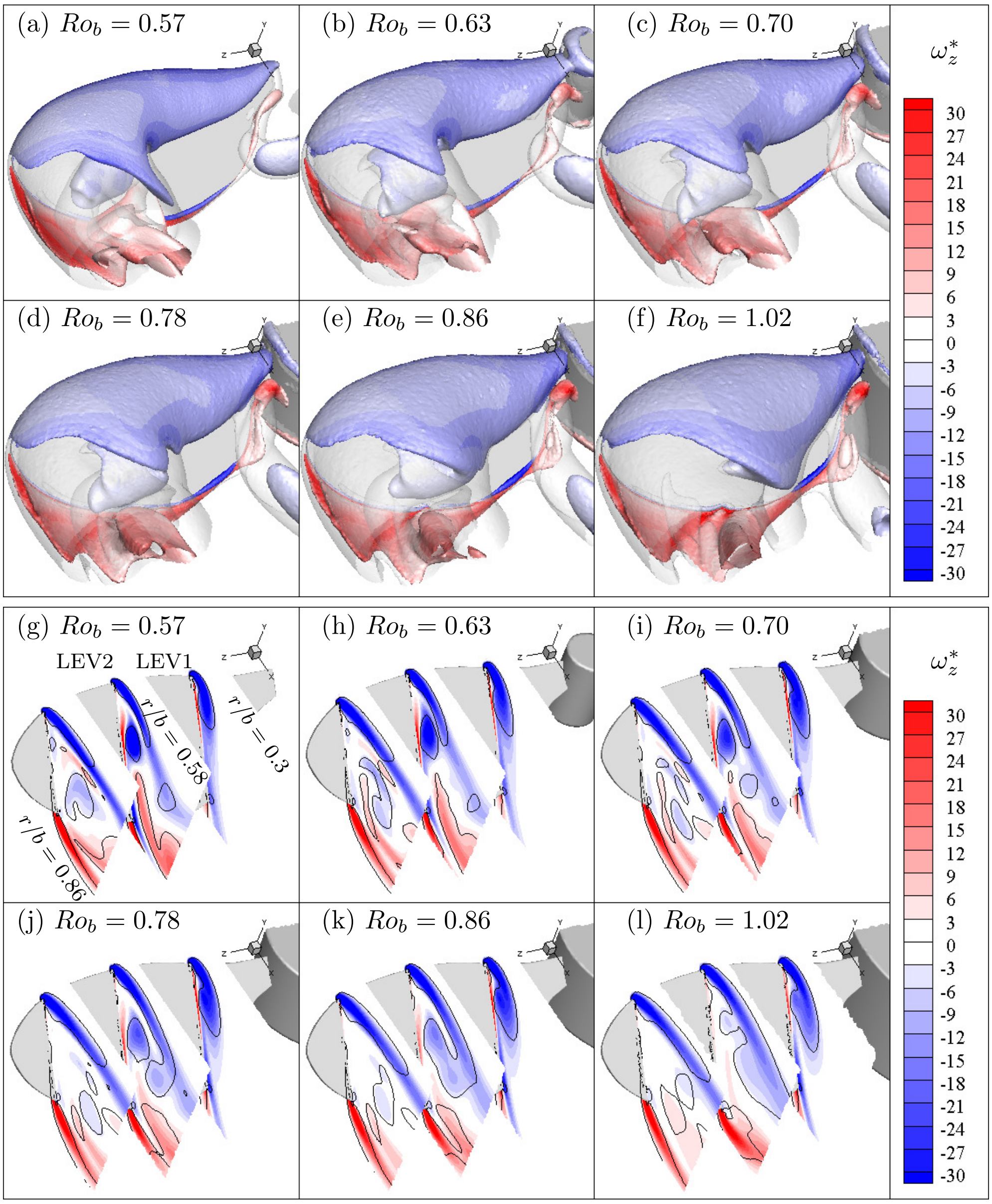

FIGURE 5.10: In figures [a-f], the LEVs for different Ro_b are represented using the semitransparent isosurfaces of the 3D Q-criterion. Additionally, the isosurfaces of the 2D Q-criterion coloured with the normalised vorticity are shown to highlight the secondary vortex features. The normalised spanwise vorticity contours at the locations $r/b = 0.3, 0.58$, and 0.86 for all the cases are shown in (g–l). Here, the black lines represent the isocontours of the 2D Q-criterion.

criterion. The secondary vortex features inside the LEV are highlighted using the isosurface of the 2D Q-criterion. The presence of the dual-LEV structure is evident in all the cases. The primary shear layer separated from the leading-edge and formed the vortex, LEV1. The secondary vortex that split from LEV1 near the mid-chord location formed the vortex, LEV2, as can be seen in figure 5.10(g). It is important to note that with an increase in Ro_b, the primary shear layer spreads over a larger area, which is accompanied by a decrease in strength of the secondary vortex. This variation of the vortex strength in terms of its vorticity can be seen more clearly in figures 5.10(g–l), where the spanwise vorticity contours are shown at three different spanwise locations for each case. In the range $0 \leq Ro_b \leq 0.78$, both the primary and secondary vortices are clear and distinct. The primary shear layers elongate more for $Ro_b \geq 0.78$ and the secondary vortex loses its strength and merges with the primary shear layer. Thus, it is important to note that the LEV-structure changes dramatically with an increase in Ro_b. The decrease in its strength must be responsible for the decreasing suction on the wing.

When observed across various spanwise planes, the normalised spanwise circulation around the LEV (Γ_z^*) increases, initially, with r/b, followed by a sudden drop when the LEV split occurs, as can be seen in figure 5.11(a). Here, two different curves can be seen, which refer to LEV1 and LEV2. For $Ro_b = 1.02$, only one curve is observed since the LEV did not split. Overall, there is an increase in the circulation at any given r/b, with an increase in Ro_b. Therefore, the LEV circulatory lift computed by integrating the spanwise circulation is also observed to be increasing with Ro_b, as can be seen figure 5.11(b). This also matches with the trends predicted from PIV images, such as those by Phillips *et al.* (2017). However, the overall $\overline{C}_L$ computed directly from the forces acting on the wing is observed to be reducing with Ro_b. Therefore, the LEV circulatory lift coefficient does not appear to be a true representative of the overall $\overline{C}_L$.

The spanwise variation of the mean spanwise velocity inside the LEV ($\overline{u}_z/U_g$) was also tracked across various Ro_b, as shown in figure 5.11(c). In all the cases, the spanwise velocity initially increased, followed by a gradual decrease along $r/b > 0.2$. Overall, $\overline{u}_z/U_g$ decreased with an increase in Ro_b, which resulted in a decreased spanwise vorticity flux, denoted by the term $\overline{u_z\omega_z}b/U_g^2$, as can be seen in figure 5.11(d). This reduction in the spanwise velocity may have been induced by the reduced streamwise velocity gradient, as described by the schematic and plot in figure 5.11 (e) and (f), respectively.

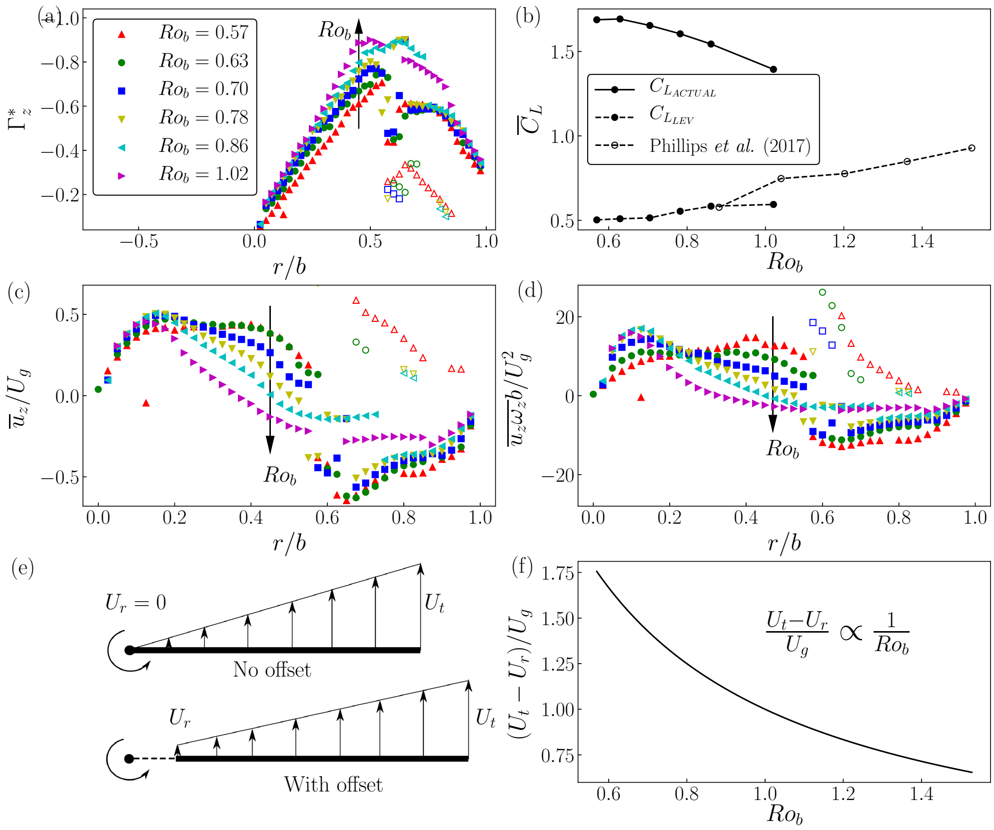

FIGURE 5.11: The spanwise variation of the normalised spanwise circulation (Γ_z^*), mean normalised spanwise velocity ($\overline{u}_z/U_g$), and mean normalised spanwise vorticity flux ($\overline{u_z\omega_z}b/U_g^2$) of the LEV for different Rossby numbers are shown is (a), (c), and (d) respectively. Here, the filled circles represent the values for LEV1 and open circles represent those for LEV2. The LEV circulatory lift coefficients obtained from Γ_z^* and the actual $\overline{C}_L$ for various Ro_b are shown in (b). The change in the root velocity (U_r), tip velocity (U_t), and the velocity gradient, with a change in Ro_b, are shown by the schematic and line plot in (e) and (f), respectively.

With an increase in the wing-root offset, the relative velocity gradient between the tip velocity (U_t) and root velocity (U_r) decreases by an inverse proportion, which will induce a lower spanwise flow. It can be noted that, after the split, there is a higher spanwise velocity through LEV2, whereas there is a negative spanwise velocity through LEV1. This is due to the tilting of LEV in the wake and shifting of the peak negative spanwise pressure gradient towards the trailing edge, as discussed below.

The footprints of the decreased LEV-strength can be observed in the spanwise pressure gradient on the wing's surface, as shown in figures 5.12(a–f). Here, the normalised spanwise pressure gradient is calculated as $(\partial p/\partial z)^* = (\partial p/\partial z) \times b/(0.5\rho U_g^2)$. The loca-

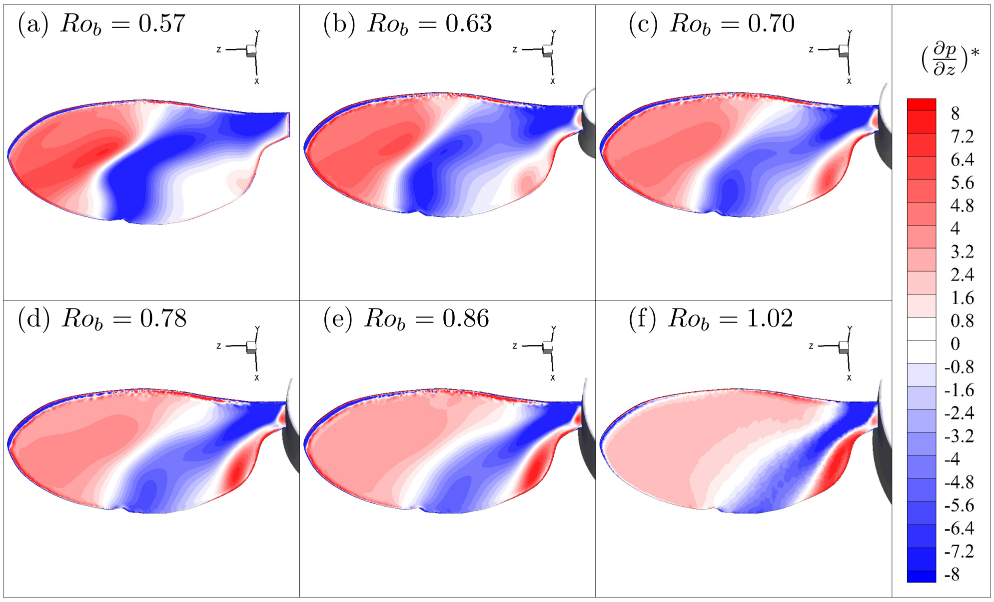

FIGURE 5.12: The normalised spanwise pressure gradients, $(\partial p/\partial z)^*$, on the wing suction side are compared for different values of Ro_b in (a–f).

tion of the zero pressure gradient near the mid-span region indicates the location where the LEV changes its direction and turns into the wake. For lower Ro_b, a more negative pressure gradient is present near the midspan region, which allows a stronger transport of the fluid in the spanwise direction. Therefore, at lower Ro_b, the LEV is narrower and stronger at the core, where the peak spanwise velocity is along the core of LEV2. With an increase in Ro_b, the region of the negative pressure gradient shrinks towards the wing root. Therefore, the weakening of the LEV is accompanied by a reduced spanwise flow.

Hence, it can be concluded that the lift coefficient of the wing is a strong function of the Rossby number in terms of the spanwise scaling, related by an inverse proportion. The lift coefficient at a very high Ro_b approaches the value for a purely translating wing. The decrease in the lift coefficient is associated with the weakening of the LEV caused by the reduced spanwise pressure gradient, allowing a lower spanwise vorticity transport.

The study of the three dimensional parameter space revealed that the effects of the $A\!\!R$, Re, and Ro can be decoupled by using the span-based Reynolds number (Re_b) and span-based Rossby number (Ro_b). The combined effects of these parameters can be seen in the contours of $\overline{C}_L$ mapped on the plane of $A\!\!R$ and Re_b in figure 5.13(a) and on

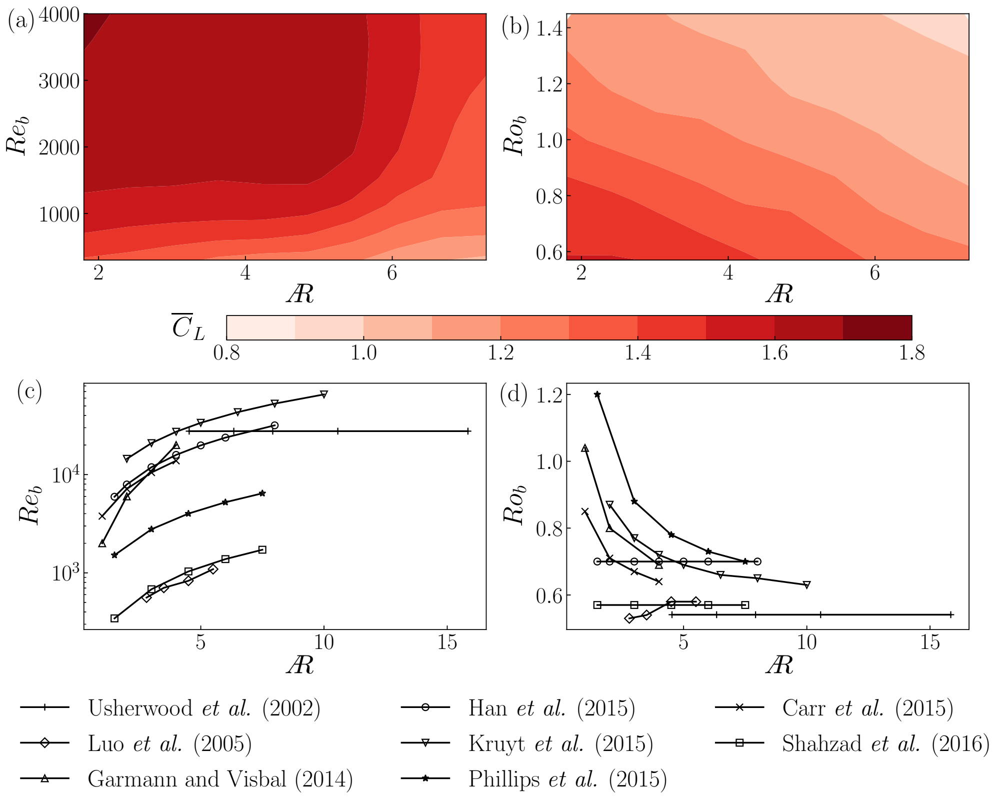

FIGURE 5.13: The contours of $\overline{C}_L$ are shown on the plane of AR and Re_b in (a) for $Ro_b = 0.7$. The contours of $\overline{C}_L$ are shown on the plane of AR and Ro_b in (b) for $Re_b = 300$. The variations of Re_b and Ro_b with respect to AR in past studies are shown in (c) and (d), respectively.

the plane of AR and Ro_b in figure 5.13(b). The discrepancies in the literature, regarding the effects of AR, can be attributed to the simultaneous variation in Re_b and Ro_b. From the information about the geometry and kinematics given in the studies on AR-effects, their respective values of Re_b and Ro_b were computed. The variation of Re_b and Ro_b with respect to AR can be seen in figures (c) and (d), respectively.

Consider the data, for example, by Shahzad *et al.* (2016), where the value of Ro_b has been maintained to be constant. Their Re_b has increased with AR, which would result in an increased $\overline{C}_L$. However, an increase in AR beyond a certain value would cause a reduction in $\overline{C}_L$, cancelling out the increase due to Re_b. A combined effect of these parameters resulted in a small increase in $\overline{C}_L$ in the lower range of AR, followed by a relatively stable $\overline{C}_L$ at higher values of AR, as can be seen in their figure 26(c). Similarly, the data by Phillips *et al.* (2015) show an increase in Re_b and a decrease in Ro_b, both contributing to an increase in $\overline{C}_L$. An increase in AR beyond a certain value should decrease $\overline{C}_L$. A combined effect resulted in an increase $\overline{C}_L$ in the range

$1.5 \leq Æ \leq 6$, followed by a slight decrease in $\overline{C}_L$ at higher Æ values, as can be seen in their figure 14(b).

It should be noted that most experimental studies have been conducted at very high Reynolds numbers ($Re_b \sim 10^4$), which are beyond the scope of the present study. At these Reynolds numbers, the viscous effects have a lower importance and a strong spanwise flow might cause an early bursting of the LEV with very high undulations in the LEV structures. Hence, it might be difficult to identify the LEV characteristics, such as the LEV split location. Therefore, in a future study at a higher Re_b, a different approach may be required to verify the correlation of the span-based Reynolds number with the flow structures. Based on the Reynolds-number range used in this study, the proposed scaling laws may hold for the flapping flight of most insects. However, in the higher range, a critical Reynolds number might exist, beyond which these laws will be unworkable.

The present study considers all the cases with a constant angle of attack ($\alpha = 45°$). However, it has been shown by previous studies (e.g. Kruyt *et al.*, 2015) that the flight performance of a wing also depends on α. At high Reynolds numbers ($Re_b \sim 10^4$), the wings of high Æ perform better if they maintain a lower α. This is because, in this range of Re_b, the high-Æ wings have a lower $\overline{C}_L/\overline{C}_D$ ratio than the low-Æ wings. Hence, for the high-Æ wings, the value of $\overline{C}_D$ can be reduced by lowering α, without having a significant reduction in $\overline{C}_L$. Hence, in the design of the wings of micro air vehicles, the proposed scaling laws should be considered in conjunction with the choice of an appropriate angle of attack.

5.5 Summary

Recent studies have shown that the effects of the wing aspect ratio, Reynolds number and Rossby number on the flow over a rotating wing are coupled. In this study, we have tried to uncouple the effects of these parameters by suggesting the wing-span as a length scale for the Reynolds number and Rossby number. Furthermore, the reasons behind the variation in the lift coefficients in all the cases have been explored by observing the flow structures.

The study was conducted using three-dimensional direct numerical flow simulations. From the observed flow structures, the wing-span was confirmed to be a more relevant length scale than the wing-chord for the LEV structure formed over the wing, supporting the modified way of scaling the Reynolds number (Re_b) proposed by Harbig *et al.* (2013). Wings of different aspect ratios were found to have a similar LEV structure at a constant Re_b, even when their roots were offset from the rotation axis. Moreover, based on the mean lift-coefficient ($\overline{C}_L$) acting on the wing, the low-$\mathcal{R}$ wings were observed to perform better at all investigated Reynolds numbers, whereas the high-$\mathcal{R}$ wings were observed to perform better only at high Reynolds numbers. This may provide useful insights into the range of wing aspect-ratios observed at different Reynolds numbers in nature.

Experimental models of rotating wings involve a central body, for which the wing is offset from its rotation axis. In the present study, the effect of the presence of the central body was also investigated. For a low offset, the values of C_L remained constant past $t/T = 0.3$ due to a stable LEV. However, at higher offsets ($\hat{b}_0 > 0.5$), C_L was observed to decrease continuously with time, suggesting a significant influence of the presence of the central body.

Furthermore, the effects of Rossby number were studied by varying the wing-root offset over a wide range. The flow structures over various $\mathcal{R}$ wings were observed to be similar with a constant R_g/b rather than a constant R_g/c, suggesting that the ratio R_g/b describes the Rossby number better. The values of $\overline{C}_L$ were observed to decrease with R_g/b, approaching the value for the translating wing. This reduction was shown to be due to the reduction in suction pressure on the wing surface. This was further observed to be caused by weakening of the LEV on account of the reduced spanwise pressure gradient and the spanwise vorticity transport.

The combined effects of the three parameters were shown on the contour maps of $\overline{C}_L$ on $\mathcal{R}$-Re_b and $\mathcal{R}$-Ro_b planes. The discrepancies in past studies regarding the effects of $\mathcal{R}$ on $\overline{C}_L$ may be explained by the variations in Re_b and Ro_b with respect to $\mathcal{R}$. The effects of the aspect ratio, Reynolds number, and Rossby number were shown to be decoupled by using the wing span as the length scale for the Reynolds number and Rossby number.

Chapter 6

Evolutionary Shape Optimisation of a Rotating Wing

6.1 Introduction

In past studies, it has been established that the stably attached leading-edge vortex (LEV) plays a key role in achieving a stable lift during the rotational translation phase of flapping wings of insects (Maxworthy, 1979; Ellington *et al.*, 1996). The LEV is spiral in structure, growing in size from the wing root to the wing tip. The LEV growth is constrained by the trailing edge, which also limits the aerodynamic forces generated by the LEV (Garmann & Visbal, 2014). The chord length at a spanwise location determines the distance between the leading edge and the trailing edge at that location. Hence, it is important to study the effects of wing shapes, with varying chord, on the aerodynamic forces. This may also be of interest to the studies on winged seeds, such as a maple seed, which auto-rotate when falling.

Past studies indicate that the semi-elliptic planforms can perform better than other generic shapes, such as rectangles and triangles, as described in chapter 2. Wing shapes can be characterised by the non-dimensional radius of the k^{th} moment of inertia, derived as

$$\hat{r}_k^k = \int_0^1 \hat{c}\hat{r}^k \mathrm{d}\hat{r}, \quad k = 1, 2, 3, ..., \tag{6.1}$$

where $\hat{c}$ is the local wing chord normalised by the mean chord and $\hat{r}$ is the spanwise distance normalised by the wing span. Ellington (1984a) has computed $\hat{r}_1$, $\hat{r}_2$, and $\hat{r}_3$ of various insect wings and proposed the *laws of wing shape* as

$$\hat{r}_2 = 0.929(\hat{r}_1)^{0.732} \quad \text{and} \qquad \hat{r}_3 = 0.900(\hat{r}_1)^{0.581}. \tag{6.2}$$

These laws are obeyed by most insect wings; however, the reasons for doing so are unknown. Ellington has also represented wing shapes analytically using the Beta distribution function, as mentioned in chapter 2.

Various researchers have used $\hat{r}_1$ as the criterion to compare the wing shapes. The lift coefficient ($\overline{C}_L$) has been observed to improve with an increase in $\hat{r}_1$, while the power economy reduced (Shahzad *et al.*, 2016). Wang *et al.* (2013) have used the Beta function to form various wing shapes of varying $\hat{r}_1$. They have recommended the use of the wings with a larger $\hat{r}_1$ for MAVs to maximise the lift and power economy.

Some past studies have proposed a variety of optimised wing shapes, where the aerodynamic loads were computed using quasi-steady models (Throneberry *et al.*, 2017; Ghommem *et al.*, 2014). However, the impact of the change in wing shapes on the flow structures has not been explored well. Moreover, the use of the evolutionary shape optimisation (ESO) approach, similar to that used in load bearing structures, does not appear to have been employed in wing shape studies.

ESO-based load bearing structures make an efficient use of building material to support the stresses in the structure. A similar method can be used in the case of a rotating wing to support the aerodynamic pressures on the wing surface. The results of Chapter 5 indicate that wings at different Reynolds numbers have different pressure distribution. Hence, in the present study, various wing shapes are obtained at different Reynolds numbers such that their areas support the surface pressures efficiently.

In this computational study, first, a rectangular wing of unity aspect ratio is rotated with various angular velocities in the range of insect Reynolds numbers. Based on the results, the wing is cut to eliminate the areas having lower magnitudes of the surface pressure. Its implications on the variation in $\overline{C}_L$ are then analysed. The ESO-based method of deriving optimal shapes may be useful in designing the MAV wing planforms at various Reynolds numbers.

6.2 Method

The model wing, having the span b, mean chord c, and thickness of $0.01b$, was placed at the centre of a cylindrical domain of diameter $18b$ and length $48c$, as has been described in chapter 3. Similar to the studies on insect wings (Birch & Dickinson, 2001; Harbig *et al.*, 2013; Carr *et al.*, 2015), the wing was maintained to be at a constant angle of attack ($\alpha = 45°$). It was initially accelerated over $t = 0.084T$ followed by a constant

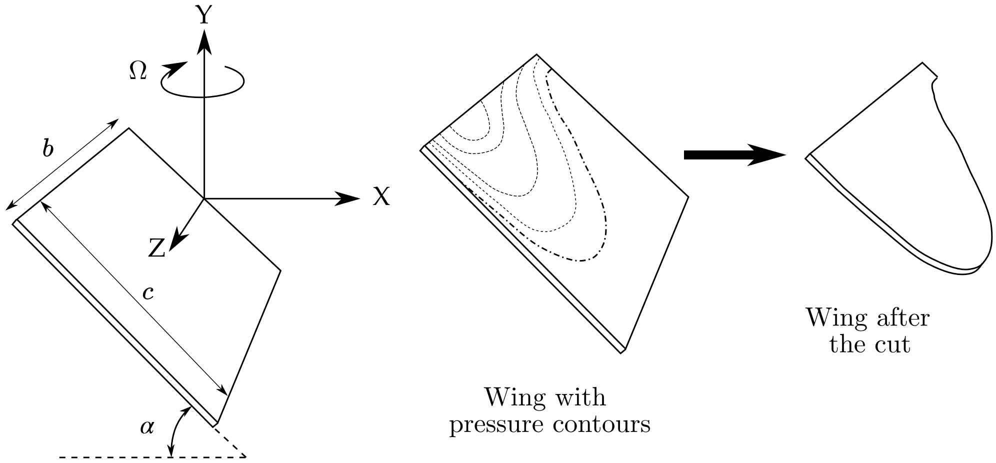

FIGURE 6.1: Schematic of the rotating wing model and the pressure-contour based wing cut.

angular velocity, which corresponds to the span-based Reynolds number,

$$Re_{span} = \frac{U_t b}{\nu}, \tag{6.3}$$

where U_t is the velocity of the wing tip and ν is the kinematic viscosity of the fluid. The shape optimisation was initiated with a rectangular wing of unity aspect ratio. The wing was rotated at the Re_{span} values of 520, 1732, 3465, and 6930, to determine the change in the optimised shapes at various Reynolds numbers. This range of Reynolds numbers overlapped with that for various insects such as a fruit fly ($Re_{span} \sim 520$), a crane fly ($Re_{span} \sim 2900$), and a beetle ($Re_{span} \sim 5200$).

The wing was rotated through 270°. The pressure contours on the wing's suction-side and pressure-side surfaces were extracted at the end of the simulation. The difference in the pressures from the two sides contributed to the overall lift and drag acting on the wing. In the subsequent design iteration, the wing was cut along a chosen pressure contour and the simulation was repeated with a new wing shape to observe the impact on the forces. The schematic of the wing and its coordinate system can be seen in figure 6.1. The method of obtaining the shapes based on ESO is explained in detail in § 6.4.

6.3 LEV and suction pressure

The LEV structure over a rotating wing is known to depend on the Reynolds number (Lentink & Dickinson, 2009b). At a higher Re_{span}, the LEV is relatively more compact with a higher spanwise vorticity flux than that at a lower Re_{span}. Since the LEV is

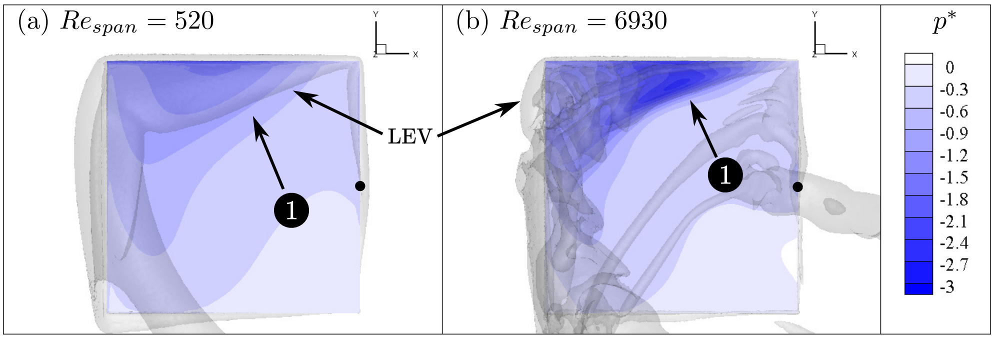

FIGURE 6.2: Wing suction pressure contours are shown for the wing of $\text{Æ} = 1$ rotating at $Re_{span} = 520$ in (a) and $Re_{span} = 6930$ in (b). At a high Re_{span} the magnitude of suction changes abruptly at location (1). The semitransparent surface shows the LEV structure identified using the constant Q-criterion. The small black dot represents the location of the wing root.

responsible for the suction, a change to the LEV structure with Reynolds number can also affect the pressure distribution over the wing surface. Therefore, the resulting optimised shape based on the pressure distribution can be expected to vary with the Reynolds number.

In the present study, initially, a wing of unity aspect ratio was rotated at $Re_{span} = 520$ and $Re_{span} = 6930$. The comparison of the resulting pressure distribution on the wing suction-side surface and the LEV structures is shown in figure 6.2. High magnitude of suction pressure is present beneath the LEV structures shown by transparent surfaces of a constant Q-criterion (Hunt *et al.*, 1988). The magnitude of suction has increased at $Re_{span} = 6930$ due to the increased spanwise transport of vorticity. At this Re_{span}, the increase in the contour levels seems to be very sharp near the LEV boundary, highlighted as location (1) in the figure. This represents a sharp increase in the magnitude of suction beneath the LEV. However, at $Re_{span} = 520$, the increase in the magnitude of suction is relatively more gradual. From this comparison, it may be inferred that, at a high Re_{span}, the suction is concentrated in a relatively smaller area. It can be noted that, at $Re_{span} = 6930$, a small vorticity at the wing root is transported diagonally towards the wing-tip by the action of the increased Coriolis acceleration.

The net lift on a wing results from the difference between the the pressures on the suction side (p_s) and the pressure side (p_p). The pressures can be normalised as

$$\begin{aligned} p_s^* &= p_s/(0.5\rho U_t^2), \\ p_p^* &= p_p/(0.5\rho U_t^2). \end{aligned} \tag{6.4}$$

The lift coefficient can be improved by maximising the difference of the pressures averaged over the wing area. This can be achieved by removing the wing area with very little pressures acting on it. This method of material removal is similar to the evolutionary structural optimisation (ESO), such as that described by Xie & Steven (1997). However, we removed the material using the surface pressure instead of the von-Mises stress, which is more relevant to load-bearing structures. The method of the shape optimisation is described in the following section.

6.4 Evolution of wing shapes from pressure contours

Initially, the rectangular wing of $\mathcal{AR} = 1$ was rotated at Reynolds numbers, $Re_{span} = 520, 1732, 3465$, and 6930. The comparison of the normalised pressures on the suction side (p_s^*) can be seen in figures 6.3 (a–d). For the same cases, the comparison of the normalised pressures on the pressure side (p_p^*) can be seen in figures (e–f). It can be seen that the distribution of p_s^* has changed with the Reynolds number. However, there is an insignificant change in p_p^*. The difference between the two pressures, $\Delta p^* = p_p^* - p_s^*$, contributes to the lift coefficient. Here, the pressures acting on the wing edges are neglected as the thickness of the wing is very small (1% of b), which exerts a negligible force. The contours of Δp^* are shown in figures (i–l).

It can be seen that a high Δp^* is concentrated in the region beneath the LEV that creates a large suction. A large area near the wing root and the trailing edge exerts a very low pressure. Such an inefficiently used material may be eliminated using a criterion for rejection, referred to as the *rejection ratio*, RR. The parts of the wing surface satisfying the following condition are removed from the model:

$$\frac{\Delta p_{mn}^*}{\Delta p_{max}^*} < RR_i, \tag{6.5}$$

where the subscript i denotes the design iteration number, Δp_{mn}^* is the value of Δp^* at a location of coordinates [m, n] on the wing surface, and Δp_{max}^* is the maximum value of Δp^* on the wing surface. In the subsequent design iteration ($i + 1$), the rejection ratio is modified by introducing the evolutionary rate (ER), such that

$$RR_{i+1} = RR_i + ER, \qquad i = 1, 2, 3, \dots . \tag{6.6}$$

In the present study, three iterations are performed with the initial rejection ratio, $RR_1 = 0.2$ and the evolutionary rate, $ER = 0.1$. To have an idea of various wing

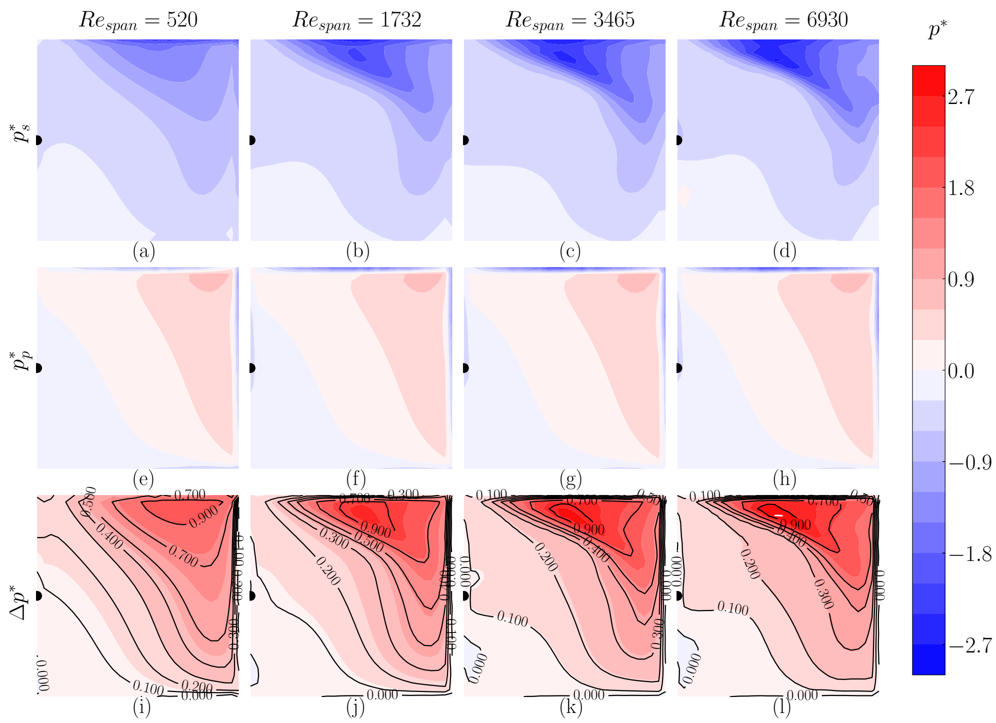

FIGURE 6.3: The contours of Δp^* (bottom row) are obtained by subtracting p_s^* (top row) from p_p^*(middle row) for $Re_{span} = 520$ (first column), $Re_{span} = 1732$ (second column), $Re_{span} = 3465$ (third column), and $Re_{span} = 6930$ (fourth column). The black dot represents the position of the wing-root. The coloured contours in the last row are superimposed with the black contour lines of constant rejection ratios.

shapes that can be produced at different values of RR, the contours of constant-RR criteria are superimposed onto the colour map of Δp^* contours in figures (i–l). The wing planform in an iteration i was obtained by cutting the rectangular wing along the contour of $\Delta p^*_{mn}/\Delta p^*_{max} = RR_i$. In some cases, such as for $RR_3 = 0.4$, where the wing root was completely removed, the wing span was reduced. To maintain a constant wing span, the wing was provided with an extension using a small strip at the wing root, with a normalised chord $c_p/b = 0.1$. In all shapes, the origin was maintained to be at the centre of the chord at the wing root.

6.5 Optimisation of wing shapes using the ESO method

The original rectangular wing shape was modified by creating new planforms using the ESO method, as discussed in the earlier section. The modified planforms were also simulated to rotate at the same Reynolds number as that of the rectangular wing. First,

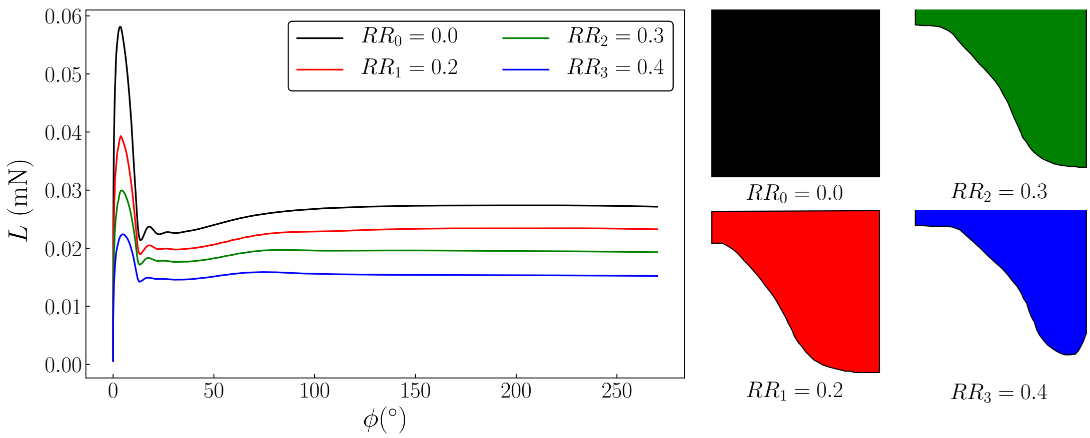

FIGURE 6.4: The time-traces of L are shown for the wing planforms obtained by rejection ratios $RR_1 = 0.2$ (red), $RR_2 = 0.3$ (green), and $RR_3 = 0.4$ (blue), rotating at $Re_{span} = 520$. The ratio RR_0 (black) corresponds to the original rectangular planform.

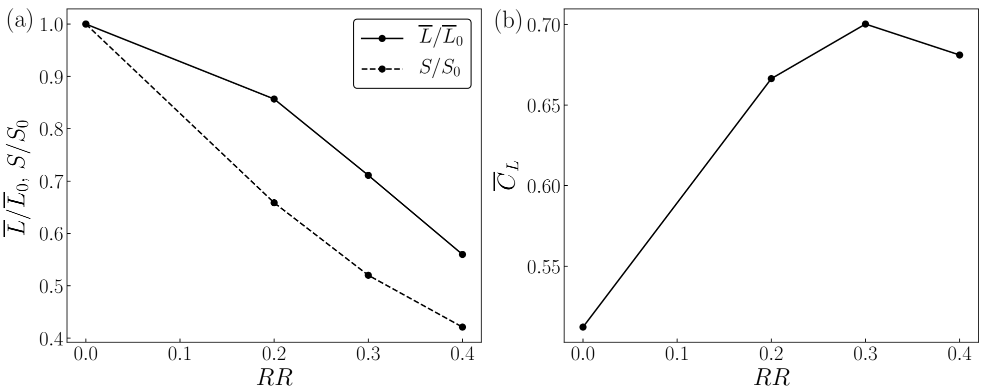

FIGURE 6.5: The iteration-wise variation of the mean lift relative to the that of the rectangular wing ($\overline{L}/\overline{L}_0$) and the variation of wing area relative to that of the rectangular wing are shown in (a). The variation of the mean lift coefficient ($\overline{C}_L$) is shown in (b). In these cases Re_{span} was maintained to be 520.

for $Re_{span} = 520$, the time-traces of the lift (L) were extracted and compared, as shown in figure 6.4. Here, the rejection ratio $RR_0 = 0$ corresponds to the original rectangular planform. It can be seen that L reaches a peak during the initial acceleration and then drops. Furthermore, after the rotation of approximately 100°, L reaches a stable value due to the stable leading-edge vortex, as also shown by Birch *et al.* (2004) and Carr *et al.* (2015). Hence, the mean lift ($\overline{L}$) can be obtained by averaging the data over the final 30° of rotation. It can be seen that $\overline{L}$ reduces with RR, due to a reduction in wing area. A decrease in the mean lift relative to the rectangular wing can be represented as $\overline{L}/\overline{L}_0$, where $\overline{L}_0$ is the mean lift over the rectangular wing at the same Reynolds number. Similarly, a decrease in the wing area (S) relative to the rectangular wing can be represented as S/S_0, where S_0 is the area of the rectangular wing.

The relative reductions in the mean lift and area are shown in figure 6.5(a). It can be seen that, even though the lift on the wing is reduced with RR, the wing area is reduced by a significantly larger amount. This resulted in an improved mean lift coefficient. Here, the mean lift and drag coefficients are calculated as

$$\overline{C}_L = \frac{2\overline{L}}{\rho U_t^2 S} \quad \text{and} \quad \overline{C}_D = \frac{2\overline{D}}{\rho U_t^2 S}, \tag{6.7}$$

where $\overline{D}$ is the mean drag over the wing. The variation of $\overline{C}_L$ with RR is shown in figure 6.5(b). The value of $\overline{C}_L$ increased with RR, with the peak reached at $RR = 0.3$. $\overline{C}_L$ starts decreasing beyond $RR = 0.3$, indicating that $RR = 0.3$ gives the maximum lift coefficient at $Re_{span} = 520$. In general, the modified planforms obtained from the design iterations were found to have a greater $\overline{C}_L$ than the rectangular wing. The design iterations were then repeated for different Reynolds numbers and the values of $\overline{C}_L$ were computed to determine the optimum RR at those Reynolds numbers.

The variation in $\overline{C}_L$ with the rejection ratio for various Re_{span} is shown as a contour map of $\overline{C}_L$ on the plane of RR and Re_{span} in figure 6.6(a). It can be seen that, for all Reynolds numbers, $\overline{C}_L$ reaches a maximum value at $RR = 0.3$ and starts decreasing beyond this ratio. Hence, the optimised wing shapes can be obtained with $RR = 0.3$ across all Reynolds numbers. The values of $\overline{C}_L$ for the optimised wing shapes are plotted as a function of Re_{span} in figure 6.6(b). The comparison with the values for the original rectangular wing at the same Reynolds numbers shows a remarkable 40% improvement in $\overline{C}_L$. Moreover, these values are also greater than those for the fruit fly wing planform rotated at the same Reynolds number.

From the optimised wing planforms shown in figure 6.6(b), it is clear that these wings have more area outboard. Hence, their centroids have moved further away from the wing root compared to the rectangular wing. The values $\hat{r}_1$ and $\hat{r}_2$ for the optimised shapes are summarised in table 6.1 along with the values for the rectangular and fruit fly wing planforms. This shows that the wings with higher values of $\hat{r}_1$ and $\hat{r}_2$ have a higher $\overline{C}_L$. This result is consistent with the findings of Shahzad *et al.* (2016) and Combes & Daniel (2001). It can be noted from figure 6.6(b) that the rectangular wing and the fruit fly wing have a similar $\overline{C}_L$ since their $\hat{r}_1$ and $\hat{r}_2$ values are very close.

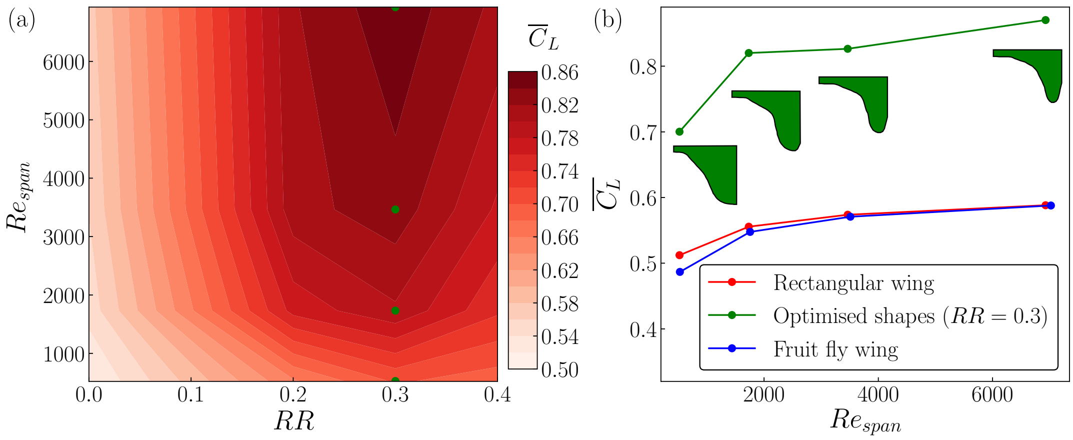

FIGURE 6.6: The contours of $\overline{C}_L$ are plotted on the plane of RR and Re_{span} in (a). In (b), the variation of $\overline{C}_L$ is plotted against Re_{span} for the rectangular wing, optimised shapes at $RR = 0.3$ and a fruit fly wing planform. The optimised $\overline{C}_L$ values are highlighted with green dots in (a) and the corresponding shapes are shown in (b).

Wing planform	$\hat{r}_1$	$\hat{r}_2$	$\mathcal{R}$
Rectangle ($RR = 0.0$)	0.50	0.58	1.00
Optimised shape ($RR = 0.3$) at $Re_{span} = 520$	0.68	0.71	1.92
Optimised shape ($RR = 0.3$) at $Re_{span} = 1732$	0.70	0.74	2.40
Optimised shape ($RR = 0.3$) at $Re_{span} = 3465$	0.71	0.75	2.87
Optimised shape ($RR = 0.3$) at $Re_{span} = 6930$	0.70	0.74	3.13
Fruit fly wing	0.52	0.57	2.91

TABLE 6.1: Characteristics of the wing shapes.

The pressures on the suction side surfaces of the optimised wing shapes are shown in figure 6.7. The pressures are distributed more efficiently than for the rectangular wing. At the Reynolds numbers of 1732, 3465, and 6930, it can be seen that the wing shapes are just sufficient to support the LEV structures. It can be seen that, when compared to the rectangular wing, the magnitude of suction pressures on the optimised wing shapes can be slightly reduced by the action of the opposite sign vorticity from the trailing edge. This is because the trailing edge has moved closer to the leading edge in the inboard area of the wing. However, the reduction in the magnitude is insignificant compared to the increase in $\overline{C}_L$ obtained by cutting a large amount of low-performing area, as discussed earlier. Furthermore, unlike for the rectangular wings, a small amount of trailing-edge vorticity is also observed to tilt into the wake at a location approximately 30% of the span of the optimised wings. This may be due to the inability of the trailing edge vortex to advect the vorticity along the trailing edge beyond a certain point. The

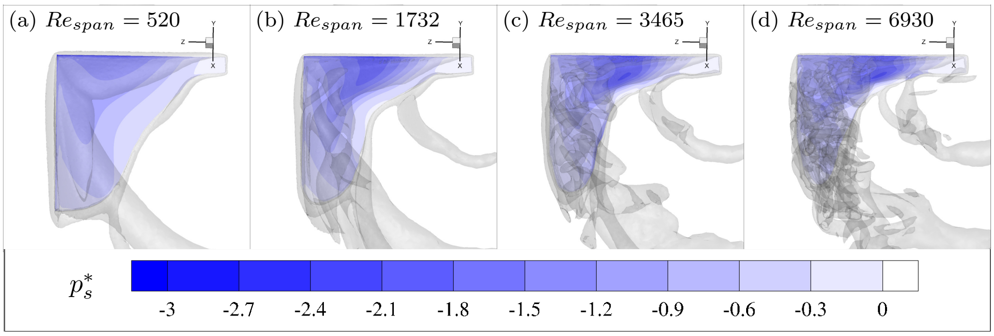

FIGURE 6.7: The normalised surface pressures on the optimised shapes (obtained from $RR = 0.3$) are distributed efficiently at (a) $Re_{span} = 520$, (b) $Re_{span} = 1732$, (c) $Re_{span} = 3465$, and (d) $Re_{span} = 6930$. The LEV structures are represented by the semi-transparent isosurfaces of the constant Q-criterion.

trailing edge becomes nearly vertical at the midspan location, requiring the advection of the trailing edge vorticity along the chordwise direction. The separation of this vorticity from the trailing edge might affect the suppression of the suction pressure, restoring a higher $\overline{C}_L$.

Furthermore, the effect on the power economy of the optimised wing shapes was also investigated. The power economy is the ratio of the mean lift coefficient and the mean power coefficient ($PE = \overline{C}_L/\overline{C}_P$). The mean power coefficient ($\overline{C}_L$) is calculated as

$$\overline{C}_P = \frac{2\overline{\tau}_y \Omega}{\rho U_t^3 S}, \tag{6.8}$$

where $\overline{\tau}_y$ is the mean fluid mechanical torque acting along the axis of rotation and Ω is the constant angular velocity. The comparison of the values of PE for the optimised wing shapes at different Reynolds numbers with those for the rectangular wing is shown in figure 6.8(a). This shows that the power economy of the optimised shapes is lower for any given Reynolds number than that for the rectangular wing. This is also in accordance with the result of Shahzad *et al.* (2016), which shows that the wings of a higher $\hat{r}_1$ have a lower PE. Interestingly, the fruit fly wing is observed to have the maximum PE, with a similar $\hat{r}_1$ to that of the rectangular wing. The reasons behind this difference were investigated further.

Wings with lower power economy require more power to rotate. This power is required to overcome the mean torque $\overline{\tau}_y$. The torque is derived from the mean drag coefficient ($\overline{C}_D$) resulting from the surface pressures and the radial location of the

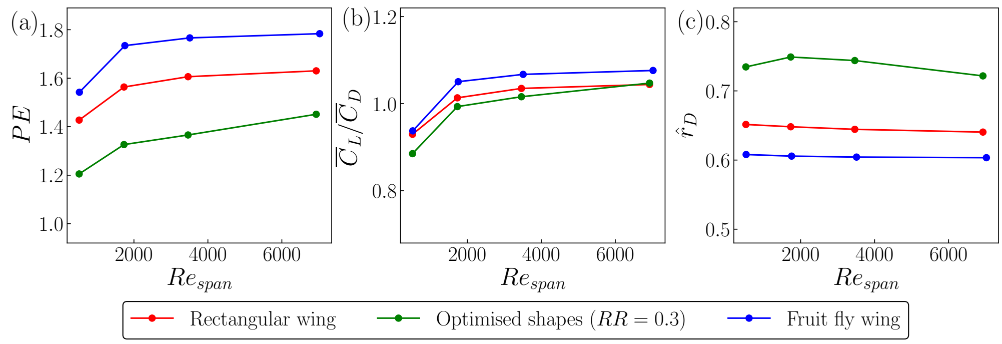

FIGURE 6.8: The variations of (a) power economy (PE), (b) $\overline{C}_L/\overline{C}_D$, and (c) normalised location of the point of application of drag ($\hat{r}_D$) with Re_{span} are shown for the rectangular wing, optimised wing shapes and the fruit fly wing.

centre of pressure. First, the variation of $\overline{C}_L/\overline{C}_D$ with Re_{span} was plotted for different wings, as shown in figure 6.8(b). Although the optimised wings have lower $\overline{C}_L/\overline{C}_D$, the difference is less than 5%. This implies that the increase in $\overline{C}_L$ of the optimised wings is accompanied by an increase in $\overline{C}_D$ by nearly an equal amount, since both the quantities directly depend on the surface pressures. Second, the variation of the normalised location of the point of application of drag ($\hat{r}_D = r_D/b$) was plotted for different wings, as shown in figure 6.8(c). The optimised wings have higher $\hat{r}_D$, which explains the increase in $\overline{C}_P$. The fruit fly wing has the lowest $\hat{r}_D$, and therefore, the highest PE. Decreasing $\hat{r}_1$ can further decrease $\hat{r}_D$ to obtain even higher PE. Insect wings could have evolved to their present shapes as a result of a compromise between maximum lift coefficient and maximum power economy. There may be several other factors, such as the resistance to bending and resistance to torsion, which require a broader chord inboard (Wootton, 1992; Ennos, 1989). The evolution of insect wing morphology has also been affected by the environmental factors and requirement for thermo-regulation, as has been discussed by Kingslover & Koehl (1994) and Johansson *et al.* (2009). However, some insect species, such as *Sceliphron* sp. and *Bombus* sp. do have a larger area outboard, i.e. a high value of $\hat{r}_1$.

From figure 6.8(a), it is clear that the fruit fly wing outperforms the optimised wings in terms of the power economy. This could be due to both, the lower drag coefficient and shorted moment arm. Since there is no significant difference between the $\overline{C}_L/\overline{C}_D$ ratios of the fruit fly wing and the optimised wings and $\overline{C}_L$ of the optimised wings is higher than that of the fruit fly wing, it is clear that $\overline{C}_D$ of the optimised wings must

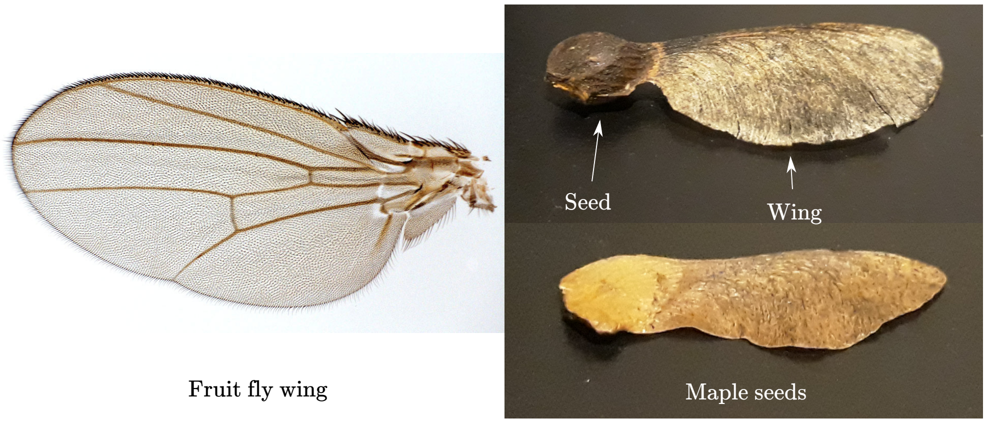

FIGURE 6.9: Wing shapes observed in nature have thicker roots, which help the $\hat{r}_1(m)$ to remain inboard. Fruit fly wing photo credit: David Hole, Florida State University. Maple seeds were photographed by me.

be higher. Moreover, this higher drag coefficient, together with a longer moment arm, creates a higher moment on the optimised wings. Hence, the optimised wings require a higher power coefficient to overcome the moment due to drag, which results in a lower power economy.

The optimised shapes may also be of interest to the studies on auto-rotating Samara seeds. The Samara seeds, such as maple seeds, are the winged seeds which auto-rotate while falling. In this case, no power input is required since the auto-rotation is caused by the action of the drag force. The seed requires sufficient lift to balance its weight, such that the seed falls with a constant velocity. The lower the velocity, the more it can be dispersed in the horizontal direction. Hence, obtaining the maximum possible lift is essential for the Samara seeds. Interestingly, the maple seeds also have a large area outboard, similar to the optimised wing shapes, implying that their wing shapes may have been evolved to generate a high lift. However, these seeds carry nuts situated at the wing root. Hence, most of their weight is concentrated near the wing root, which makes it fall only in certain orientations. For this reason, their wing roots cannot be too thin. It is also important to have a spanwise twist in these wings, which helps to start the auto-rotation, as has been discussed by Norberg (1973).

Overall, it was observed that a higher $\overline{C}_L$ would require a larger area outboard. However, the value of $\overline{C}_D$ would also increase simultaneously, as both the values depend on pressure. Hence, the power requirement to overcome the drag would also increase. One method of reducing the drag is to lower the angle of attack. However, it has been shown by Kruyt *et al.* (2015) that lower angles are beneficial for the wings of very large aspect ratios (and at a high Re_{span}). This is because, at a low Re_{span}, lower angles of attack may create a relatively smaller LEV, which would create a lower suction. Hence, the lift coefficient would also decrease, which is not desirable. Another method of reducing the power requirement is to lower the $\hat{r}_1$. For a simple flat plate planform, the area centroid, $\hat{r}_1(S)$, is same as the centre of mass $\hat{r}_1(m)$. However, the centre of mass can be shifted inward for the same planform by adding more mass to its root. The centre of pressure, which affects $\overline{C}_L$ and $\overline{C}_D$, is dependent on the spanwise wing area distribution, as seen in this study. Therefore, a larger $\overline{C}_L$ can be obtained by more outwards wing area. Simultaneously, a lower $\overline{C}_P$ can be obtained by moving the centre of mass inward using a thicker wing root.

Interestingly, it can be seen that a maple seeds have a heavy mass (seed) at their roots that helps in bringing $\hat{r}_1(m)$ down. Similarly, insect wings have a thick axillary area, where all the wing venation is connected. Moreover, the wing veins are thicker at the wing root and thinner towards the tip, helping $\hat{r}_1(m)$ to be inward. The pictures of a maple seed and a fruit fly wing can be seen in figure 6.9. This design in nature may help the wings to have a larger $\overline{C}_L$ and a lower $\overline{C}_P$ simultaneously.

6.6 Summary

In this study, the evolutionary structural optimisation (ESO) based method was used to optimise the shapes of rotating wings at various Reynolds numbers. The optimised shapes are efficient in their use of material to support the aerodynamic pressures. The mean lift coefficient of the wing ($\overline{C}_L$) was significantly improved in successive ESO iterations. The maximum $\overline{C}_L$ was obtained for the rejection ratio (RR) of 0.3. The optimised shapes are different for different Reynolds numbers. In general, the optimised wings exhibited larger areas outboard, similar to that observed in a few insects and Samara seeds. These shapes supported the LEV structures more efficiently than the rectangular wings, which are used in most experimental and numerical models in the studies on insect wing aerodynamics. The increase in the lift coefficient was also accompanied by an increase in the drag coefficient. However, with the increased drag coefficient and a more outboard location of the centre of pressure, the power requirement also increased, which resulted in a poor power economy. Most insect wings might have evolved as a compromise between a high lift coefficient and a high power economy, as semi-elliptic shapes. Nevertheless, the present study presents a new approach to obtain the optimised wing shape for any given Reynolds number while comparing its implications on the flow structures. This may be useful in designing the high-lift wings for MAVs.

Chapter 7

Effects of the Flapping Motion Profile

7.1 Introduction

Lift generated by the flow around steady wings is not enough to support the weight of small flyers due to the increased viscous resistance at the small scales. Hence, these flyers need to flap their wings in order to generate an extra lift and overcome the drag, requiring an additional power than their large gliding counterparts. Hence, flight of the hovering small flyers is costly compared to the large gliders. However, the high lift generated as a result of multiple unsteady mechanisms makes flapping essential for a stable flight at low Reynolds numbers. As discussed in earlier chapters, the flapping stroke of an insect comprises the rotational translation (or sweep) during a half stroke, followed by the flip motion (or pitch) towards the end of the half stroke. Two such half strokes, namely, the upstroke and downstroke, make a single flapping stroke. Although the mid-stroke aerodynamics can be represented well by the rotating wing models, they do not capture the unsteady effects during the flip motion, such as the rotational circulation and the wake capture, as discussed by Dickinson *et al.* (1999). The cycle-averaged aerodynamic loads may be different from the loads obtained in the quasi-steady state of a purely rotating wing. Hence, in order to have a complete idea of the kinematic efficiency of a flyer, it is important to study its flapping kinematics.

An insect wing is free to rotate around three orthogonal axes, allowing three degrees of freedom (3-DOF). The corresponding three Euler angles represent the phase angle (ϕ), the angle of attack (α), and the deflection angle (θ). It has been established that during 'normal hovering', an insect wing is minimally deflected (i.e. $\theta \sim 0$) and the wing flaps symmetrically in upstroke and downstroke along nearly a single horizontal plane

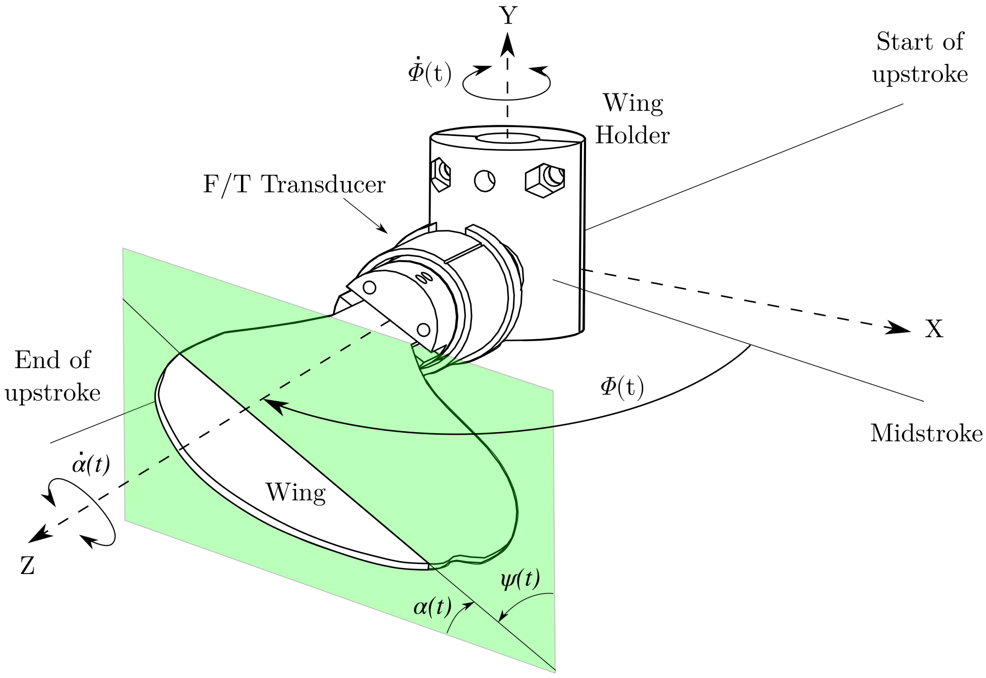

FIGURE 7.1: Schematic of the flapping wing setup.

(Rayner, 1979; Maxworthy, 1981). Hence, the important angles in this mode are ϕ and α, which are shown in the schematic in figure 7.1. Here, the coordinates are shown in the wing's reference frame, where the X axis is along the streamwise velocity, the Y axis is aligned with the sweep axis and the Z axis is aligned with the pitch axis. Also, ϕ is measured as the angular displacement of the wing span axis from the mid-stroke and α is measured as the angle made by the wing chord with the horizontal. Following the convention from the literature, the pitch angle (ψ) is defined such that $\alpha = \pi/2 - |\psi|$.

Various past studies have investigated the influence of the mean angles ($\overline{\phi}$ and $\overline{\alpha}$) and the maximum amplitudes of the these angles (ϕ_A and α_A), such as those by Berman & Wang (2007), Wang *et al.* (2013), and Zheng *et al.* (2013). Overall, they suggested the optimum amplitude values to be in the range $70° < \phi_A < 90°$ and $45° < \alpha_A < 55°$. The optimum mean phase angle was $\overline{\phi} = 0°$ and the optimum mean angle of attack was $\overline{\alpha} = 90°$. Berman & Wang (2007) showed a variation in the optimum ϕ_A based on the Reynolds number.

However, even for the given mean angles and amplitudes, the time-variation of the angles can impact the cycle-averaged aerodynamic loads. Berman & Wang (2007) have

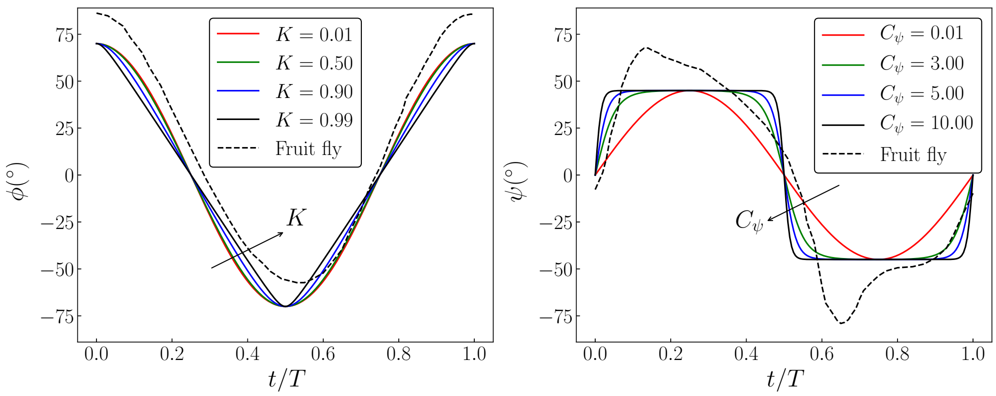

FIGURE 7.2: Flapping motion waveforms for ϕ and ψ obtained by varying the parameters K and C_ψ, respectively. The kinematics of a real free-flying fruit fly, shown by the dashed black lines, has been obtained by Fry *et al.* (2005).

suggested the following models to obtain various waveforms for the flapping kinematics:

$$\begin{aligned} \phi(t) &= \frac{\phi_A}{\sin^{-1} K} \sin^{-1}[K \sin(2\pi f t + \phi_\psi)] \qquad \text{and} \\ \psi(t) &= \frac{\psi_A}{\tanh(C_\psi)} \tanh[C_\psi \sin(2\pi f t)], \end{aligned} \tag{7.1}$$

where K is the sweep profile parameter varying in the limit $0 \leq K \leq 1$, C_ψ is the pitch profile parameter varying in the range $0 \leq C_\psi \leq 10$ and ϕ_ψ is the pitching phase offset. Typically, for a symmetric flip rotation with respect to the stroke reversal, $\phi_\psi = \pi/2$. An advanced rotation, with $\phi_\psi < \pi/2$, was observed to have a positive lift peak than that for a delayed rotation, with $\phi_\psi > \pi/2$ (Dickinson *et al.*, 1999). In equation 7.1, $\phi(t)$ is a smoothed triangular waveform, which becomes sinusoidal as K approaches 0. Similarly, $\psi(t)$ is a smoothed step waveform, which becomes sinusoidal as C_ψ approaches 0. The smoothed triangular waveform of $\phi(t)$ and the smoothed trapezoidal waveform of $\psi(t)$ used for a *robofly* by Dickinson and co-workers can be approximated by $K = 0.99$ and $C_\psi = 10$. The waveforms for various values of K and C_ψ are shown in figure 7.2.

Most experimental and numerical studies on flapping wings model sinusoidal waveforms, whereas some studies have used the simplified *robofly* model of Dickinson. The constant $\dot{\phi}(t)$ during the translation phase of the *robofly* model might be responsible for a stable lift. However, the rapid pitch motion towards the end of the stroke can create a high lift peak, which can make the overall flight unstable. On the contrary, a smooth harmonic waveform might not be optimal for generating a high cycle-averaged lift. Real insects are found to have more complex flapping waveforms, as have been shown by Ellington (1984b), Fry *et al.* (2005), and Zanker (1990). Hence, it is important to study the variation in the waveform and its impact on the flight performance. Some studies, such as those by Berman & Wang (2007), Ghommem *et al.* (2013), and Gogulapati *et al.* (2014) have studied the effects of flapping motion waveforms. However, these studies either use the quasi-steady models or two-dimensional numerical simulations to predict the forces on the wing. Such models may not completely capture the three-dimensional unsteady flow effects. The optimum values of K suggested from these studies also don't match with those in the real insects. Hence, it is important to present an experimental evidence to ascertain or challenge the existing results from the optimisation studies.

In this experimental study, a fruit-fly wing planform was made to flap at $Re_b = 275$ using various motion waveforms for the time-variations of ϕ and ψ. The performance was computed from direct measurements of the forces and torques along three Cartesian axes. The cycle averaged lift and power economy were observed to vary with the changes in the values of K and C_ψ. The optimum K and C_ψ values proposed from this study can help the MAVs to perform better than using the simplified kinematics.

7.2 Method

A fruit fly wing planform of the wing span, $b = 0.12$ mm, and aspect ratio, $\mathcal{R} = 2.91$, was attached rigidly to the ATI Nano17 IP68 F/T transducer at its root. The wing was fabricated from a 2 mm acrylic sheet. The ATI Nano17 transducer, along with the wing, was attached to a flapping mechanism allowing two degrees of freedom. The flapping mechanism was driven using two servo motors (model: EC-max30, Maxon Motor). Motor-1 controlled the sweep motion (about the Y axis) via the main shaft. Motor-2 controlled the pitch motion (about the Z axis) via a timing belt-and-pulley mechanism placed inside the hollow main shaft. The parts of the flapping wing assembly are shown in an exploded view in figure 7.3(a). A detailed description of the flapping mechanism can be found in § 3.1.3. The wing was offset from the sweep axis such that the offset ratio was $b_0/b = 0.5$. For this offset ratio, the flow over the wing can be assumed to be minimally affected by the central body, as explained in § 4.5.

The flapping frequency was maintained to be constant ($n = 0.55$ Hz), which resulted in a mean span-based Reynolds number ($Re_b = 275$) that closely matches that of a fruit

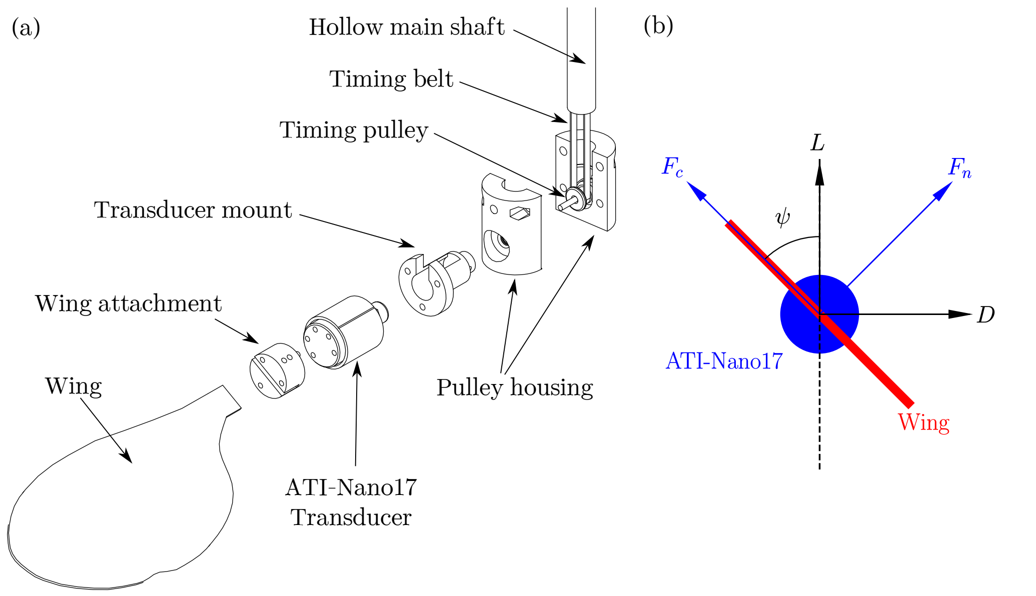

FIGURE 7.3: The parts of the flapping wing rig assembly are shown in an exploded view in (a). The schematic in (b) shows the alignment of the forces measured using ATI-Nano17 transducer attached to the wing root.

fly wing. Here, the reference velocity was computed as $U_g = 4n\phi_A R_g$, where R_g is the radius of gyration of the wing. Other parameters, which were maintained to be constant are the sweep amplitude ($\phi_A = 70°$), pitch amplitude ($\psi_A = 45°$), mean sweep angle ($\overline{\phi} = 0°$), mean pitch angle ($\overline{\psi} = 0°$), and pitching phase offset ($\phi_\psi = 90°$).

The flapping motion rig was mounted on a square tank of size $0.5 \times 0.5 \times 0.5$ m^3 filled with Stella food grade mineral oil of the kinematic viscosity, $\nu = 150$ mm^2/s. This high viscosity helped to maintain sufficiently high signal-to-noise ratio, even at the low Reynolds number. Mineral oil also helped in reducing the noise levels in the recorded signals by electrically and thermally isolating the transducer.

The ATI Nano17 transducer was attached to the wing in such a way that it always measured the forces and torques along the axes fixed to the wing's reference frame. As can be seen in figure 7.3(b), the transducer measured the forces along the wing chord (F_c) and normal to the wing (F_n). The lift and drag over the wing were calculated as

$$L = F_c \cos(\psi) + F_n \sin(\psi) \quad \text{and} \quad D = -F_c \sin(\psi) + F_n \cos(\psi), \tag{7.2}$$

respectively. The lift and drag coefficients of the wing were computed as

$$C_L = \frac{2L}{\rho U_g^2 S} \quad \text{and} \quad C_D = \frac{2D}{\rho U_g^2 S}, \tag{7.3}$$

where ρ is the density of the mineral oil and S is the wing area. The transducer also measured the torques about the axes along the chord and the normal, referred to as τ_c and τ_n, respectively. Hence, the torques along X-axis and Y-axis were computed as

$$\tau_x = -\tau_c \sin(\psi) + \tau_n \cos(\psi) \quad \text{and} \quad \tau_y = \tau_c \cos(\psi) + \tau_n \sin(\psi), \tag{7.4}$$

respectively. Moreover, the force and torque measured along the wing span (Z-axis) were referred to as F_z and τ_z, respectively. The coefficients of moments along the X, Y, and Z axes were computed as

$$C_{m_x} = \frac{2\tau_x}{\rho U_g^2 Sb}, \quad C_{m_y} = \frac{2\tau_y}{\rho U_g^2 Sb}, \quad \text{and} \quad C_{m_z} = \frac{2\tau_z}{\rho U_g^2 Sb}. \tag{7.5}$$

In a reverse stroke, the direction of the flow was reversed. Accordingly, the signs for F_n and τ_n were also reversed. The motors driving the flapping motion were equipped with encoders (model: ENC24 2RMHF, Maxon Motor) to measure the angular displacements ϕ and ψ. The F/T transducer, motors, and the encoders were connected to a Beckhoff EK1100 coupler in an EtherCAT based real time control system. The forces, torques, and angular displacements were sampled at 100 Hz and recorded using TwinCAT 3.0.

7.3 Repeatability of the flapping cycles

During an experiment, the wing starts flapping in the oil, which is initially quiescent. However, after the wing flips at the end of the half strokes, it leaves vortical structures in the wake, which influence the forces in the subsequent flapping cycle, due a phenomenon known as the wake capture (Dickinson *et al.*, 1999). Hence, the instantaneous forces at the same flapping phase may differ from one flapping cycle to the next. To check the repeatability of the forces, the wing was flapped 20 times and the forces and torques were recorded throughout the wing motion.

Figure 7.4(a) shows the imposed motion profile, where $K = 0.01$ and $C_\psi = 3$. The recorded F_n and F_c over 20 cycles are shown in figure 7.4(b) as 20 overlapping curves, which show an almost negligible deviation from the phase-averaged curve. Here, the phase-averaged curve is obtained by phase-averaging over 10 cycles, starting from the fifth cycle. The time traces of the corresponding lift and drag coefficients are shown in figure 7.4(c). The peak C_L during the upstroke and downstroke differs by a small amount ($< 10\%$), indicating the near-symmetric flapping motion in both half-strokes. Similarly, the time variations of moment coefficients C_{m_x}, C_{m_y}, and C_{m_z} are shown

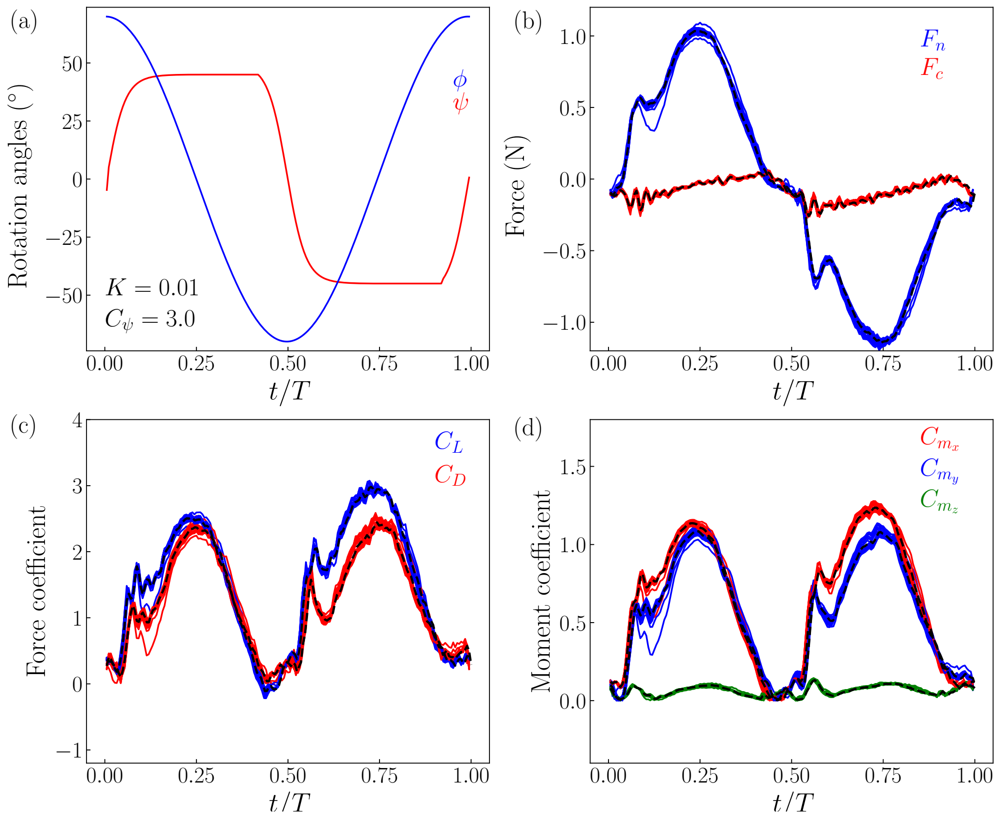

FIGURE 7.4: The time traces of 20 flapping cycles are shown for (a) the angles ϕ and ψ, (b) the forces F_n and F_c, (c) the lift and drag coefficients, (d) the moment coefficients along X, Y, and Z axes. The black dashed lines represent the values for a phase-averaged cycle.

in figure 7.4(d) and show a similar variation to that of the force coefficients. A little asymmetry between the two half-strokes may be on account of the backlash ($\sim 4°$) in the gear box of the driving motor-2, which slightly deviates the smooth flip motion profile. This is evident from the sharp corners in ψ curve in figure 7.4(a) near $t/T = 0.4$ and $t/T = 0.9$.

It should be noted that C_{m_z} has a negligible value throughout the flapping cycle. Hence, the power associated with the flip motion, which is on account of $(C_{m_z}\dot{\alpha})$ can be neglected in the total power calculations. The coefficient C_{m_y} is of interest, since most of the power is required to overcome this moment during the sweep motion.

7.4 Effects of the motion profile

The effects of the motion profiles on the wing aerodynamics were studied by systematically varying the values of K and C_ψ that changed the driven flapping waveforms.

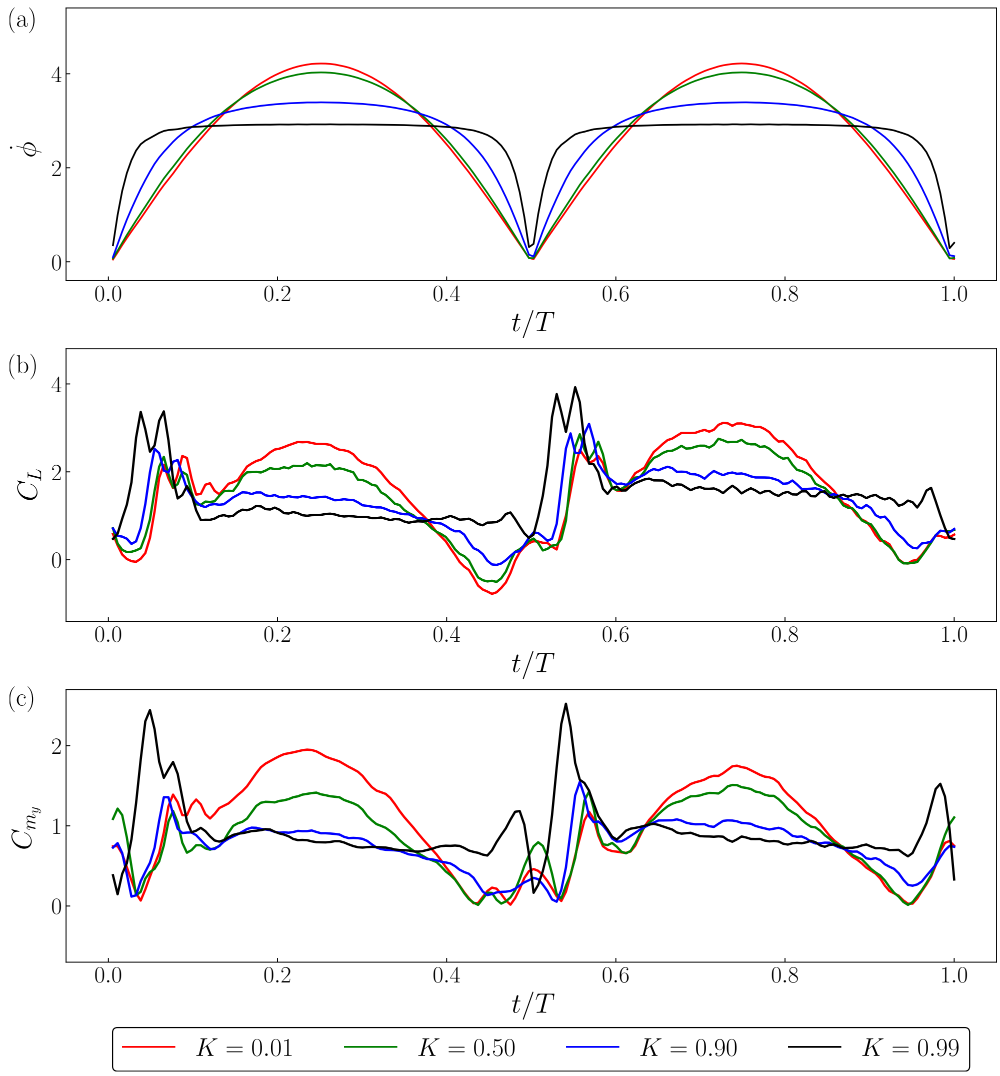

FIGURE 7.5: The sweep motion profile is varied by changing the values of K. The resulting time-traces of $\dot{\phi}$, C_L, and C_{m_y} are shown in (a), (b) and (c), respectively, for $C_\psi = 5$.

First, the pitching motion profile was maintained to be trapezoidal with $C_\psi = 5$. The sweep motion profile was varied by changing the K values in the range [0.01–0.99]. The resulting time traces of the lift coefficient and moment coefficient about Y-axis are shown in figures 7.5(b) and 7.5(c), respectively.

It can be seen that the time traces of both, the lift coefficient and the Y-moment coefficient, change with K. There is a peak at the start of the sweep motion in both half-strokes, followed by a second peak close to the midstrokes. The magnitude of the first peak increases with an increase in K. This peak is associated with the rapid pitch motion, whose effect is amplified by an increase in sweep acceleration with K. On the

K	Values at $t/T = 0.25$			Cycle-averaged values		
	$\dot{\phi}$ (rad/s)	C_L	C_{m_y}	$\overline{C}_L$	$\overline{C}_{m_y}$	PE
0.01	4.21	2.61	1.84	1.54	0.99	0.73
0.50	4.02	2.17	1.37	1.42	0.85	0.84
0.90	3.39	1.40	0.90	1.32	0.75	0.96
0.99	2.92	1.05	0.80	1.43	0.93	0.89

TABLE 7.1: Comparison of the values of $\dot{\phi}$, C_L, C_{m_y} at $t/T = 0.25$ and the cycle-averaged values of $\overline{C}_L$, $\overline{C}_{m_y}$, and PE is shown for various values of K.

contrary, the magnitude of the second peak decreases with K. This is because the sweep velocity profile, shown in figure 7.5(a), changes with K and reaches a nearly constant velocity throughout a major part of the sweep motion at $K = 0.99$. Although a high K value results in a nearly stable lift coefficient during the sweep, it also adversely affects the initial peak, creating a jerk at the start of the sweep motion. Therefore, with a high K, the flight may be relatively unstable (i.e. less smooth) compared to that at a low K. The difference between the time-traces of C_L for a sinusoidal sweep profile ($K \approx 0$) and a triangular sweep profile ($K \approx 1$) shown here is in agreement with that observed by Bos *et al.* (2008).

The effects of $\dot{\phi}$ on C_L and C_{m_y} are analysed by comparing their values at $t/T = 0.25$, as shown in table 7.1. It can be seen that the values of both C_L and C_{m_y} decrease monotonically with a decrease in $\dot{\phi}$, indicating a strong dependence of aerodynamic loads on the sweep velocity. The overall flight performance can be analysed by comparing the cycle averaged values of the lift and moment coefficients. As can be seen in table 7.1, the values of $\overline{C}_L$ and $\overline{C}_{m_y}$ decrease with an increase in K. However, the values are lowest for $K = 0.9$. The values for $K = 0.99$ are greater than those at $K = 0.9$, possibly because of the small positive peaks observed in the time-traces at $t/T = 0.45$ and 0.95.

The power required to flap the wing to overcome the aerodynamic loads can be normalised to give the power coefficient, which is computed as

$$C_P = \frac{2\tau_y\dot{\phi} + 2\tau_z\dot{\alpha}}{\rho U_g^3 S} = \frac{(2C_{m_y}\dot{\phi} + 2C_{m_z}\dot{\alpha})(b)}{U_g}. \tag{7.6}$$

As discussed earlier, the terms in C_{m_z} can be neglected due to their very low values. Hence, the expression for the power coefficient reduces to $C_P \approx 2C_{m_y}\dot{\phi}b/U_g$. The power economy, which is measure of the flight performance, can be calculated as $PE = \overline{C}_L/\overline{C}_P$, where $\overline{C}_P$ is the mean power coefficient. It can be observed from table 7.1

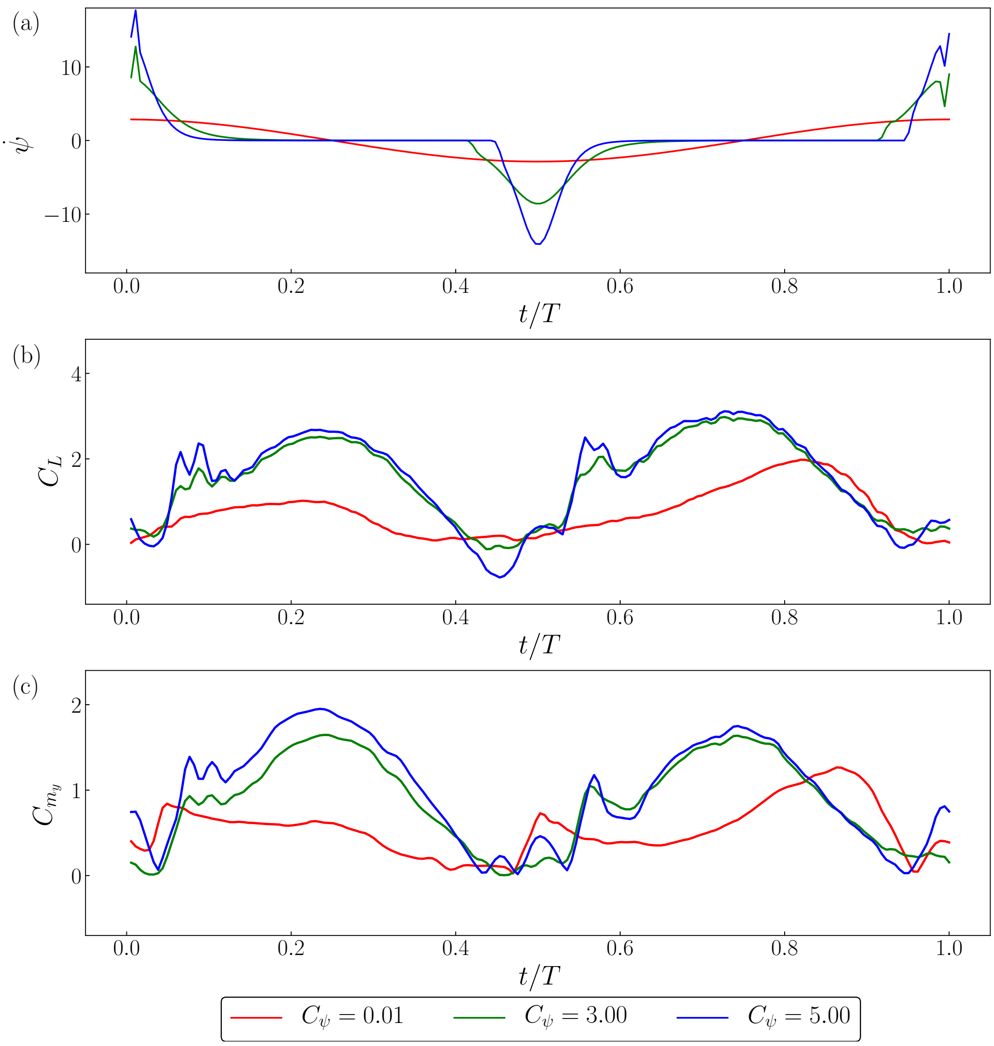

FIGURE 7.6: The pitch motion profile is varied by changing the values of C_ψ. The resulting time traces of $\dot{\psi}$, C_L, and C_{m_y} are shown in (a), (b) and (c), respectively, for $K = 0.01$.

that the power economy varies in an inverse proportion to $\overline{C}_L$. The maximum cycle-averaged lift is obtained for $K = 0.01$, which has the lowest PE and the lowest $\overline{C}_L$ is obtained for $K = 0.9$, which has the highest PE. Therefore, the selection of the parameter K is crucial in determining the performance in terms of the maximised lift and maximised power economy.

Furthermore, the sweep motion profile was varied by changing the values of C_ψ, while K was maintained to be 0.01. The resulting time-traces of the pitch-rotation velocity ($\dot{\psi}$), C_L, and C_{m_y} are shown in figure 7.6. It can be seen that there is a large change in C_L and C_{m_y} values when C_ψ changes from 0.01 to 3. However, for $C_\psi > 3$, the increase in the magnitudes of C_L and C_{m_y} is marginal.

C_ψ	Values at $t/T = 0.25$			Cycle averaged values		
	$\dot{\psi}$ (rad/s)	C_L	C_{m_y}	$\overline{C}_L$	$\overline{C}_{m_y}$	PE
0.01	0.0	0.86	0.58	0.74	0.54	0.73
3.00	0.0	2.49	1.59	1.49	0.86	0.80
5.00	0.0	2.61	1.84	1.54	0.99	0.73

TABLE 7.2: Comparison of the values of $\dot{\psi}$, C_L, C_{m_y} at $t/T = 0.25$ and the cycle averaged values of $\overline{C}_L$, $\overline{C}_{m_y}$, and PE is shown for various values of C_ψ.

The effects on the peak and the cycle averaged values are tabulated in table 7.2. At the mid-stroke, ($t/T = 0.25$), the wing is in a sweep motion. The pitch-rotation velocity at this instance is zero. However, the peak values of C_L and C_{m_y} are found to be dependent on C_ψ. The cycle averaged values also increase monotonically with C_ψ. The increased aerodynamic forces for $C_\psi = 5$ may be on account of maintaining a high angle of attack during most of the sweep motion. However, the power economy is minimally affected by C_ψ. Hence, it can be concluded that a larger value of C_ψ can result in a high flapping performance. However, Berman & Wang (2007) have predicted low values of C_ψ to be optimum, using the optimisation models. The discrepancies can be attributed to their force predictions models, which do not completely capture the effects of rotational forces and Coriolis forces that change with a change in C_ψ.

Finally, the sweep and pitch motion profiles were varied simultaneously by systematically varying K in the range $0.01 \leq K \leq 0.99$ and C_ψ in the range $0.01 \leq C_\psi \leq 5$. The performance was measured in terms of the mean lift coefficient and power economy in each case. The contours of $\overline{C}_L$ and PE are mapped on the planes of K and C_ψ, as can be seen in figure 7.7. High $\overline{C}_L$ can be obtained at a low K and a high C_ψ, whereas high PE can be obtained at a high K and a high C_ψ. Therefore, a high C_ψ results in a high performance, both in terms of $\overline{C}_L$ and PE. However, the selection of K is crucial in targeting a high $\overline{C}_L$ or a high PE.

7.5 Summary

In this study, the effects of the flapping motion profile were investigated by performing the experiments on a flapping wing and measuring its performance in terms of the mean lift coefficient ($\overline{C}_L$) and power economy (PE). The flapping motion rig involved two degrees of freedom, in the sweep and pitch. The corresponding motion profiles were varied by changing the values of the sweep profile parameter (K) and the pitch profile

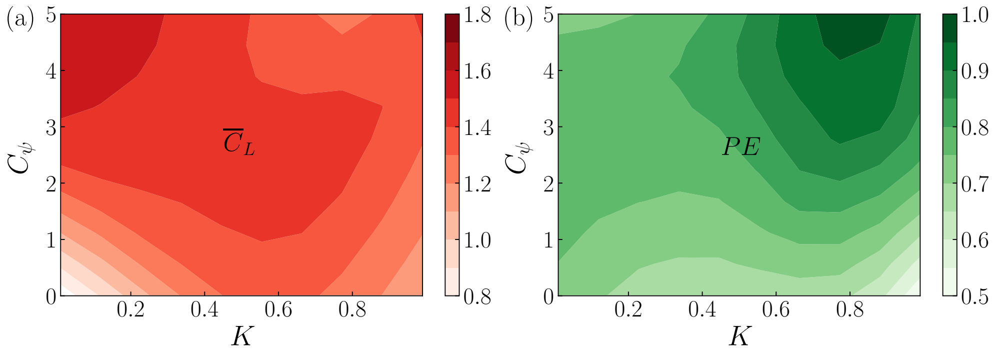

FIGURE 7.7: The contours of $\overline{C}_L$ and PE are shown on the K–C_ψ planes in (a) and (b), respectively.

parameter (C_ψ). The resulting $\overline{C}_L$ and PE values were mapped on the planes of K and C_ψ. Both $\overline{C}_L$ and PE were observed to be maximised by increasing C_ψ, which applied a trapezoidal pitch motion profile. However, changes to the value of K showed opposite effects on $\overline{C}_L$ and PE. A sinusoidal sweep motion profile, with a low K, maximised $\overline{C}_L$, whereas a triangular sweep motion profile, with a high K, maximised PE. These contour maps might be useful in determining appropriate flapping kinematics of a MAV. Additional information about the flow structure, in a future study, might be useful in explaining the variations observed in $\overline{C}_L$ and PE.

Chapter 8

Conclusions and Recommended Future Work

8.1 Conclusions

In this thesis, the aerodynamics of both rotating and flapping wings is investigated using both experimental and computational analyses. Review of the past studies on the effects of various geometrical and kinematic parameters on the wing aerodynamics revealed some challenges. These challenges are addressed in the present thesis. The investigation comprises four broad studies, the conclusions of which are discussed below.

8.1.1 Effects of the central body size

The central body size can affect the leading-edge vortex (LEV) structure over a rotating wing in two ways; first, by making the wing-root to be offset from the rotation axis that reduces the spanwise velocity gradient and second, on account of the secondary flow generated near the wall of the rotating central body, which can potentially interfere with the LEV formed at the wing root. The offset ratio, $\hat{b}_0$ was calculated as the wing-root offset (b_0) normalised by the wing span (b). Scanning PIV experiments were conducted to capture the three-dimensional LEV structure over the rotating wing with the offset ratio varying in the range $\hat{b}_0 \in [0, 0.5]$. The large scale LEV structure shows a negligible change for offset ratios $0 \leq \hat{b}_0 \leq 0.25$. However, the strength of the secondary vortex, which is formed near the mid-chord region after the LEV splits, reduces with an increase in $\hat{b}_0$. Ultimately, for $\hat{b}_0 > 0.25$, there is a dramatic change in the large-scale LEV, with no split occurring in it. The effect of the secondary flow at the central body wall was investigated using numerical simulations of rotating wings with offsets, with and without a central body. The presence of a central body, with offset ratio in the range $\hat{b}_0 \leq 0.5$, was found to have a negligible influence on the lift over the wing. This range includes the offset ratios typically used in experiments. Beyond this range, the presence of a central body has a detrimental effect on the lift, indicating that the effects of the secondary flow are significant. Overall, it can be concluded that the aerodynamics of a rotating wing is affected markedly beyond a certain central body size. The range of offsets, within which the flow and the forces are minimally affected, does cover the typical range of offsets used in experimental models and micro air vehicles.

8.1.2 Effects of aspect ratio, Reynolds number and Rossby number

In this study, The individual and combined influences of aspect ratio, Reynolds number, and Rossby number on the leading-edge vortex (LEV) of a rotating wing of insect-like planform are investigated numerically. A previous study from our group (Harbig *et al.*, 2013) has determined the wing span to be an appropriate length-scale governing the large-scale LEV structure. In this study, the aspect ratio range considered is further extended, to show that this scaling works well as the aspect ratio is varied by a factor of 4 ($1.8 \leq AR \leq 7.28$) and over a Reynolds number range of two orders of magnitude. The present study also extends this scaling for wings with an offset from the rotation axis, which is typically the case for actual insects and often for experiments. Remarkably, the optimum range of aspect ratios based on the lift coefficients at different Reynolds numbers coincide with those observed in nature.

The scaling based on the wing-span is extended to the acceleration terms of the Navier-Stokes equations, suggesting a modified scaling of the Rossby number, which decouples the effects of aspect ratio. By varying the Rossby number over a wide range ($1.67 \leq Ro \leq 10$), the lift on the wing is shown to decrease with increasing Rossby number, asymptoting to the value for a translating wing. A detailed investigation of the flow structures, by increasing the Rossby number in a wide range, reveals the weakening of the LEV due to the reduced spanwise flow, resulting in a reduced lift. Overall, the use of span-based scaling of the Reynolds and Rossby numbers, together with the aspect ratio, may help reconcile apparent conflicting trends between observed variations in aerodynamic performance in different sets of experiments and simulations.

8.1.3 Evolutionary shape optimisation of a rotating wing

Motivated by various wing shapes found in insects flying at various Reynolds numbers, optimisation of wing shape is performed for a range of wing-tip-velocity-based Reynolds numbers, $Re_{span} \in [500, 7000]$. The past optimisation studies involve force predictions from quasi-steady models, whereas the present study establishes a new approach, i.e. the evolutionary shape optimisation (ESO). This approached is derived from the evolutionary structural optimisation of the load-bearing structures. In this method, the wing surface pressure is used as the rejection criterion. Starting from a rectangular wing with $\AE = 1$, the areas with low pressure magnitudes, contributing negligibly to the lift coefficient, are removed in the subsequent design iterations. The rejection ratio (RR) is modified in each iteration. $RR = 0.3$ is found to result in the shapes having the maximum $\overline{C}_L$ across all the investigated Reynolds numbers.

The optimised shapes are found to vary with Re_{span}. However, all the shapes exhibited a larger area distributed outboard. This also resulted in a relatively lower power economy (PE). It is concluded that a larger outboard area is beneficial for $\overline{C}_L$ and larger inboard area is beneficial for PE. In nature, a compromise between the two parameters can be found. Interestingly, some insect wings and winged seeds are found to have a larger outboard area; however, their power economy is maintained to be high by their mass concentrated more inboard.

8.1.4 Effects of the flapping wing motion profile

In this experimental study, the effects of various flapping motion profiles on the performance of a fruit fly wing are investigated. The wing was made to flap in a mineral oil tank and the forces and torques over the wing were measured to assess its performance. The flapping motion involved two degrees of freedom. The sweep motion waveform was varied from sinusoidal to triangular by changing the sweep profile factor in the range $0 \leq K \leq 1$. The pitch motion waveform was varied from sinusoidal to trapezoidal, independently, by changing the pitch profile factor in the range $0 \leq C_\psi \leq 10$. The resulting contours of $\overline{C}_L$ and PE were mapped on the K-C_ψ planes. Higher C_ψ is advantageous for obtaining both high $\overline{C}_L$ and high PE. However, K has a different effects on $\overline{C}_L$ and PE. High K results in a high PE, whereas low K results in a high $\overline{C}_L$. Moreover, time-traces of the lift at a high K were found to have sudden peaks at the start of the sweep motion, which might make the flight unstable. The time-traces for a low K were relatively smooth. Indeed, in insect wings, the sweep motion is found to be nearly sinusoidal, which can be approximated by $K \sim 0$, that gives a high $\overline{C}_L$ and a relatively smooth lift variation over a flapping cycle. The power economy of insects may be controlled by several other factors such as the mass distribution and wing twist. The suggested motion profiles from this study can help MAVs perform better than by using the standard harmonic motion profiles.

8.2 Recommendations for future work

The present study has investigated some of the key features of the insect flight. The proposed scaling laws and optimisation methods can be useful in the design of various components and kinematics of MAVs. The improved performance of the MAVs will be beneficial for the community, since they exhibit applications in a range of tasks from fire fighting to agriculture. The parameter space surrounding the investigation of the insect flight is very large, which includes several variables. Even though the present research tries to address some of the key challenges, some questions remain under-explored.

- The effect of wing flexibility is not well understood. The recent research shows that the lift on the wing is improved with its flexibility; however, the interaction of the flow with the flexible wing is expected to change with the Reynolds number.
- The effects of anisotropy in the wing material needs to be investigated. Some outcomes of the present work indicate that the anisotropy might be helpful in the wing mass distribution to give a higher power economy. This can be investigated in detail by designing the wings of various venation patterns and variable thicknesses and observing its implications.
- The suggested span-based scaling of Reynolds and Rossby numbers is verified in the insect range of Reynolds numbers. However, the study of this scaling at higher Reynolds numbers can provide useful insights into characterising the flow structures over large rotating wings, such as those of helicopters and wind turbines.
- The torque measurements on a flapping wing show that the torque about the pitch axis is very small, indicating the possibility of passive pitch motion. The passive pitch motion profile can be a function of the sweep motion profile. Moreover, the angle of attack at the mid-stroke in the passive pitching can change with the Reynolds number. The study of a passively pitching wing at various Reynolds numbers can provide useful insights into the wing pitching profiles and angles of attack observed in various insects.

Appendix A

Scaling of acceleration terms in Navier-Stokes equations

To understand the influence of Rossby number and Reynolds number on the flow better, the Navier-Stokes (NS) equations are revisited by examining the key scalings using the method similar to Lentink & Dickinson (2009a). The vector NS equation in a rotating frame-of-reference is given by

$$\rho\frac{D\boldsymbol{u}}{Dt}+\rho\dot{\boldsymbol{\Omega}}\times\boldsymbol{r}+\rho\boldsymbol{\Omega}\times(\boldsymbol{\Omega}\times\boldsymbol{r})+2\rho\boldsymbol{\Omega}\times\boldsymbol{u}=-\boldsymbol{\nabla}p+\mu\boldsymbol{\nabla}^2\boldsymbol{u}. \tag{A.1}$$

Lentink & Dickinson (2009a) have scaled the velocity terms by the wing-tip velocity (U_t) and the length terms by the mean chord (c). However, using the scaling based on the findings of Harbig *et al.* (2013) and the present study, the variables can be non-dimensionalised as follows: $\boldsymbol{u}^*=\boldsymbol{u}/U_g$, $t^*=tU_g/b$, $\boldsymbol{\Omega}^*=\boldsymbol{\Omega}/\Omega$, $\dot{\boldsymbol{\Omega}}^*=\dot{\boldsymbol{\Omega}}/\dot{\Omega}$, $\boldsymbol{r}^*=\boldsymbol{r}/b$, $p^*=p/(\rho U_g^2)$, and $\boldsymbol{\nabla}^*=b\boldsymbol{\nabla}$, where U_g is the velocity at the radius of gyration of the wing, Ω is the time-averaged angular velocity, $\dot{\Omega}$ is the time-averaged angular acceleration, and b is the wing span. Substituting these terms and dividing equation A.1 by $\rho {U_g}^2/b$ gives

$$\frac{D\boldsymbol{u}^*}{Dt}+\frac{\dot{\Omega}b^2}{U_g^2}\dot{\boldsymbol{\Omega}}^*\times\boldsymbol{r}^*+\frac{\Omega^2b^2}{U_g^2}\boldsymbol{\Omega}^*\times(\boldsymbol{\Omega}^*\times\boldsymbol{r}^*)+\frac{2\Omega b}{U_g}\boldsymbol{\Omega}^*\times\boldsymbol{u}^*=-\boldsymbol{\nabla}^*p^*+\frac{\mu}{\rho U_g b}\boldsymbol{\nabla}^{*2}\boldsymbol{u}^*. \tag{A.2}$$

Omitting the symbol * for simplicity and rearranging the terms, the equation can be rewritten as

$$\frac{D\boldsymbol{u}}{Dt}+\frac{(\dot{\Omega}/\Omega^2)}{(R_g/b)^2}\dot{\boldsymbol{\Omega}}\times\boldsymbol{r}+\frac{1}{(R_g/b)^2}\boldsymbol{\Omega}\times(\boldsymbol{\Omega}\times\boldsymbol{r})+\frac{2}{(R_g/b)}\boldsymbol{\Omega}\times\boldsymbol{u}=-\boldsymbol{\nabla}p+\frac{\mu}{\rho U_g b}\boldsymbol{\nabla}^2\boldsymbol{u}. \tag{A.3}$$

Thus, it can be noted that the viscous term scales with $\rho U_g b/\mu$, which is the span-based Reynolds number (Re_b). The angular and centripetal accelerations scale with $(R_g/b)^2$ and the Coriolis acceleration scales with R_g/b. For a constant speed rotation, the angular acceleration term can be omitted. With an increase in R_g/b, the influence of the centripetal and Coriolis accelerations reduces, which could have caused a reduction in the spanwise flow.

Bibliography

Achache, Y., Sapir, N. & Elimelech, Y. 2017 Hovering hummingbird wing aerodynamics during the annual cycle. I. Complete wing. *Royal Society Open Science* **4** (8).

Albagnac, J., Moulin, F. Y., Eiff, O., Lacaze, L. & Brancher, P. 2014 A three-dimensional experimental investigation of the structure of the spanwise vortex generated by a shallow vortex dipole. *Environmental Fluid Mechanics* **14**, 957–970.

Ansari, S. A., Knowles, K. & Zbikowski, R. 2008a Insectlike flapping wings in the hover. Part I: Effect of wing kinematics. *Journal of Aircraft* **45** (6), 1945–1954.

Ansari, S. A., Knowles, K. & Zbikowski, R. 2008b Insectlike flapping wings in the hover. Part II: Effect of wing geometry. *Journal of Aircraft* **45** (6), 1976–1990.

Aono, H., Liang, F. & Liu, H. 2008a Near- and far-field aerodynamics in insect hovering flight: an integrated computational study. *Journal of experimental biology* **211** (Pt 2), 239–257.

Aono, H., Shyy, W. & Liu, H. 2008b Vortex dynamics in near wake of a hovering hawkmoth. In *46th AIAA Aerospace Sciences Meeting and Exhibit*. AIAA Paper 2008-583.

Beals, N. & Jones, A. R. 2015 Lift production by a passively flexible rotating wing. *AIAA Journal* **53** (10), 2995–3005.

Bennett, L. 1966 Insect aerodynamics: Vertical sustaining force in near-hovering flight. *Science* **152** (3726), 1263–1266.

Berman, G. J. & Wang, Z. J. 2007 Energy-minimizing kinematics in hovering insect flight. *Journal of Fluid Mechanics* **582**, 153–168.

Birch, J. M. & Dickinson, M. H. 2001 Spanwise flow and the attachment of the leading-edge vortex on insect wings. *Nature* **412**, 729–733.

Birch, J. M., Dickson, W. B. & Dickinson, M. H. 2004 Force production and flow structure of the leading edge vortex on flapping wings at high and low Reynolds numbers. *Journal of Experimental Biology* **207** (7), 1063–1072.

Bomphrey, R. J. 2006 Insects in flight: direct visualization and flow measurements. *Bioinspiration & Biomimetics* **1** (4), S1–S9.

Bomphrey, R. J., Lawson, N. J., Harding, N. J., Taylor, G. K. & Thomas, A. L. R. 2005 The aerodynamics of *Manduca sexta*: digital particle image velocimetry analysis of the leading-edge vortex. *Journal of Experimental Biology* **208** (6), 1079–1094.

Bos, F. M., Lentink, D., Van Oudheusden, B. W. & Bijl, H. 2008 Influence of wing kinematics on performance in hovering insect flight. *Journal of Fluid Mechanics* **594**, 341–368.

Bross, M. & Rockwell, D. 2014 Flow structure on a simultaneously pitching and rotating wing. *Journal of Fluid Mechanics* **756**, 354–383.

Brücker, C. 1995 Digital-Particle-Image-Velocimetry (DPIV) in a scanning light-sheet: 3D starting flow around a short cylinder. *Experiments in Fluids* **19** (4), 255–263.

Caballero, J., Mazo, C., Rodriguez-Pinto, I. & Theobald, J. C. 2015 A visual horizon affects steering responses during flight in fruit flies. *Journal of Experimental Biology* **218** (18), 2942–2950.

Carr, Z. R., DeVoria, A. C. & Ringuette, M. J. 2015 Aspect-ratio effects on rotating wings: circulation and forces. *Journal of Fluid Mechanics* **767**, 497–525.

Chen, D., Kolomenskiy, D., Nakata, T. & Liu, H. 2018 Forewings match the formation of leading-edge vortices and dominate aerodynamic force production in revolving insect wings. *Bioinspiration & Biomimetics* **13** (1), 016009.

Cheng, B., Sane, S. P., Barbera, G., Troolin, D. R., Strand, T. & Deng, X. 2013 Three-dimensional flow visualization and vorticity dynamics in revolving wings. *Experiments in Fluids* **54** (1423), 1–12.

Combes, S. A. & Daniel, T. L. 2001 Shape, flapping and flexion: wing and fin design for forward flight. *Journal of Experimental Biology* **204** (12), 2073–2085.

Combes, S. A. & Daniel, T. L. 2003 Flexural stiffness in insect wings I. Scaling and the influence of wing venation. *Journal of Experimental Biology* **206** (17), 2979–2987.

David, L., Jardin, T., Braud, P. & Farcy, A. 2012 Time-resolved scanning tomography PIV measurements around a flapping wing. *Experiments in Fluids* **52**, 857–864.

De Clercq, K. M. E., de Kat, R., Remes, B., van Oudheusden, B. W. & Bijl, H. 2009 Aerodynamic experiments on DelFly II: Unsteady lift enhancement. *International Journal of Micro Air Vehicles* **1** (4), 255–262.

Dickinson, M. H., Lehmann, F.-O. & Sane, S. P. 1999 Wing rotation and the aerodynamic basis of insect flight. *Science* **284** (5422), 1954–1960.

Dudley, R. & Ellington, C. P. 1990 Mechanics of forward flight in bumblebees: I. Kinematics and morphology. *Journal of Experimental Biology* **148** (1), 19 LP – 52.

Elimelech, Y., Kolomenskiy, D., Dalziel, S. B. & Moffatt, H. K. 2013 Evolution of the leading-edge vortex over an accelerating rotating wing. *Procedia IUTAM* **7**, 233–242.

Ellington, C. P. 1984a The aerodynamics of hovering insect flight. II. Morphological parameters. *Philosophical Transactions of the Royal Society B: Biological Sciences* **305** (1122), 17–40.

Ellington, C. P. 1984b The aerodynamics of hovering insect flight. III. Kinematics. *Philosophical Transactions of the Royal Society B: Biological Sciences* **305** (1122), 41–78.

Ellington, C. P. 1999 The novel aerodynamics of insect flight: applications to micro-air vehicles. *Journal of Experimental Biology* **202**, 3439–3448.

Ellington, C. P., van den Berg, C., Willmott, A. P. & Thomas, A. L. R. 1996 Leading-edge vortices in insect flight. *Nature* **384** (6610), 626–630.

Ennos, A. R. 1989 Inertial and aerodynamic torques on the wings of diptera in flight. *J. Exp. Biol.* **142** (1), 87–95.

Fouras, A., Lo Jacono, D. & Hourigan, K. 2008 Target-free Stereo PIV: A novel technique with inherent error estimation and improved accuracy. *Experiments in Fluids* **44**, 317–329.

Fry, S. N., Rohrseitz, N., Straw, A. D. & Dickinson, M. H. 2008 TrackFly: Virtual reality for a behavioral system analysis in free-flying fruit flies. *Journal of Neuroscience Methods* **171** (1), 110–117.

Fry, S. N., Sayaman, R. & Dickinson, M. H. 2005 The aerodynamics of hovering flight in Drosophila. *Journal of Experimental Biology* **208** (12), 2303–2318.

Garmann, D. J. & Visbal, M. R. 2013 A numerical study of hovering wings undergoing revolving or translating motions. In *31st AIAA Applied Aerodynamics Conference*. Reston, Virginia: AIAA Paper 2013-3052.

Garmann, D. J. & Visbal, M. R. 2014 Dynamics of revolving wings for various aspect ratios. *Journal of Fluid Mechanics* **748**, 932–956.

Garrick, I. E. 1936 Propulsion of a flapping and oscillating airfoil. *Tech. Rep.* 567. National Advisory Committee for Aeronautics.

Ghommem, M., Collier, N., Niemi, A. H. & Calo, V. M. 2014 On the shape optimization of flapping wings and their performance analysis. *Aerospace Science and Technology* **32** (1), 274–292.

Ghommem, M., Hajj, M. R., Mook, D. T., Stanford, B. K., Beran, P. S. & Watson, L. T. 2013 Global-local optimization of flapping kinematics in hovering flight. *International Journal of Micro Air Vehicles* **5** (2), 4–7.

Gogulapati, A., Friedmann, P. P. & Martins, J. R. R. A. 2014 Optimization of flexible flapping-wing kinematics in hover. *AIAA Journal* **52** (10), 2342–2354.

Graftieaux, L., Michard, M. & Grosjean, N. 2001 Combining PIV, POD and vortex identification algorithms for the study of unsteady turbulent swirling flows. *Measurement Science and Technology* **12** (9), 1422–1429.

Green, M. A., Rowley, C. W. & Smits, A. J. 2011 The unsteady three-dimensional wake produced by a trapezoidal pitching panel. *Journal of Fluid Mechanics* **685**, 117–145.

Han, J.-S., Chang, J. W. & Cho, H.-K. 2015 Vortices behavior depending on the aspect ratio of an insect-like flapping wing in hover. *Experiments in Fluids* **56** (9), 181.

Han, J. S., Chang, J. W. & Kim, S. T. 2014 Reynolds number dependency of an insect-based flapping wing. *Bioinspiration & Biomimetics* **9** (4), 046012.

Harbig, R. R. 2014 Role of wing morphology in the aerodynamics of insect flight. PhD thesis, Monash University.

Harbig, R. R., Sheridan, J. & Thompson, M. C. 2013 Reynolds number and aspect ratio effects on the leading-edge vortex for rotating insect wing planforms. *Journal of Fluid Mechanics* **717**, 166–192.

Harbig, R. R., Sheridan, J., Thompson, M. C., Ozen, C. A. & Rockwell, D. 2012 Observations of flow structure changes with aspect ratio for rotating insect wing planforms. In *42nd AIAA Fluid Dynamics Conference and Exhibit*. AIAA Paper 2012-3082.

Harrison, J. F., Kaiser, A. & VandenBrooks, J. M. 2010 Atmospheric oxygen level and the evolution of insect body size. *Proceedings of the Royal Society B: Biological Sciences* **277** (1690), 1937–1946.

Hawkes, E. W. & Lentink, D. 2016 Fruit fly scale robots can hover longer with flapping wings than with spinning wings. *Journal of the Royal Society Interface* **13** (123), 20160730.

Hu, Y. & Wang, J. J. 2011 Dual leading-edge vortex structure for flow over a simplified butterfly model. *Experiments in Fluids* **50** (5), 1285–1292.

Hunt, J. C. R., Wray, A. A. & Moin, P. 1988 Eddies, streams, and convergence zones in turbulent flows. In *Center for Turbulence Research, Proceedings of the Summer Program*, pp. 193–208.

Jardin, T. 2017 Coriolis effect and the attachment of the leading edge vortex. *Journal of Fluid Mechanics* **820**, 312–340.

Jardin, T. & David, L. 2015 Coriolis effects enhance lift on revolving wings. *Physical Review E* **91** (031001), 1–4.

Jensen, M. 1956 Biology and physics of locust flight. III. The aerodynamics of locust flight. *Philosophical Transactions of the Royal Society B: Biological Sciences* **239** (667), 511–552.

Johansson, F., Söderquist, M. & Bokma, F. 2009 Insect wing shape evolution: independent effects of migratory and mate guarding flight on dragonfly wings. *Biological Journal of the Linnean Society* **97** (2), 362–372.

Jones, A. R., Medina, A., Spooner, H. & Mulleners, K. 2016 Characterizing a burst leading-edge vortex on a rotating flat plate wing. *Experiments in Fluids* **57** (4), 52.

Kang, C.-K. & Shyy, W. 2014 Analytical model for instantaneous lift and shape deformation of an insect-scale flapping wing in hover. *Journal of the Royal Society Interface* **11**, 20140933.

Kesel, A. B. 2000 Aerodynamic characteristics of dragonfly wing sections compared with technical aerofoils. *The Journal of Experimental Biology* **203**, 3125–3135.

Kim, D. & Gharib, M. 2010 Experimental study of three-dimensional vortex structures in translating and rotating plates. *Experiments in Fluids* **49** (1), 329–339.

Kingslover, J. G. & Koehl, M. A. R. 1994 Selective factors in the evolution of insect wings. *Annual Review of Entomology* **39**, 425–451.

Kruyt, J. W., van Heijst, G. F., Altshuler, D. L. & Lentink, D. 2015 Power reduction and the radial limit of stall delay in revolving wings of different aspect ratio. *Journal of the Royal Society Interface* **12**, 20150051.

Lawson, J. M. & Dawson, J. R. 2014 A scanning PIV method for fine-scale turbulence measurements. *Experiments in Fluids* **55** (12).

Lee, K.-B., Kim, J.-H., Park, J. S. & Kim, C. 2012 Unsteady aerodynamic effects of wing-body interactions in three-dimensional insects' flapping flight. In *50th AIAA Aerospace Sciences Meeting including the New Horizons Forum and Aerospace Exposition*. AIAA paper 2012-0419.

Lee, Y. J., Lua, K. B. & Lim, T. T. 2016 Aspect ratio effects on revolving wings with Rossby number consideration. *Bioinspiration & Biomimetics* **11** (5), 056013.

Lehmann, F.-O. 2002 The constraints of body size on aerodynamics and energetics in flying fruit flies: an integrative view. *Zoology* **105** (2002), 287–295.

Lentink, D. & Dickinson, M. H. 2009a Biofluiddynamic scaling of flapping, spinning and translating fins and wings. *Journal of Experimental Biology* **212** (16), 2691–2704.

Lentink, D. & Dickinson, M. H. 2009b Rotational accelerations stabilize leading edge vortices on revolving fly wings. *Journal of Experimental Biology* **212** (16), 2705–2719.

Leweke, T. 2012 Dye visualization - a method for investigating biomechanical flows. *Current Pharmaceutical Biotechnology* **13** (11), 2141–2152.

Lighthill, M. J. 1970 Aquatic animal propulsion of high hydromechanical efficiency. *Journal of Fluid Mechanics* **44**, 265–301.

Liu, G., Dong, H. & Li, C. 2016 Vortex dynamics and new lift enhancement mechanism of wingbody interaction in insect forward flight. *Journal of Fluid Mechanics* **795**, 634–651.

Liu, H. 2009 Integrated modeling of insect flight: From morphology, kinematics to aerodynamics. *Journal of Computational Physics* **228** (2), 439–459.

Liu, H. & Aono, H. 2009 Size effects on insect hovering aerodynamics: an integrated computational study. *Bioinspiration & Biomimetics* **4** (1), 15002.

Liu, H., Ellington, C. P., Kawachi, K., van den Berg, C. & Willmott, A. P. 1998 A computational fluid dynamic study of hawkmoth hovering. *Journal of Experimental Biology* **201** (4), 461–477.

Liu, H., Kolomenskiy, D., Nakata, T. & Li, G. 2017 Unsteady bio-fluid dynamics in flying and swimming. *Acta Mechanica Sinica* **33** (4), 663–684.

Liu, Y., Roll, J., Van Kooten, S. & Deng, X. 2018 Schlieren photography on freely flying hawkmoth. *Biology letters* **14** (5), 20180198.

Liu, Z. & Zheng, Y. 2006 PIV study of bubble rising behavior. *Powder Technology* **168**, 10–20.

Lu, Y., Shen, G. X. & Lai, G. J. 2006 Dual leading-edge vortices on flapping wings. *Journal of Experimental Biology* **209** (24), 5005–5016.

Luo, G. & Sun, M. 2005 The effects of corrugation and wing planform on the aerodynamic force production of sweeping model insect wings. *Acta Mechanica Sinica* **21** (6), 531–541.

Ma, K. Y., Chirarattananon, P., Fuller, S. B. & Wood, R. J. 2013 Controlled flight of a biologically inspired, insect-scale robot. *Science* **340** (6132), 603–607.

Marden, J. H. 1987 Maximum lift production during takeoff in flying animals. *Journal of Experimental Biology* **130** (1), 235–258.

Maxworthy, T. 1979 Experiments on the Weis-Fogh mechanism of lift generation by insects in hovering flight. Part 1. Dynamics of the 'fling'. *Journal of Fluid Mechanics* **93**, 47–63.

Maxworthy, T. 1981 The fluid dynamics of insect flight. *Annual Review of Fluid Mechanics* **13**, 329–350.

Minelli, A., Maruzzo, D. & Fusco, G. 2010 Multi-scale relationships between numbers and size in the evolution of arthropod body features. *Arthropod Structure and Development* **39** (6), 468–477.

Nabawy, M. R. A. & Crowther, W. J. 2016 Optimum hovering wing planform. *Journal of Theoretical Biology* **406**, 187–191.

Naidu, V., Young, J. & Lai, J. 2013 Effect of wing flexibility on the performance of tandem wings during hover flight. In *31st AIAA Applied Aerodynamics Conference*. AIAA paper 2013-3051.

Nakata, T. & Liu, H. 2012a A fluid–structure interaction model of insect flight with flexible wings. *Journal of Computational Physics* **231** (4), 1822–1847.

Nakata, T. & Liu, H. 2012b Aerodynamic performance of a hovering hawkmoth with flexible wings: a computational approach. *Proceedings. Biological sciences / The Royal Society* **279** (1729), 722–731.

Nguyen, T. T., Sundar, D. S., Yeo, K. S. & Lim, T. T. 2016 Modeling and analysis of insect-like flexible wings at low Reynolds number. *Journal of Fluids and Structures* **62**, 294–317.

Nijhout, H. F. & Callier, V. 2015 Developmental mechanisms of body size and wing-body scaling in insects. *Annual Review of Entomology* **60**, 141–156.

Norberg, R. A. 1973 Autorotation, self stability, and structure of single winged fruits and seeds (Samaras) with comparative remarks on animal flight. *Biological Reviews of the Cambridge Philosophical Society* **48** (4), 561–596.

Ozen, C. A. & Rockwell, D. 2013 Flow structure on a rotating wing: effect of wing aspect ratio and shape. In *51st AIAA Aerospace Sciences Meeting*. AIAA Paper 2013-676.

Phillips, N., Knowles, K. & Bomphrey, R. J. 2015 The effect of aspect ratio on the leading-edge vortex over an insect-like flapping wing. *Bioinspiration & Biomimetics* **10** (5), 056020.

Phillips, N., Knowles, K. & Bomphrey, R. J. 2017 Petiolate wings: effects on the leading-edge vortex in flapping flight. *Interface Focus* **7**, 20160084.

Phillips, N., Knowles, K. & Lawson, N. J. 2010 Effect of wing planform shape on the flow structures of an insect-like flapping wing in Hover. In *27th Congress of International Council of the Aeronautical Sciences*, pp. 1–14.

Poelma, C., Dickson, W. B. & Dickinson, M. H. 2006 Time-resolved reconstruction of the full velocity field around a dynamically-scaled flapping wing. *Experiments in Fluids* **41** (2), 213–225.

Rakotomamonjy, T., Ouladsine, M. & Moing, T. L. 2007 Modelization and kinematics optimization for a flapping-wing microair vehicle. *Journal of Aircraft* **44** (1), 217–231.

Rayner, J. M. V. 1979 A vortex theory of animal flight. Part 1. The vortex wake of a hovering animal. *Journal of Fluid Mechanics* **91** (4), 697–730.

Roache, P. 2003 Error Bars for CFD. In *41st Aerospace Sciences Meeting and Exhibit*. AIAA paper 2003-408.

Roache, P. J. 1998 Verification of codes and calculations. *AIAA Journal* **36** (5), 696–702.

Sane, S. P. 2003 The aerodynamics of insect flight. *Journal of Experimental Biology* **206** (23), 4191–4208.

Sane, S. P. & Dickinson, M. H. 2001 The control of flight force by a flapping wing: lift and drag production. *Journal of Experimental Biology* **204** (15), 2607–2626.

Shahzad, A., Tian, F. B., Young, J. & Lai, J. C. 2017 Numerical study of rigid and flexible wing shapes in hover. *Journal of Physics: Conference Series* **822** (1), 012007.

Shahzad, A., Tian, F. B., Young, J. & Lai, J. C. S. 2016 Effects of wing shape, aspect ratio and deviation angle on aerodynamic performance of flapping wings in hover. *Physics of Fluids* **28** (11), 111901.

Shyy, W., Lian, Y., Tang, J., Liu, H., Trizila, P., Stanford, B., Bernal, L., Cesnik, C. E. S., Friedmann, P. P. & Ifju, P. 2008 Computational aerodynamics of low Reynolds number plunging, pitching and flexible wings for MAV applications. *Acta Mechanica Sinica* **24** (4), 351–373.

Shyy, W. & Liu, H. 2007 Flapping wings and aerodynamic lift: the role of leading-edge vortices. *AIAA Journal* **45** (12), 2817–2819.

Srygley, R. B. & Thomas, A. L. R. 2002 Unconventional lift-generating mechanisms in free-flying butterflies. *Nature* **420** (6916), 660–664.

Taha, H. E., Hajj, M. R. & Nayfeh, A. H. 2013 Wing kinematics optimization for hovering micro air vehicles using calculus of variation. *Journal of Aircraft* **50** (2), 610–614.

Throneberry, G., Hassanalian, M. & Abdelkefi, A. 2017 Optimal design of insect wing shape for hovering nano air vehicles. In *58th AIAA/ASCE/AHS/ASC Structures, Structural Dynamics, and Materials Conference*. AIAA SciTech Forum.

Tudball Smith, D., Rockwell, D., Sheridan, J. & Thompson, M. 2017 Effect of radius of gyration on a wing rotating at low Reynolds number: A computational study. *Physical Review Fluids* **2** (6), 064701.

Usherwood, J. R. & Ellington, C. P. 2002 The aerodynamics of revolving wings II. Propeller force coefficients from mayfly to quail. *Journal of Experimental Biology* **205** (11), 1565–1576.

Vance, J. T. 2009 Experimental and natural variation in hovering flight capacity in bees, Hymenoptera: Apidae. PhD thesis, University of Nevada Las Vegas.

Vogel, S. 1966 Flight in Drosophila I. Flight performance of tethered flies. *Journal of Experimental Biology* **44**, 567–578.

Vogel, S. 1967 Flight in Drosophila: III. Aerodynamic characteristics of fly wings and wing models. *The Journal of Experimental Biology* **46** (3), 431–443.

Wagner, H. 1925 Über die entstehung des dynamischen auftriebes von tragflügeln. *ZAMM-Journal of Applied Mathematics and Mechanics/Zeitschrift für Angewandte Mathematik und Mechanik* **5** (1), 17–35.

Walker, P. B. 1931 Experiments on the growth of circulation about a wing with a description of an apparatus for measuring fluid motion. *Tech. Rep.* 1402. Aeronautical Research Committee. Reports and memoranda.

Wan, H., Dong, H. & Gai, K. 2015 Computational investigation of cicada aerodynamics in forward flight. *Journal of the Royal Society Interface* **12** (102), 20141116.

Wang, Q., Goosen, H. & Keulen, F. V. 2013 Optimal hovering kinematics with respect to various flapping-wing shapes. In *International Micro Air Vehicle Conference and Flight Competition (IMAV2013)*. Toulouse, France.

Weis-Fogh, T. 1973 Quick estimates of flight fitness in hovering animals, including novel mechanisms for lift production. *Journal of Experimental Biology* **59** (1), 169–230.

Wojcik, C. J. & Buchholz, J. H. J. 2014 Vorticity transport in the leading-edge vortex on a rotating blade. *Journal of Fluid Mechanics* **743**, 249–261.

Wolfinger, M. & Rockwell, D. 2014 Flow structure on a rotating wing: effect of radius of gyration. *Journal of Fluid Mechanics* **755**, 83–110.

Wootton, R. J. 1979 Function, homology and terminology in insect wings. *Systematic Entomology* **4** (1), 81–93.

Wootton, R. J. 1992 Functional morphology of insect wings. *Annual Review of Entomology* **37**, 113–140.

Wu, T. Y.-T. 1971 Hydromechanics of swimming propulsion. Part 2. Some optimum shape problems. *Journal of Fluid Mechanics* **46**, 521–544.

Xie, Y. M. & Steven, G. P. 1997 *Basic Evolutionary Structural Optimization*, pp. 12–29. Springer London.

Zanker, J. M. 1990 The wing beat of Drosophila melanogaster. I. Kinematics. *Philosophical Transactions of the Royal Society B: Biological Sciences* **327** (1238), 1–18.

Zanker, J. M. & Götz, K. G. 1990 The wing beat of Drosophila melanogaster. II. Dynamics. *Philosophical Transactions of the Royal Society B: Biological Sciences* **327** (1238), 19–44.

Zhao, L., Huang, Q., Deng, X. & Sane, S. P. 2010 Aerodynamic effects of flexibility in flapping wings. *Journal of the Royal Society Interface* **7** (44), 485–497.

Zheng, L., Hedrick, T. L. & Mittal, R. 2013 A multi-fidelity modelling approach for evaluation and optimization of wing stroke aerodynamics in flapping flight. *Journal of Fluid Mechanics* **721**, 118–154.